LINAC AND DAMPING RING DESIGNS OF THE FUTURE CIRCULAR e^+e^- COLLIDER OF CERN

by

Salim Oğur

B.S., Physics, Boğaziçi University, 2012

M.S., Physics, Boğaziçi University, 2015

Submitted to the Institute for Graduate Studies in
Science and Engineering in partial fulfillment of
the requirements for the degree of
Doctor of Philosophy

Graduate Program in Physics

Boğaziçi University

2019

LINAC AND DAMPING RING DESIGNS OF THE FUTURE CIRCULAR e^+e^- COLLIDER OF CERN

APPROVED BY:

Prof. V. Erkcan Özcan ....
(Thesis Supervisor)

Dr. Frank Zimmermann ....
(Thesis Co-supervisor)

Prof. Erhan Gülmez ....

Prof. Katsunobu Oide ....

Prof. İbrahim Semiz ....

Assoc. Prof. Gökhan N. Ünel ....

DATE OF APPROVAL: 07.05.2019

ACKNOWLEDGEMENTS

It was an honor to be a CERN doctoral student under supervision of Katsunobu Oide and Frank Zimmermann. There were many chances to learn from them, also plenty of opportunities world-wide to learn, apply and present which all become the heartland of this thesis.

The global Future Circular Collider study consists of hundreds of people from all over the world, however the FCC-e^+e^- injector team at CERN deserves a special thanks besides my supervisors in this thesis. Thus, many thanks to Yannis Papaphiloppou, Bernhard Holzer, Özgür Etişken, Bastian Härer and Tessa Charles.

This thesis is not just limited to beam optics and dynamics designs performed at CERN, but it has many inputs from Iryna Chaikovska, Robert Chehab of LAL, Paris, France; Danila Nikiforov, Alexey Levichev, Pavel Martyshkin, Dmitry Shatilov of BINP, Novosibirsk, Russia; also from John T. Seeman of SLAC, Stanford, USA. Last but not least, a very well-deserved and special thanks to KEK, Ibaraki, Japan. I count myself auspicious to work with Kazuro Furukawa, Naoko Iida, Takuya Kamitani, Yuji Seimiya. Their valuable inputs and the works we carried out at KEK are the other milestones of this thesis.

In the end, I would like to thank a lot to my university supervisor and pacemaker V. Erkcan Özcan. It was always a friendly, challenging yet attainable adventure to be guided by him during my graduate studies.

Special thanks to KahveLab, Gökhan Ünel, my friends and family for always being there for me.

ABSTRACT

LINAC AND DAMPING RING DESIGNS OF THE FUTURE CIRCULAR e^+e^- COLLIDER OF CERN

CERN has started the design of a 98 km circular positron-electron collider as a first step of the global Future Circular Collider (FCC) project since 2014. The FCC-e^+e^- is being designed to furnish high luminosities for Z, W, H, and $t\bar{t}$ particles with different energies and currents in the collider and it will restore the charge decrease due to collisions, scatterings etc. via quasi-continuous top-up injection. However, the pre-injector chain will keep its present course yet cycle distinctly through the 4 operational stages in the collider. The injector complex will consist of a 6 GeV S-Band linac, a damping ring at 1.54 GeV and pre-booster ring to reach 20 GeV for injection to the main booster, which is located in the same tunnel as the collider, which will accelerate the beams to the final energies for collisions. As an alternative option to the pre-booster ring, a 20 GeV linac is also considered. The positrons will be created by impinging onto a hybrid target inside the linac at 4.46 GeV and accelerated in the remaining part of the linac up to 1.54 GeV and get matched to be transferred into the damping ring for radiation damping. The designs of the linacs and damping ring will be the foci of this thesis, as well as the optimisation of bunch schedules of the whole injector complex up to the collider. The beam optics designs are partially applied at SuperKEKB linac of KEK by hands-on operations. The beam based misalignment studies and beam jitter source survey have taken place which are also presented in this thesis.

ÖZET

CERN GELECEĞİN DAİRESEL e^+e^- CARPIŞTIRICISI DOĞRUSAL HIZLANDIRICI VE SÖNÜMLENDİRİCİ HALKA TASARIMI

Avrupa Nükleer Araştırmalar Merkezi (CERN) 2014 yılı itibariyle 98 kilometrelik Geleceğin Dairesel Çarpıştırıcısı (FCC)'nın tasarımına başladı. Projenin ilk adımı olan positron-elektron çarpıştırıcısı FCC-e^+e^-, içerisinde 4 farklı akım ve enerjide; Z, W, H bozonlarını ve $t\bar{t}$ parçacıklarını son derece yüksek ışınlılıklar elde ederek incelemeyi hedefliyor. FCC-e^+e^-, çarpışma, saçılma vb. sebeplerden eksilen yüklerin sürekli gibi geri beslenmesi sayesinde; hedeflenen ışınlılıkta nerdeyse sabit akışta veri toplayabilecek. 4 farklı operasyon için 4 farklı iyileştirmeden geçecek olan çarpıştırıcının aksine, enjektör kompleksi hep aynı donanım ama farklı değişkenleriyle işletilecek. Enjektörler, S-bandında 6 GeV'lik doğrusal hızlandırıcı, 1.54 GeV'de bir sönümlendirici halka, 20 GeV'e kadar enerjiyi artıran ön-artırıcı ve onun beslediği 98 kilometrelik ana-artırıcı dairesel hızlandırıcılardan oluşacaktır. Ana-artırıcı, çarpıştırıcı ile aynı tünelin içine yerleştirilecek ve demeti hedeflenen çarpışma enerjilerine hızlandıracak. Ön-artırıcı yerine, doğrusal hızlandırıcıyla 20 GeV'e ulaşıp doğrudan ana-artırıcıyı besleme seçeneği de düşünülmüştür. Pozitron kümeleri, doğrusal hızlandırıcının 4.46 GeV'e karşılık gelen noktasında elektronların ikili-hedefe çarptırılması sonucu oluşturulacaklardır. Hedeften salınan pozitronlar yakalanıp hızlandırıcının geri kalan 1.54 GeV'lik kısmında hızlandırılıp, ardından yayınımlarının ışınım yaparak küçülmesi için sönümlendirici halkaya aktarılacaklar. Doğrusal hızlandırıcı ve sönümlendirici halka tasarımları ile birlikte enjektörlerin zaman çizelgeleri ve yeterlilikleri bu tezin ana konusudur. Demet optik tasarımları kısmi olarak KEK'in SuperKEKB çarpıştırıcısını besleyen doğrusal hızlandırıcısında uygulanmıştır. KEK'te demet kullanarak mıknatıs sapmaları ve demet titreşme sebeplerinin belirlenmesi üzerine yapılmış çalışmalar da bu tezde sunulmuştur.

TABLE OF CONTENTS

LIST OF FIGURES

LIST OF TABLES

LIST OF SYMBOLS

$\vec{A}$	Electromagnetic vector potential
$\vec{a}$	Scaled vector potential
$\vec{B}$	Magnetic field
C	Circumference of the ring
c	Speed of light
E	Energy
$\vec{E}$	Electric field
e	Electron charge
e^-	Electron
e^+	Positron
f	Revolution frequency
h	Harmonic number
H	Higgs boson
H	Hamiltonian
hh	Hadron-hadron
K	New Hamiltonian after canonical transformation
k	Wave number
$\mathscr{L}$	Lagrangian
m_0	Rest mass
N	Number of particles
P	Power
P_i	Transformed coordinates in momentum space
p_i	Coordinates in momentum space
P_0	Momentum of the reference particle
q	Charge of a particle
Q	Betatron tune
Q_i	Spatial transformed coordinates
q_i	Spatial coordinates

R	Transfer Matrix
r_e	Radius of electron
T	Period
T	Intra-beam scattering growth time
t	Top quark
$\bar{t}$	Top antiquark
U_0	Energy loss per turn
V_{rf}	Voltage in an RF cavity
W	W boson
W_T	Transverse wakefield per unit length
W_L	Longitudinal wakefield per unit length
Z	Z boson
α	Twiss parameter alpha
α_p	Momentum compaction factor
β	Twiss parameter beta
β_{rel}	Relativistic beta
γ	Twiss parameter gamma
γ_{rel}	Relativistic gamma
δ	Momentum spread
ϵ_{rms}	Root-mean-square (i.e. geometric) emittance
ϵ_{norm}	Normalized emittance
ε_0	Vacuum permittivity
η	Dispersion function
η_p	Slippage factor
λ	RF wavelength
μ	Betatron phase advance over one complete turn
ν	Speed of the particle
ξ	Chromaticity
ω	Angular cavity frequency
ρ	Bending radius

σ	Root-mean-square size
φ	Phase advance
ϕ	Cavity phase advance
ϕ	Scalar potential

LIST OF ACRONYMS/ABBREVIATIONS

BCtoLinac	Bunch Compressor to the Linac Beam Transfer Line
BINP	Budker Institute of Nuclear Physics
BNS	Balakin-Novokhatsy-Smirnov
BR	Booster Ring
BS	Beamstrahlung
BTL	Beam Transfer Line
CERN	European Organization for Nuclear Research
CLIC	Compact Linear Collider
CM	Center of Mass
CSR	Coherent Synchrotron Radiation
DR	Damping Ring
ECS	Energy Compressor System
EM	Electromagnetic
FCC	The Future Circular Collider
FODO	Focusing and defocusing quadrupole lenses in alternating order
IBS	Intra-Beam Scattering
KBE	KEKB electron injection
KBP	KEKB positron injection
KEK	High Energy Accelerator Research Organization
LEP	Large Electron Positron Collider
LHC	Large Hadron Collider
Linac	Linear Accelerator
LitoDR	Linac to the Damping Ring Beam Transfer Line
NC	Normal Conducting
PRB	Pre-booster Ring
PS	Proton Synchrotron
QFE	Injection to photon factories at KEK
QUT	Quadrupole under test

RF	Radio-Frequency
SC	Super Conducting
SLAC	Stanford Linear Accelerator
SLC	Stanford Linear Collider
SPS	Super Proton Synchrotron
SFE	RF-gun low emittance electrons for KEKB
SR	Synchrotron Radiation
SuperKEKB	Upgraded B-meson factory at KEK
3D	Three Dimensional
6D	Six Dimensional

1. INTRODUCTION

The world's leading particle and accelerator physics laboratory CERN has started to design an accelerator complex to succeed the existing 26.7 km Large Hadron Collider (LHC). On one hand, Compact Linear Collider (CLIC), as a post-LHC linear collider option, offers a linear extendable lepton collider potent to reach TeV energy, nonetheless it does not enable an option for the study of hadrons. On the other hand, the FCC in a 98 km tunnel will host different colliders to study a variety of options, subsequently. First, the circular lepton collider up to 365 GeV center of mass (CM) energy will be dedicated for the precision study of the already discovered particles, then a hadron collider of 100 TeV CM energy which will replace the lepton collider and seek beyond the knowns. Finally, a lepton-hadron collider will take place by an additional electron recovery linac to intercept the hadron beam [1]. Therefore, the FCC will have the world energy frontier, the FCC-*hh*, and a luminosity frontier, the FCC-e^+e^- , as the potential first step of the project. The injector complex of the lepton collider is the focus of this thesis.

The design of an injector chain requires an overall injection strategy including store times in each accelerator, most importantly sufficiency of the complex to reach the extremely high target luminosities. Since the FCC-e^+e^- will have a 98-km top-up booster in the same tunnel as the collider, the beam loss due to collisions will be quasi-continuously restored. Therefore, the optimization of the injector chain becomes vital not just because of the cost minimisation and being limited to the available technology, but also due to the short beam lifetime in the collider and additional fluctuations that can occur while injecting the lost charge back into the bucket.

Beam optics, as the name evokes, is similar to light optics requiring focusing and directing instruments to transport the beam to the designated spot. Unlike the photon beam (i.e. light), the lepton beam has a certain charge which creates a repulsive force, also the aim is to preserve this beam and to increase its energy even more. Therefore, magnets are required to keep the charged beams in the track, meanwhile cavities are needed for the acceleration. All together, we have a machine made of metals, and the beam interacts with the metallic structures as well as it interacts within itself. Therefore, the path followed in this thesis is to start with introducing the project and injectors, then to discuss the dynamics of a charged particle in transverse and longitudinal planes, which should be followed by the imperfections created by the interactions and the misalignment of the accelerator elements. Finally, some implementation of accelerator physics acquired will be applied on an existing machine, namely SuperKEKB injector linac.

1.1. Overview of the FCC-e^+e^-

The FCC-e^+e^- is being designed to serve as a precision factory for Z, W, H bosons and $t\bar{t}$ quarks, covering beam energies from 45.6 to 182.5 GeV. The beam current stored in the collider decreases as the final energy in the collider increases in order to limit the total radiated synchrotron power to 100 MW throughout the four operational modes [2]. The collider operational parameters can be found in Table 1.1 [3, 4].

The injector complex consists of a linac and damping ring [5], pre-booster synchrotron [6], and top-up booster [7] as visualised in Figure 1.1. The collider will have two beam pipes, one for each species, yet the rest of the pre-injector synchrotrons having one beam pipe can accumulate and accelerate solely one kind at a session. Therefore, depending upon the necessary beam to be injected into the collider, injectors will follow either of the way stated below.

(i) Electron Beam Delivery

Step 1: 3.4 nC electron beam injected into the linac at 10 MeV from radio frequency (RF) gun,

Step 2: Acceleration of the e^- beam in the Linac up to 1.54 GeV,

Step 3: Injection at that energy into the damping ring (DR) for emittance cooling,

Step 4: Injecting the beam back to the linac at 1.54 GeV via bunch compressor (not shown in Figure 1.1),

Step 5: Acceleration in the linac up to 6 GeV,

Table 1.1. FCC-e^+e^- Machine Parameters [3, 4]

operation mode	Z	W	$H(ZH)$	$t\bar{t}$
beam energy [GeV]	45.6	80	120	182.5
arc cell optics	60/60	90/90	90/90	90/90
momentum compaction [10^{-5}]	1.48	0.73	0.73	0.73
horizontal emittance [nm]	0.27	0.28	0.63	1.45
vertical emittance [pm]	1.0	1.0	1.3	2.9
horizontal beta* [m]	0.15	0.2	0.3	1
vertical beta* [mm]	0.8	1	1	2
length of interaction area [mm]	0.42	0.5	0.9	1.75
longitudinal damping time [ms]	414	77	23	6.6
SR energy loss / turn [GeV]	0.036	0.34	1.72	9.21
total RF voltage [GV]	0.10	0.44	2.0	10.9
RF acceptance [%]	1.9	1.9	2.3	3.7
energy acceptance [%]	1.3	1.3	1.5	2.8
energy spread (SR / BS) [%]	0.038 / 0.132	0.066 / 0.153	0.099 / 0.15	0.153 / 0.192
bunch length (SR / BS) [mm]	3.5 / 12.1	3.3 / 7.65	3.15 / 4.9	1.93 / 2.43
Piwinski angle (SR / BS)	8.2 / 28.5	6.6 / 15.3	3.4 / 5.3	0.76 / 0.96
bunch intensity [10^{11}]	1.7	1.5	1.5	2.2
no. of bunches / beam	16640	2000	393	50
beam current [mA]	1390	147	29	5.4
luminosity [10^{34} cm^{-2}s^{-1}]	230	32	7.8	1.4
beam-beam parameter (x / y)	0.004 / 0.133	0.0065 / 0.118	0.016 / 0.108	0.099 / 0.138
luminosity lifetime [min]	70	50	42	39
time between injections [sec]	122	44	31	32
allowable asymmetry [%]	$\pm$ 5	$\pm$3	$\pm$ 3	$\pm$ 3
actual lifetime by BS ("weak") [min]	$>$ 200	20	18	24

Step 6: Pre-booster ring (PRB) or C-Band linac for 6-20 GeV acceleration,

Step 7: 98-km top-up booster for acceleration from 20 GeV to the final energies.

(ii) Positron Beam Delivery

Step 1: 10 nC electron beam injected into the linac from the thermionic gun,

Step 2: Acceleration of the e^- beam in the linac up to 4.46 GeV,

Step 3: Impinging on the target with that e^- beam to create e^+ ,

Step 4: Pre-injector linac for positron about 0.2 GeV,

Step 5: Acceleration of e^+ in the linac up to 1.54 GeV,

Step 6: Injection at that energy into the damping ring for emittance cooling, Step 7: Injecting the beam back to the linac at 1.54 GeV via bunch compressor (not shown in Figure 1.1),

Step 8: Acceleration in the linac up to 6 GeV,

Step 9: Pre-booster synchrotron or C-Band linac for 6-20 GeV acceleration,

Step 10: 98-km top-up booster ring (BR) for acceleration from 20 GeV to the final energies.

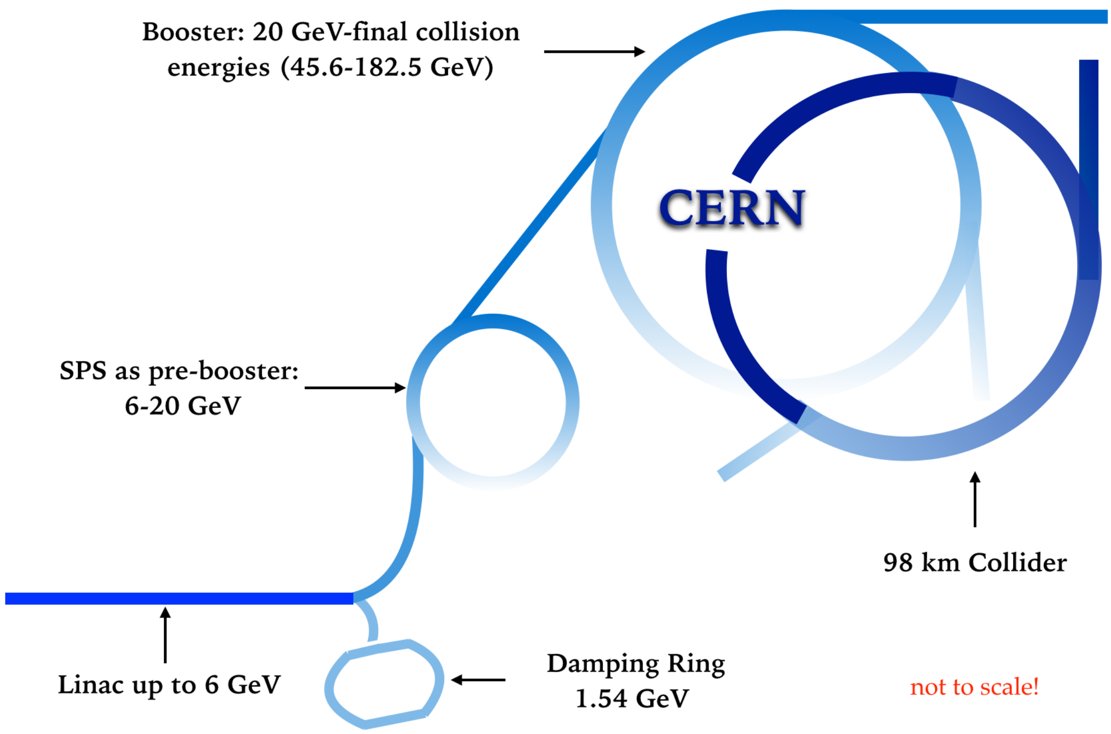

Figure 1.1. FCC-e^+e^- main layout (transfer line from DR back to linac is omitted).

The FCC-e^+e^- injector baseline foresees a pre-booster synchrotron for the acceleration from 6 to 20 GeV that would most likely to be the SPS with some slight modifications as it was utilised during the Large Electron-Positron Collider (LEP) operation. As an alternative to the pre-booster, a longer linac accelerating up to 20 GeV is being designed. In either case, 20 GeV beams will be injected into the 98 km top-up booster to reach the final collision energies. The bunch population at the collider will be reached by accumulating for around 10 injections the current in every collider bunch, at each injection. For this reason, 2.13×10^{10} particles per bunch have been considered for the pre-injectors taking into account some transmission efficiency above 80%.

The 1.54 GeV damping ring (DR) will be at the end of the linac and electrons will be transferred from a branching point in the linac at 1.54 GeV (its drawing is omitted in the layout scheme). It is possible to tilt the DR just by a small angle in order not to bend e^+ beam noticeably. In this way, the beam transfer lines can share the same tunnel as the main linac.

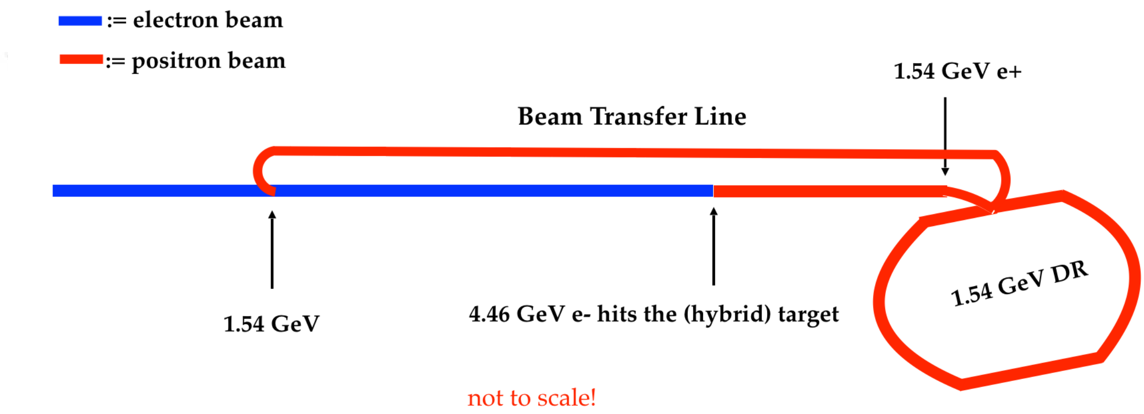

Figure 1.2. Positron flow scheme using the same linac as for the electrons. Notice that the positrons will be transferred back to the linac, drawn green.

2. THEORY OF PARTICLE DYNAMICS

Particles in an accelerator move in a vacuumed volume controlled by the electromagnetic(EM) fields. Magnets are required in order to keep a *bunch* of particles in a designated reference orbit in a congested volume meanwhile they are also accelerated in the RF cavities. Magnets are indeed of great importance due to the fact that the charged particles in a bunch result in a repulsive Coulomb interaction, so called *space charge*. Apart from this, the interaction between the bunch and the surrounding metallic boundaries leads to *wakefields* which result in emittance blow and possible transmission loss. Therefore, in order to describe the dynamics of charged particles in an accelerator, it is better to commence with the particles assuming no internal or external interaction, and first construct their dynamics, then gradually include the beam quality diluting effects: wakefields and *collective effects* such as space charge and scattering.

The vector-matrix notation is a powerful formalism simplifying the complexity of the particle dynamics and beam optics. For this reason, we will construct those matrices providing linear transfer maps by reckoning with the kinematics of a charged particle in an EM-field [13]. The Lagrangian of a particle with charge q travelling in EM-field with speed ν and rest mass m_0 is:

$$\mathscr{L} = -m_0 c^2 \sqrt{1 - \frac{\nu^2}{c^2}} - q\phi + q\vec{\nu} \cdot \vec{A}, \tag{2.1}$$

where the electromagnetic vector and scalar potentials are $\vec{A}$ and ϕ, respectively. The electric and magnetic fields can be derived from the potentials, seriatim:

$$\vec{E} = -\vec{\nabla}\phi - \frac{\partial \vec{A}}{\partial t}, \tag{2.2}$$

$$\vec{B} = \vec{\nabla} \times \vec{A}. \tag{2.3}$$

Furthermore, the Lagrangian in Equation 2.1 can be substituted in the Euler-Lagrange equation as below in order to figure out the force acting on the particle:

$$\frac{d}{dt}\left(\frac{\partial \mathscr{L}}{\partial \dot{q}_i}\right) - \frac{\partial \mathscr{L}}{\partial q_i} = 0, \tag{2.4}$$

where q_i refers to the space coordinates and $\dot{q}_i$ is its time derivative, thereby p_i becomes the canonical momenta with $m = \gamma_{rel} m_o$ where γ_{rel} is the relativistic Lorentz factor:

$$p_i = \frac{\partial \mathscr{L}}{\partial \dot{q}_i} = m\nu_i + qA_i. \tag{2.5}$$

Thus, the Euler-Lagrange equation will result in the Lorentz force as expected:

$$\vec{F} = q\vec{E} + q\vec{\nu} \times \vec{B}. \tag{2.6}$$

The Hamiltonian can be found using the identity:

$$H = \sum_i \dot{q}_i p_i - \mathscr{L}(q, \dot{q}, t). \tag{2.7}$$

By substituting the Equations 2.1 and 2.5 into Equation 2.7, the Hamiltonian will yield:

$$\begin{aligned} H &= \nu_x p_x + \nu_y p_y + \nu_x p_x + \frac{m_o c^2}{\gamma_{rel}} - q\vec{\nu} \cdot \vec{A} + q\phi \\ &= m\nu^2 + \frac{m_o c^2}{\gamma_{rel}} + q\phi \\ &= \gamma_{rel} m_o c^2 + q\phi \end{aligned}$$

As a result, the Hamiltonian of a relativistic particle in EM-field in Cartesian coordinates is found to be:

$$H = c\sqrt{(\vec{p} - q\vec{A})^2 + m^2c^2} + q\phi. \tag{2.8}$$

In addition, the generating functions are needed to construct canonical transformations of Equation 2.8. There are four standard mixed-variable generating functions transforming (q_i, p_i) to their new counterparts (Q_i, P_i) with K being the new Hamiltonian:

(i) *first kind:* $F_1 = F_1(q, Q, t)$, $p_i = \frac{\partial F_1}{\partial q_i}$, $P_i = -\frac{\partial F_1}{\partial Q_i}$, $K = H + \frac{\partial F_1}{\partial t}$.

(ii) *the second kind:* $F_2 = F_2(q, P, t)$, $p_i = \frac{\partial F_2}{\partial q_i}$, $Q_i = \frac{\partial F_2}{\partial P_i}$, $K = H + \frac{\partial F_2}{\partial t}$.

(iii) *the third kind:* $F_3 = F_3(p, Q, t)$, $q_i = -\frac{\partial F_3}{\partial p_i}$, $P_i = -\frac{\partial F_3}{\partial Q_i}$, $K = H + \frac{\partial F_3}{\partial t}$.

(iv) *the fourth kind:* $F_4 = F_4(p, P, t)$, $q_i = -\frac{\partial F_4}{\partial p_i}$, $Q_i = \frac{\partial F_4}{\partial P_i}$, $K = H + \frac{\partial F_4}{\partial t}$.

In order to illustrate the canonical transformations, we can construct the Hamiltonian of a relativistic particle for a curved space [14]. The motion of particles are guided by the magnets throughout the accelerator, and the simplest magnet is a dipole bend which results in a curved orbit. The Cartesian coordinates (X, Y, Z) in Figure 2.1

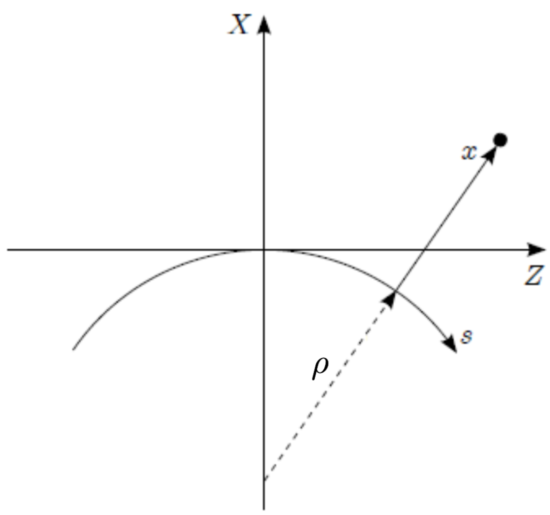

Figure 2.1. Curved trajectory of a relativistic particle due to a dipole bend [14].

are defined for a particle together with the canonical momenta (P_X, P_Y, P_Z). ρ is the bending radius, s is the arc length and x and y are the local (i.e. moving) coordinates which are always perpendicular to s. Therefore, the Cartesian coordinates become:

$$\begin{aligned} X &= (x+\rho)\cos\left(\frac{s}{\rho}\right) - \rho, \\ Y &= y, \\ Z &= (x+\rho)\sin\left(\frac{s}{\rho}\right). \end{aligned} \tag{2.9}$$

We need to perform a transformation from Cartesian to the curved spatial coordinates. For this reason, Equation 2.9 and corresponding momenta are substituted in the third generating function which follows:

$$F_3 = -\left((x+\rho)\cos\left(\frac{s}{\rho}\right) - \rho\right) P_X - yP_Y - (x+\rho)\sin\left(\frac{s}{\rho}\right) P_Z, \tag{2.10}$$

where F_3 has no explicit time dependence leading to equality of new and old Hamiltonians $K = H$. In addition, we can solve for the canonical momenta using $p_i = -\frac{\partial F_3}{\partial q_i}$:

$$\begin{aligned} p_x &= P_X \cos\left(\frac{s}{\rho}\right) + P_Z \sin\left(\frac{s}{\rho}\right), \\ p_y &= P_Y, \\ p_s &= P_Z\left(1+\frac{x}{\rho}\right)\cos\left(\frac{s}{\rho}\right) - P_X\left(1+\frac{x}{\rho}\right)\sin\left(\frac{s}{\rho}\right). \end{aligned} \tag{2.11}$$

On the other hand, we need to express the corresponding new vector potential A_{q_i} by vector decomposition of the old vector potential A_{Q_i}:

$$\begin{aligned} A_x &= A_X \cos\left(\frac{s}{\rho}\right) - A_Z \sin\left(\frac{s}{\rho}\right), \\ A_y &= A_Y, \\ A_s &= A_Z \cos\left(\frac{s}{\rho}\right) + A_X \sin\left(\frac{s}{\rho}\right). \end{aligned} \tag{2.12}$$

Thus, by substituting Equation2.11 and 2.12 into the Equation 2.8, we find the new Hamiltonian:

$$K = H = c\sqrt{\left(\frac{p_s}{1+\frac{x}{\rho}} - qA_s\right)^2 + (p_x - qA_x)^2 + (p_y - qA_y)^2 + m^2c^2} + q\phi. \tag{2.13}$$

2.1. Linear Transfer Maps

The dynamics of the particles in an accelerator is defined as a 6-dimensional (6D) vector which spans both spatial (q_i) and phase (p_i) spaces, whereby the Hamiltonian mechanics leading to conserved quantities can be exploited. In Figure 2.2, a bunch of particles are illustrated in a moving coordinate system, where the spatial and canonical coordinates are defined with respect to a reference particle, so called the *synchronous particle* [15]. The coordinate system conventionally used in accelerator physics is the right hand rule orthogonal system in which x is horizontal to the earth ground, y is vertical and the particles are accelerated in the direction of z or interchangeably s for the case of the curved orbit. The designation of a synchronous (reference) particle is

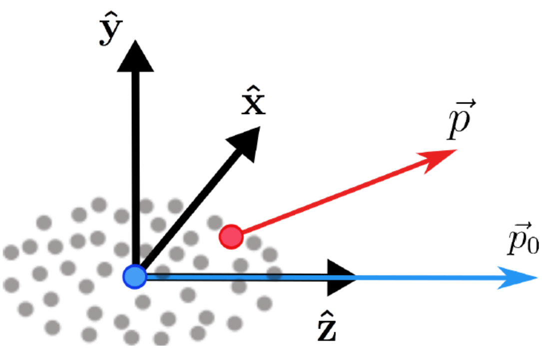

Figure 2.2. Bunch of particles in a moving coordinate system [15].

quite useful which is assumed to be located at the weighted average of all the particles' spatial coordinates with the reference momentum in the direction of acceleration, in other words, the synchronous particle stands for the *centroid* of the bunch. For instance, the small angle along the x-axis can be defined as:

$$x' = \frac{dx}{dz}, \tag{2.14}$$

This angle can be also used to describe the associated momentum in that axis with respect to the reference momentum p_0 as follows:

$$p_x = p_0 x' = \gamma_{rel}\beta_{rel} m_0 c x', \tag{2.15}$$

Similarly. the vertical plane for y can be defined by (y, p_y). Finally, the longitudinal direction will be defined as (z, δ), where the momentum dispersion or the energy spread with respect to reference momentum is $\delta = \frac{\Delta p}{p_o}$. Therefore, the 6D vector which defines a particle's space and momenta is:

$$\overrightarrow{x_0} = \begin{pmatrix} x \\ p_x \\ y \\ p_y \\ z \\ \delta \end{pmatrix}. \tag{2.16}$$

If the linear transfer map of each accelerator element is achieved, the particle defined by Equation 2.16 can be propagated [14]. In order to achieve such transfer matrices, we need to rearrange the Hamiltonian in Equation 2.13 by defining the scaled vector potential as $\vec{a} = \frac{q}{P_0}\vec{A}$ and the curvature as $h = \frac{1}{\rho}$:

$$\begin{aligned} H = \frac{\delta}{\beta_{rel}} - (1 + hx)\sqrt{\left(\delta + \frac{1}{\beta_{rel}} - \frac{q\phi}{cp_0}\right)^2 - (p_x - a_x)^2 - (p_y - a_y)^2 - \frac{1}{\beta_{rel}^2\gamma_{rel}^2}} \\ - (1 + hx)a_s. \end{aligned} \tag{2.17}$$

where $z = \frac{s}{\beta_{rel}} - ct$ and $\delta = \frac{E}{cp_0} - \frac{1}{\beta_{rel}}$ with the energy $E = \gamma_{rel} m_0 c^2$.

The equation of motion for a charged particle in a region can be achieved by substituting the potentials present in that region into Equation 2.17. For instance, the *drift space* is the straight region (i.e. curvature $h = 0$) where the potentials ϕ and $\vec{a}$ are both zero, therefore the Hamiltonian for the drift space is:

$$H = \frac{\delta}{\beta_{rel}} - \sqrt{\left(\delta + \frac{1}{\beta_{rel}}\right)^2 - p_x^2 - p_y^2 - \frac{1}{\beta_{rel}^2 \gamma_{rel}^2}}. \tag{2.18}$$

The equations of motion corresponding to this Hamiltonian can be calculated. The horizontal equations are as follows:

$$-\frac{\partial H}{\partial x} = 0, \qquad \frac{\partial H}{\partial p_x} = \frac{p_x}{d}, \tag{2.19}$$

where the parameter d is defined as:

$$d = \sqrt{\left(\delta + \frac{1}{\beta_{rel}}\right)^2 - p_x^2 - p_y^2 - \frac{1}{\beta_{rel}^2 \gamma_{rel}^2}}. \tag{2.20}$$

Similarly, we can find the vertical equations of motion as follows:

$$-\frac{\partial H}{\partial y} = 0, \qquad \frac{\partial H}{\partial p_y} = \frac{p_y}{d}. \tag{2.21}$$

Finally, the longitudinal equations of motion are:

$$-\frac{\partial H}{\partial y} = 0, \qquad \frac{\partial H}{\partial \delta} = \frac{1}{\beta_{rel}}\left(1 - \frac{1}{d}\right) - \frac{\delta}{d}. \tag{2.22}$$

Thus, the 6D vector elements will transformed from the initial $\overrightarrow{x_0} = (x_0, p_{x_0}, y_0, p_{y_0}, z_0, \delta_0)$ at $s = s_0$ to the final $\overrightarrow{x_1} = (x_1, p_{x_1}, y_1, p_{y_1}, z_1, \delta_1)$ at $s = s_1 = s_0 + L$ where L is the drift length:

$$
\begin{aligned}
x_1 &= x_o + \frac{p_{x0}}{d} L, \\
p_{x_1} &= p_{x_0}, \\
y_1 &= y_o + \frac{p_{y0}}{d} L, \\
p_{y_1} &= p_{y_0}, \\
z_1 &= z_0 + \frac{L}{\beta_{rel}} \left(1 - \frac{1}{d}\right) - \frac{\delta_0}{d} L, \\
\delta_1 &= \delta_0.
\end{aligned}
\tag{2.23}
$$

It turns out that p_x, p_y and d are constants from Equation 2.19-2.22 as well as δ. In Equation 2.23, d appears as a non-linear function of the powers of the canonical momenta. Wherefore, power series expansion of d in Equation 2.23 can be a useful approximation to obtain the linear transformation:

$$
\begin{aligned}
x_1 &= x_o + p_{x_0} L + \mathcal{O}(2), \\
p_{x_1} &= p_{x_0}, \\
y_1 &= y_o + p_{y_0} L + \mathcal{O}(2), \\
p_{y_1} &= p_{y_0}, \\
z_1 &= z_0 + \frac{L}{\beta_{rel}^2 \gamma_{rel}^2} + \mathcal{O}(2), \\
\delta_1 &= \delta_0.
\end{aligned}
\tag{2.24}
$$

Hence, we have achieved the drift space transfer matrix for a length L by neglecting the higher order terms i.e. $\mathcal{O}(2)$:

$$
R_{drift} = \begin{pmatrix}
1 & L & 0 & 0 & 0 & 0 \\
0 & 1 & 0 & 0 & 0 & 0 \\
0 & 0 & 1 & L & 0 & 0 \\
0 & 0 & 0 & 1 & 0 & 0 \\
0 & 0 & 0 & 0 & 1 & \frac{L}{\beta_{rel}^2 \gamma_{rel}^2} \\
0 & 0 & 0 & 0 & 0 & 1
\end{pmatrix}.
\tag{2.25}
$$

As a result, the linear transformation of the 6D vector of the particle turns out to be:

$$\overrightarrow{x_1} = R_{drift}\overrightarrow{x_o}. \tag{2.26}$$

In addition, transfer maps for each accelerator element can be constructed. For example, the transfer matrix for the focusing[1] quadrupole magnet is [14]:

$$R_{quad} = \begin{pmatrix} \cos(\omega L) & \frac{\sin(\omega L)}{\omega} & 0 & 0 & 0 & 0 \\ -\omega\sin(\omega L) & \cos(\omega L) & 0 & 0 & 0 & 0 \\ 0 & 0 & \cosh(\omega L) & \frac{\sinh(\omega L)}{\omega} & 0 & 0 \\ 0 & 0 & \omega\sinh(\omega L) & \cosh(\omega L) & 0 & 0 \\ 0 & 0 & 0 & 0 & 1 & \frac{L}{\beta_0^2\gamma_0^2} \\ 0 & 0 & 0 & 0 & 0 & 1 \end{pmatrix}, \tag{2.27}$$

where ω corresponds to square-root of the quadrupole integrated strength K_1 as follows:

$$\omega = \sqrt{K_1}. \tag{2.28}$$

The first two rows of Equation 2.27 state that the quadrupole is focusing in horizontal direction (x) if $K_1 > 0$, whereas the third and fourth rows show that it is defocusing vertically (i.e. y), and the last two rows point out that the longitudinal plane is transformed as in the drift space case. Therefore, $K_1 < 0$ refers to focusing quadrupole in vertical axis. Besides, the notation of ω has been intentionally chosen to make a link to the oscillations controlled by the quadrupoles which will be discussed in Section 2.3. Lastly, the matrix elements act on one plane merely, meaning there is no co-variance term between x and y or/and z, therefore it can be concluded that the quadrupoles do not create coupling, or the motion guided by quadrupoles are ideally de-coupled.

The R matrices for each accelerator element are embedded in the beam optics and dynamics design programs, such as in the code *SAD* [16] which is used throughout this thesis. For instance, a beamline consisting of a focusing quadrupole, a drift space,

[1]The focusing quadrupole conventionally refers to focusing in x-axis in the literature.

defocusing quadrupole, and another drift space will have the transfer matrix:

$$R = R_{drift_2} R_{defocus} R_{drift_1} R_{focus}, \tag{2.29}$$

where the overall transfer matrix R is the matrix multiplication of the transfer matrices of the beamline elements in backward direction. In fact, it is multiplying the initial 6D vector $\overrightarrow{x_0}$ step by step with beam line elements in respective order. Last but not least, this special beamline is called a *FODO* lattice, which is frequently used in this thesis both in linac and damping ring designs.

2.2. Magnets

There is no magnetic monopole, therefore poles come in pair in the magnets with the Latin naming convention, except the solenoid which is mostly not considered as multipole. The particles in an accelerator are guided longitudinally and steered by the dipoles, and kept together transversely by the quadrupoles, sextupoles, octupoles, and higher order multipoles. Among those, there are also combined function magnets achieved by breaking the symmetry between the pole axes or by adding additional windings to the magnet coils. Normally, the multipoles, excluding the fringe fields, can be fairly defined in the transverse plane, which are also known as *hard edge magnets*.

The magnetic field of a pure multipole magnet can be derived from the Maxwell equations for a region without charge or current (i.e. inside the beam pipe without the beam passing through). The magnetic field in that case:

$$\overrightarrow{\nabla} \cdot \overrightarrow{B} = 0, \tag{2.30}$$

$$\overrightarrow{\nabla} \times \overrightarrow{B} = 0. \tag{2.31}$$

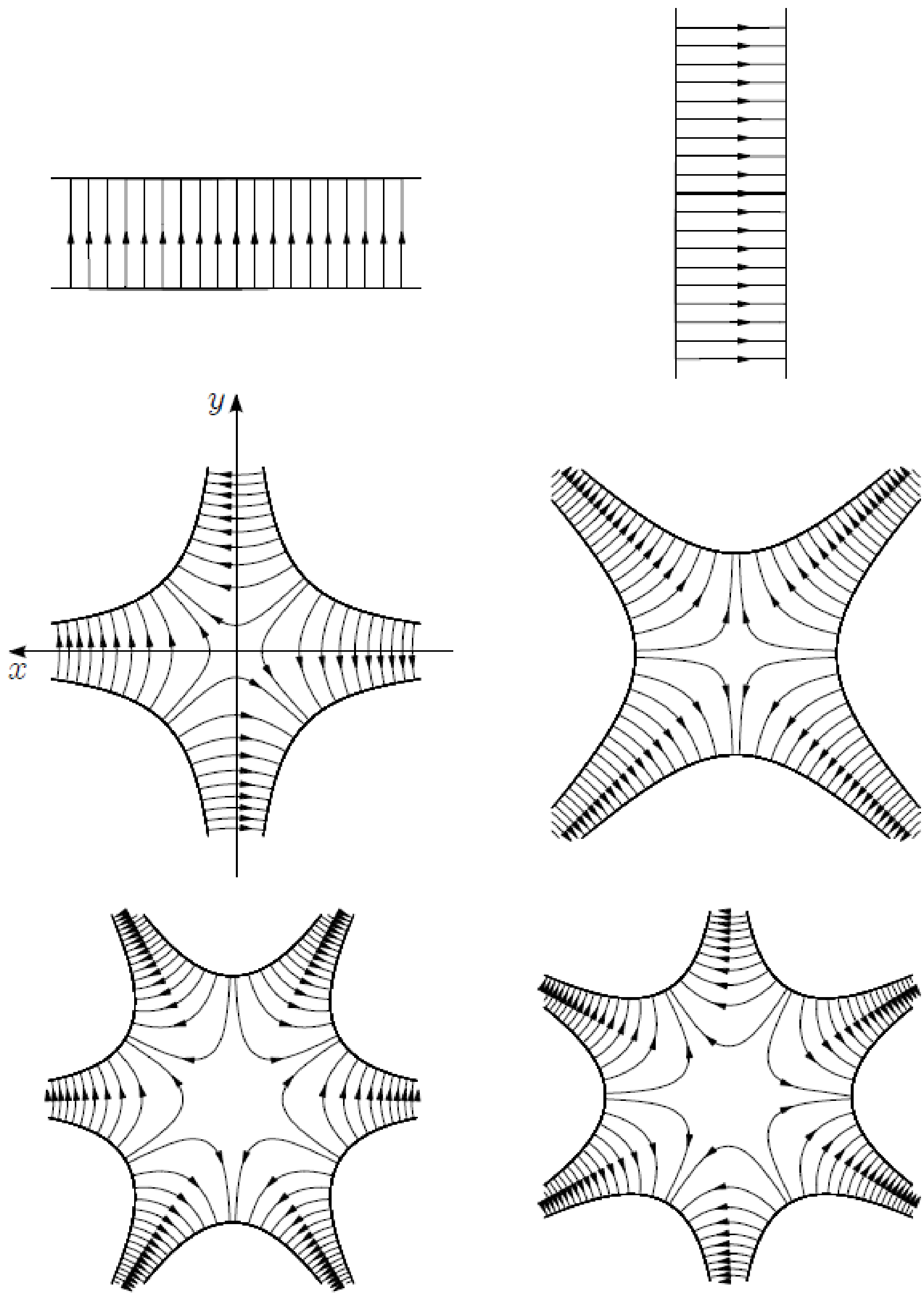

Figure 2.3. Multipole field lines. Top row: dipole. Middle row: quadrupole. Bottom row: Sextupole. Left column stands for the normal multipoles ($a_n = 0$), while right column presents the skew ($b_n = 0$) counterparts [14].

Here, the magnetic field obeying Eqs. 2.30 and 2.31 is:

$$B(z) = B_y + iB_x = B_{ref} \sum_{n=0}^{\infty} [b_n + ia_n] \left(\frac{x + iy}{R_{ref}} \right)^n , \tag{2.32}$$

where $B_z = 0$ for the multipoles if it is not stated otherwise, B_x and B_y are real; B_{ref} and R_{ref} are arbitrarily chosen reference magnetic field and radius respectively. In addition, the parameter n corresponds to dipoles when $n = 0$, quadrupoles for $n = 1$, sextupoles for $n = 2$, and so on in US notation which is chosen since the accelerator design code *SAD* follows that convention. Besides, the angle of the skewness ϕ can be added in order to show the orientation of the field, which is provided by multiplying Equation 2.32 with $e^{i\phi_n}$. Generally, $\phi_n = 0$ or $\phi_n = \pi$ refers to the *normal multipole*, whereas the *skew multipoles* are with $\phi_n = \pm\frac{\pi}{2}$. Figure 2.3 shows the magnetic field lines in example multipoles.

The impact of the magnets to the particle dynamics requires the substitution of the potentials (i.e. $\vec{A}$, and V) into the Hamiltonian as discussed in Section 2.1. Therefore using the identity $\vec{B} = \vec{\nabla} \times \vec{A}$, the vector potential yielding Equation 2.32 can be found as:

$$A_z = -B_{ref} \ \mathbb{R}\mathrm{e} \left\{ \sum_{n=0}^{\infty} [b_n + ia_n] \frac{r^{n+1} e^{i\theta(n+1)}}{(n+1) R_{ref}^n} \right\} . \tag{2.33}$$

In Equation 2.33 the choice of gauge is such that the horizontal and vertical components of the vector potential are zero. Furthermore, in order to find a_n and b_n coefficients, we can look into the derivatives of the field components with respect to the transverse axes, as follows:

$$\frac{\partial^n B_y}{\partial x^n} = \frac{\partial^n B_x}{\partial y^n} = n! \frac{B_{ref}}{R_{ref}^n} b_n, \tag{2.34}$$

for a normal multipole by recalling $a_n = 0$; whereas for the skew multipole (i.e. $b_n = 0$):

$$\frac{\partial^n B_x}{\partial x^n} = \frac{\partial^n B_y}{\partial y^n} = n! \frac{B_{ref}}{R_{ref}^n} a_n. \tag{2.35}$$

Therefore, Equation 2.34 states that a normal dipole magnet (i.e. bending in x-axis) has uniform field in y-axis, while a quadrupole has a linearly increasing field with x for $y = 0$ or vice versa. Last but not least, the sextupole field increases with x^2 at $y = 0$, similarly increases with y^2 for $x = 0$. All in all, we can define the *normalised multipole strength* for a particle with charge q and reference momentum p_0:

$$k_n = \frac{q}{p_0}\frac{\partial^n B_y}{\partial x^n}, \tag{2.36}$$

for normal multipoles whereas for the skew multipoles, it is:

$$k_n^{skew} = -\frac{q}{p_0}\frac{\partial^n B_x}{\partial x^n}. \tag{2.37}$$

Finally, we can use the Lorentz force as in Equation 2.6 for a magnet which is free of electric field by equating its magnitude to the centrifugal force: $q\nu B = m\frac{\nu^2}{\rho}$ to solve for the reference momentum. As a result, the normalised strength in Equation 2.36 for a multipole magnet with the length (i.e. integration path) l will result in:

$$K_n = \frac{B^{(n)} l}{B\rho}, \tag{2.38}$$

by using short-hand notation for the derivative. The denominator is known as *magnetic rigidity*:

$$B\rho = 3.3356 \times E[\text{GeV}] \tag{2.39}$$

which is again another interpretation of the Lorentz force in practical units. To illustrate, a quadrupole focuses the beam with a focal length $f = 1/K_1$ as a beam of light is focused by an optical lens.

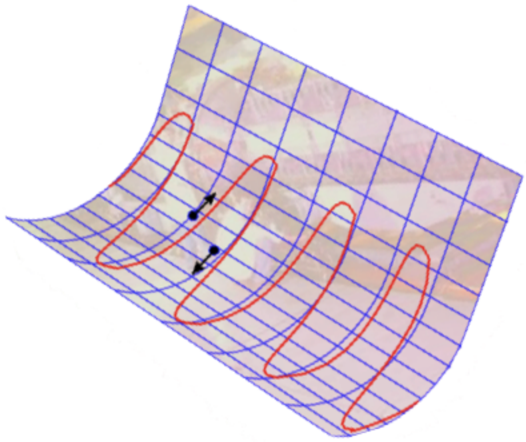

Figure 2.4. The particles inside the accelerator oscillate due to the quadrupole (de)focusing impact, analogically resembling to the motion of a ping-pong ball in a gutter [17].

2.3. Tranverse Motion and Betatron Oscillations

The transverse motion of a particle in an accelerator is controlled by the multipole magnets creating a pseudo-harmonic oscillator known as *Hill's equation* in which the field strength K varies strongly with the direction of propagation s as follows:

$$x'' + K(s)\ x = 0, \tag{2.40}$$

Similarly, it yields $y'' + K(s)\ y = 0$ for the y-axis. A depiction of motion inside the accelerator is presented in Figure 2.4. The solution of Equation 2.40 is as follows:

$$x = \sqrt{\epsilon\beta(s)}\cos(\varphi(s) + \varphi_0), \tag{2.41}$$

and its first derivative with respect to s with $\varphi = \varphi(s) + \varphi_0$ is:

$$x' = \frac{1}{2}\beta'(s)\sqrt{\frac{\epsilon}{\beta}}\cos(\varphi) - \varphi'\sqrt{\epsilon\beta}\sin(\varphi), \tag{2.42}$$

However, before defining the parameters above, we will rearrange x' as follows:

$$x' = -\alpha\sqrt{\frac{\epsilon}{\beta}}\cos(\varphi) - \sqrt{\frac{\epsilon}{\beta}}\sin(\varphi), \tag{2.43}$$

where Twiss parameter α and phase advance φ are defined, respectively as follows:

$$\alpha = -\frac{1}{2}\beta' \tag{2.44}$$

$$\varphi = \int_{s_0}^{s_1} \frac{ds}{\beta(s)}. \tag{2.45}$$

In order to obtain ϵ (i.e. emittance), we can multiply $x_{max} = \sqrt{\epsilon\beta(s)}$ and its corresponding canonic $x'_{max} = \sqrt{\frac{\epsilon}{\beta}}$ for the case α is zero. Therefore, the emittance in a sense is the area of the phase space ellipse if we multiply it by π. The community diverges in whether to add or omit the factor of π in the unit of emittance, yet π.mm.mrad is generally accepted[2] . The horizontal phase space is shown in Figure 2.5.

Twiss parameters α and β together with the emittance ϵ defines the beam uniquely, in other words, characteristics of a beam can be defined with these 3 independent parameters. The third Twiss parameter γ is a dependent parameter as $\gamma = \frac{1+\alpha^2}{\beta}$. Considering Equations 2.44 and 2.45, we can conclude that optics design of an accelerator is basically the proper choice of the β-function. Actually, setting a β-function defines the boundaries of the particles with respect to the *synchronous particle* such as:

$$x_{max} = \sqrt{\epsilon\beta(s)}. \tag{2.46}$$

[2]The short hand notation μm as equivalent of π.mm.mrad will be used throughout the thesis.

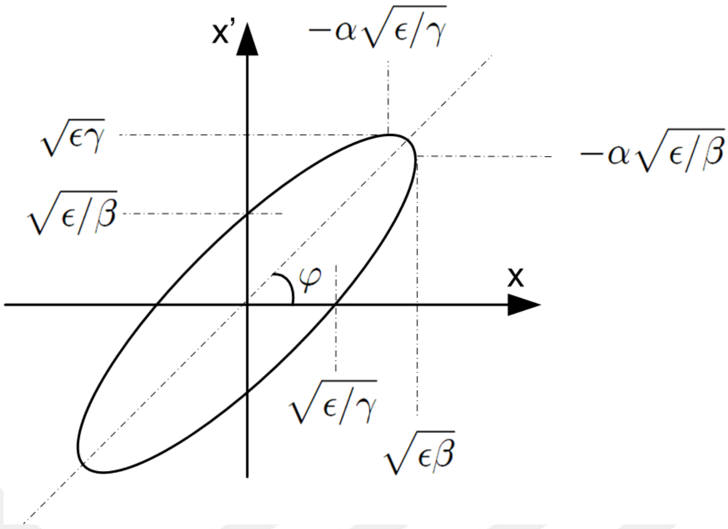

Figure 2.5. Horizontal Phase Space and Courant-Synder Twiss Parameters [18].

Equation 2.46 defines the maximum (1-sigma) horizontal distance to the reference particle. Hence, the optics design of the accelerator refers to design of *beam envelope* which is also known as *single particle dynamics*, a depiction can be seen as the red see-saw curves in Figure 2.6, and all the particle trajectories will be between this envelope (only positive side of the envelope is shown in this thesis). On the other hand, *tracking* is a multi-particle simulation in which each particle is propagated through the designed accelerator element, as the trajectories depicted in Figure 2.7.

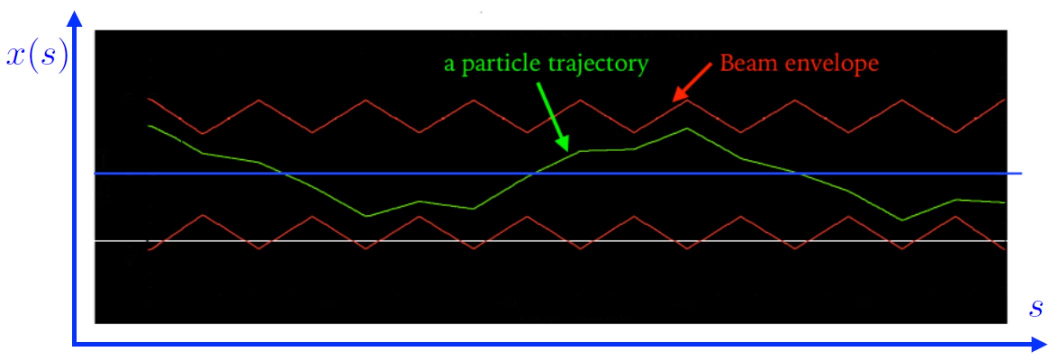

Figure 2.6. Beam envelope and a particle trajectory through the accelerator [20].

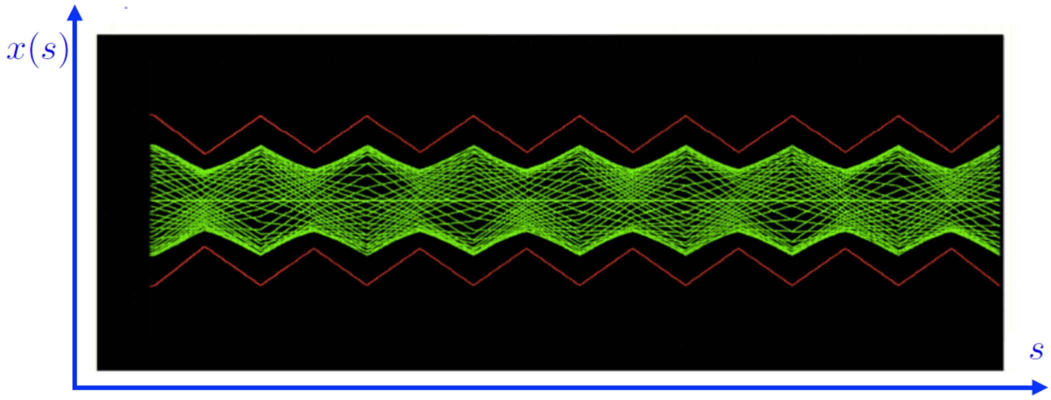

Figure 2.7. Multi-particle tracking where each green line symbolises the trajectory of a particle [20].

2.3.1. Conservation of Emittance and Adiabatic Damping

The Courant-Snyder invariant is a conserved quantity throughout a beam transport with no energy gain or loss [19]. It is given by:

$$\frac{A}{\pi} = \epsilon(s) = \beta x'^2 + 2\alpha x x' + \gamma x^2, \tag{2.47}$$

where ϵ is the geometric emittance if it is not stated otherwise via a subscript, which is calculated by tracking 6D vector of the multi-particle beam using the *rms* (root-mean-square) formula:

$$\epsilon_{rms} = \sqrt{< x^2 >< x'^2 > - < xx' >^2}, \tag{2.48}$$

where the Twiss (i.e. Courant-snyder) parameters are:

$$\alpha = -\frac{< xx' >}{\epsilon_{rms}}, \tag{2.49}$$

$$\beta = \frac{< xx >}{\epsilon_{rms}}, \tag{2.50}$$

$$\gamma = \frac{< x'x' >}{\epsilon_{rms}}. \tag{2.51}$$

The emittance is a conserved quantity of linear transformation, yet the beam is supposed to get accelerated, namely gain energy. Therefore, the conserved quantity of the motion including acceleration due to Liouville's Theorem [18] is the *normalized emittance*:

$$\epsilon_{norm} = \beta_{rel}\gamma_{rel}\epsilon_{rms}. \tag{2.52}$$

As the particles gain energy, β_{rel} will increase and asymptotically approach to 1 while γ_{rel} gets bigger and bigger in Equation 2.52. Therefore, since the normalized emittance is constant, the geometric emittance is getting smaller during acceleration. This shrinkage is called *adiabatic damping*, yet this process does not contain any radiation damping, which will be described in Section 2.6. Instead, the adiabatic shrinkage stems from the fact that the momentum in x stays the same while the acceleration extends the momentum vector along z, as a result, the divergence of the beam, and thus, the geometric emittance gets smaller. On the other hand, for instance in a damping ring, the synchrotron radiation results momentum decrease in all dimensions, yet the restoration of the momentum occurs solely along z. Therefore, the beam emittance cooling can be said to happen in a similar fashion yet stemming from different processes.

The concept of emittance is one of the most important quantity in accelerator physics. It plays a very significant role in the transfer of the beam between the accelerators or even from one cavity to another. Usually, the rms emittance of the beam is calculated and given, as we did in Equation 2.48. However, the rms refers to 1-sigma of the beam, in other words, 39% of the beam, therefore 4 times of the rms would represent 87%, or more generally regarded acceptance is 6 times of rms referring to 95% [21]. Therefore, the acceptance of an accelerator or cavity should be several times bigger than the rms emittance, as can be visualized in Figure 2.8.

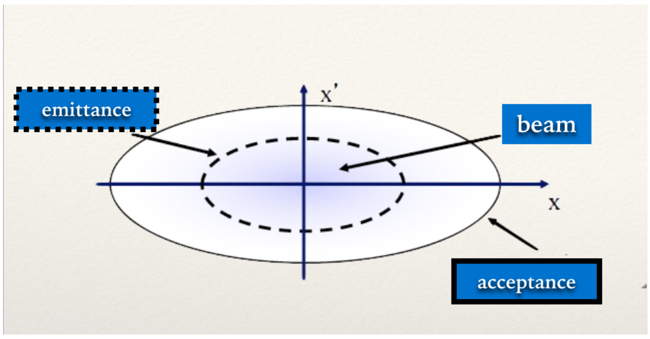

Figure 2.8. The beam is dense near the reference particle and dilutes further away. Therefore, emittance refers to a fractional area of the beam, acceptance is several times the emittance describes how much of the beam is enclosed.

2.4. Dispersion and Slippage Factor

Up to now, we have actually assumed that all the particles have the same momentum p_0 as the synchronous particle. However, the energy spread in the bunch will lead some portion of the bunch to experience different bending, acceleration as well as transverse focusing. Spectroscopically, more energetic particles are bent less, and as a result follow a larger radius orbit in a circular accelerator, a depiction is presented in Figure 2.9. Therefore, the orbit or the designated circumference C_0 will change in accordance with the momentum spread as follows:

$$\frac{\Delta C}{C_0} = \alpha_p \frac{\Delta p}{p_0}, \tag{2.53}$$

where α_p is the *momentum compaction factor*, also it is useful to recall that $\frac{\Delta p}{p} = \delta$. Therefore, Hill's equation in Equation 2.40 will also be altered:

$$x'' + K(s)x = \frac{1}{\rho}\delta, \tag{2.54}$$

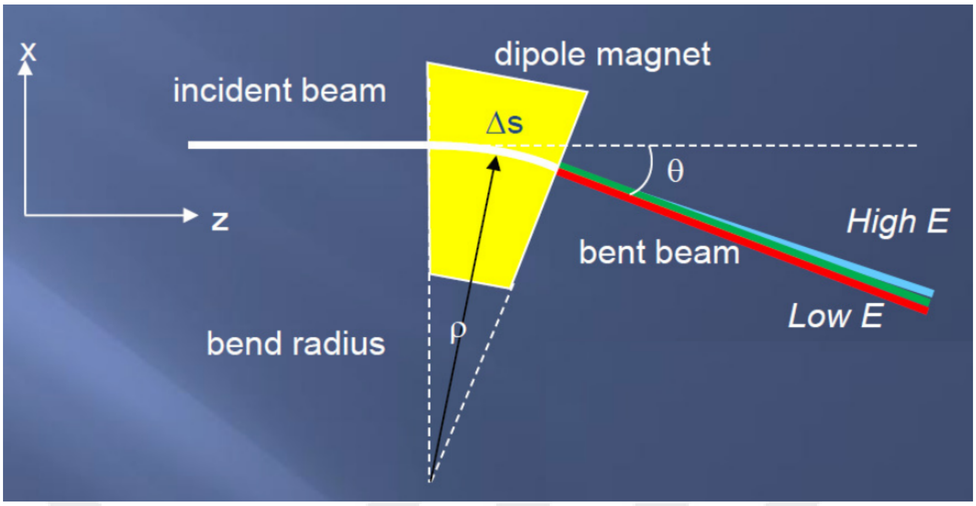

Figure 2.9. Bending magnet acts like an optical prism leading to observation of a spectrum for different energetic particles in a bunch [22].

The solution of Equation 2.54 will change the maximum horizontal 1-sigma distance stated in Equation 2.46 as follows:

$$x = x_\beta + \eta\delta. \tag{2.55}$$

where x_β is the horizontal location of the particle due to betatron function which is in Equation 2.46, and η is the dispersion function obeying:

$$\eta'' + K(s)\eta = \frac{1}{\rho}. \tag{2.56}$$

Equation 2.56 can be considered to describe the *off-momentum particle motion.* All in all, the horizontal beam width gets bigger due to dispersion, as follows:

$$\sigma_x^2 = \beta\epsilon_x + \eta^2\delta^2. \tag{2.57}$$

Therefore, the horizontal beam width is changed by:

$$\Delta x = \eta\delta = \eta \frac{\Delta p}{p}. \tag{2.58}$$

The compaction factor is determined by the lattice design which can be calculated over the new orbit:

$$\alpha_p = \frac{1}{C_0} \oint \frac{\eta}{\rho} ds = \frac{I_1}{C_0}, \tag{2.59}$$

where $I_1 = \oint \frac{\eta}{\rho} ds$ is the *first synchrotron radiation integral.*

The bending in horizontal axis curves the longitudinal trajectory. Some particles with different energy will diverge from the reference particle by an amount of $\eta\delta$. That might create delays to the arrival times into the cavity, therefore dispersion also affects the energy gain and synchronisation of the particles in a bunch. As a result, we need to define the *slippage factor* which depends on the lattice as well as beam energy, as follows [3]

$$\eta_p = \frac{1}{\gamma_T^2} - \frac{1}{\gamma_{rel}^2} = -\frac{\Delta f / f_0}{\Delta p / p_0}, \tag{2.60}$$

where γ_T is relativistic factor for the *transition energy* and defined by the lattice as $\gamma_T = \frac{1}{\sqrt{\alpha_p}}$, and where f_0 is the revolution frequency calculated by dividing nominal circumference of the synchrotron by the particle speed. Therefore, the particles in a constant magnetic field will behave differently whether their energy is below the transition energy or not. The possible cases are as follows:

- Positive η_p refers to below transition during which the revolution frequency increases as momentum increases.
- $\frac{1}{\gamma_{rel}} = \sqrt{\alpha_p}$ is the transition case, and η_p is zero.
- Negative η_p corresponds to above transition case in which, the revolution frequency decreases as momentum increases.

[3] It is noteworthy to state that η_p and the dispersion function η are not the same parameters.

The phase transition is particularly important for the proton/ion machines, since their energy might be below transition in the pre-injectors. For instance, the proton synchrotron (PS) of CERN accepts the beam at 1.4 GeV and ejects at 26 GeV to fill the SPS in the injector chain of the LHC. However, the PS lattice imposes the transition energy to occur at 6 GeV. Therefore, during ramp-up in the PS, the RF cavities with phase ϕ_s needs a phase jump to $(\phi - \pi)$ to keep the particles together longitudinally when the sign of the η_p is inverted [23]. On the other hand, the compaction factor for a lepton synchrotron is at the order of 10^{-4}-10^{-5} yet considering high γ_{rel}, it can be concluded that the lepton synchrotron is usually above transition and needs no phase jump in the RF system.

2.5. Longitudinal Motion

2.5.1. EM Field in Cylindrical Cavity

Transverse oscillations are controlled by the magnets and by controlling transverse dynamics, some particles can be altered longitudinally as well, just in the case of the chromatic correction done by the sextupoles which will be discussed in Section 2.7. However, the magnetic field does not do work since the force associated with the magnetic field, $\vec{F}_{mag} = q(\vec{v} \times \vec{B})$ is always perpendicular to the motion. Therefore, particles can only gain energy from the electric field available in the cavities. The most convenient EM mode for the acceleration is the TM_{010} where the magnetic field is in transverse plane, and the electric field is in longitudinal direction in a cylindrical cavity. The EM field components for TM_{010} in cylindrical coordinates are:

$$E_r = 0, \tag{2.61}$$

$$E_\theta = 0, \tag{2.62}$$

$$E_s = E_0 J_0(kr)\sin(\omega t + \phi_0), \tag{2.63}$$

$$B_r = 0, \tag{2.64}$$

$$B_\theta = \frac{E_0}{c} J_1(kr)\cos(\omega t + \phi_0) \tag{2.65}$$

$$B_s = 0, \tag{2.66}$$

where J_0 and J_1 are Bessel functions of the first kind of zeroth and first order, respectively. Also, the angular cavity frequency and wave number are $w = k/c$ and $k = J_0/a$, respectively. The field amplitude E_0 is assumed to be constant, and ϕ_0 is the cavity phase. Actually, during the acceleration of particles, energy in the structure is transferred to the particles resulting in a drop in the cavity voltage. This effect is known as *beam loading* and need to be compensated so that the posterior bunch gains the same amount of energy as the prior bunch, which will be discussed in details in Section 5.8.

2.5.2. Acceleration and Longitudinal Dynamics

A particle gains energy while traversing in an RF accelerating structure consisting of a series of cavities in which the EM field of mode TM_{010} oscillates and creates a voltage V_{rf} in the structure. The TM_{010} mode in a cylindrical cavity consists of the longitudinal electric field and the transverse magnetic field. The longitudinal electric field leads to acceleration, and the transverse magnetic field results in a *weak focusing* transversely which can be neglected by referring to the speed of light in the denominator in Equation 2.65. Longitudinal dynamics in a linac is comparably easy and synchronization condition is basically to require that the spacing between the cavities obey $L = h\beta_{rel}\lambda$ where h is the harmonic number, λ is the wavelength of the cavity operation frequency. The energy gain is associated with the cavity phase, for instance if the reference particle arrives at the cavity with a phase ϕ_s, it gains an energy equal to:

$$\Delta E = qV_{rf}\sin(\phi_s). \tag{2.67}$$

The longitudinal dynamics in a synchrotron is rigorous due to many turns, and therefore, many passes through cavities in the presence of energy deviation amongst the particles of a bunch. The chromatic momenta of the particles result in orbit change in synchrotrons, in other words there will be a delay in the arrival time of the particles at the cavities, therefore they will experience varying energy gain. The delay may lead the bunch to be elongated and even lead to beam loss. Therefore, the longitudinal motion of the particles needs to have *synchronism*, and this is possible by choosing the right phase for the acceleration to manipulate the location of the particles in a bunch and consequently their energy gain. The longitudinal displacement due to the delay resulting from the momentum deviation is:

$$\Delta z = \frac{C_0}{\beta_0} - \frac{C}{\beta_{rel}}, \tag{2.68}$$

where $C = \beta_{rel}cT$ is the circumference covered at a period T by the particle having speed $\beta_{rel}c$, and the parameters with subscript zero are corresponding counterparts for the synchronous particle. Therefore, we can approximate the following:

$$\frac{dz}{ds} \approx \frac{\Delta z}{C_0} = \frac{1}{\beta_0}\left(1 - \frac{T}{T_0}\right). \tag{2.69}$$

Here, the period change can be Taylor expanded as following:

$$\frac{T}{T_0} = 1 + \eta_p\delta_p + \eta_p^{(n)}\delta_p^{(n)} + \cdots . \tag{2.70}$$

Using Equation 2.70, we can approximate Equation 2.69 as follows:

$$\frac{dz}{ds} \approx -\eta_p\frac{\delta_p}{\beta_0} = -\eta_p\delta, \tag{2.71}$$

where small momentum deviation δ_p is interchanged with the energy deviation δ by assuming $\delta_p \approx \delta\beta_0$ which is a fair approximation for the relativistic case of electron and positron beams. Equation 2.71 defines the spatial motion in z-axis. On the other hand, the equation of motion for the momentum can be easily constructed. Assuming that the cavity phase is ϕ_{rf} when the synchronous particle arrives at the cavity, the non-synchronous particle will exploit the field will arrive with a time difference of $\frac{\omega_{rf}z}{c}$, it is crucial to re-state that the position z is the longitudinal distance to the synchronous particle which is ideally assumed to catch the RF phase ϕ_{rf}. Therefore, the difference in energy gain for a non-synchronous particle becomes:

$$\Delta\delta = \frac{qV_{rf}}{cP_0}\sin\left(\phi_{rf} - \frac{\omega_{rf}z}{c}\right). \tag{2.72}$$

Equation 2.72 describes the energy deviation amongst diverse energetic particles in a generic way. Especially for the circular lepton machines, we need to also include the energy loss due to the synchrotron radiation (SR) over a circumference C_0. SR will be discussed in Section 2.6, yet we can simply assume the energy loss through one turn around a ring with circumference C_0 is U_0, therefore Equation 2.72 can be written:

$$\frac{d\delta}{ds} = \frac{qV_{rf}}{cP_0C_0}\sin\left(\phi_{rf} - \frac{\omega_{rf}z}{c}\right) - \frac{U_0}{cP_0C_0}. \tag{2.73}$$

All in all, we have also achieved the equations of motion (i.e. Equation 2.71 and Equation2.73) for a synchrotron storage ring, as well. As in the case of transverse betatron oscillations, a controlled (mainly by the cavity) oscillatory motion also occurs in the longitudinal direction. In order to obtain the frequency of the oscillation, we can take the derivative of Equation 2.71 and substitute Equation2.73 into it, as follows:

$$\frac{d^2\delta}{ds^2} = -\eta_p\frac{qV_{rf}}{cP_0C_0}\sin\left(\phi_{rf} - \frac{\omega_{rf}z}{c}\right) + \eta_p\frac{U_0}{cP_0C_0}. \tag{2.74}$$

Recalling that the synchronous particle phase is set to the RF phase as $\phi_s = \phi_{rf}$, with

$$\sin\phi_s = \frac{U_0}{qV_{rf}}, \tag{2.75}$$

and making small angle approximation in Equation2.74, we will achieve the *harmonic motion* as:

$$\frac{d^2\delta}{ds^2} = -k_z^2 z, \tag{2.76}$$

where

$$k_z^2 = -\frac{qV_{rf}}{cP_0}\frac{\omega_{rf}}{cC_0}\eta_p \cos\phi_s. \tag{2.77}$$

Therefore, the longitudinal motion is stable if $k_z^2 > 0$, stating that

$$qV_{rf}\eta_p \cos\phi_s < 0, \tag{2.78}$$

here, the slippage factor η_p is typically at the order of 10^{-4}-10^{-5} for a storage ring (resulting from the lattice design) above transition and therefore Equation 2.78 and synchronous phase must satisfy $\frac{\pi}{2} < \phi_s < \pi$ for the stability. The overall Hamiltonian resulting in the equations of motion in Equation 2.71 and 2.73 can be calculated.

$$H = \frac{qV_{rf}}{\omega_{rf}cP_0}\left(\sin(\phi_s)\frac{\omega_{rf}z}{c} - \cos\left(\phi_s - \frac{\omega_{rf}z}{c}\right)\right) - \frac{1}{2}\eta_p\delta^2. \tag{2.79}$$

Equation 2.79 can be plotted by letting (z, δ) as free parameters, as shown in Figure 2.10 [14]. Figure 2.10 asserts that the longitudinal motion is stable when the contours are closed and do not intercept with the others. Therefore, the biggest closed contour refers to the *longitudinal acceptance*.

2.6. Synchrotron Radiation

Particles radiate photons once their present course is disturbed, and the energy of the emitted photons or energy lost from the particles is called *synchrotron radiation* (SR). The particles radiate more when they are bent dramatically from their present

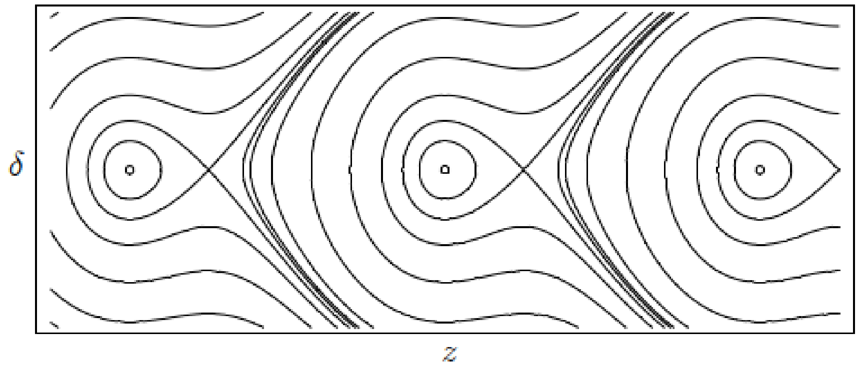

Figure 2.10. Hamiltonian as a function of δ and z. These contours can be considered as describing the longitudinal motion, with closed curves called *RF buckets*. Each RF bucket, deliminated in the figure by its *seperatrix*, is spaced by one RF wavelength [14].

trajectory. The radiation power is given by the Larmor formula [24]:

$$P = \frac{q^2}{6\pi\varepsilon_0 m_0^2 c^3}(\dot{p}_{\parallel}^2 + \gamma_{rel}^2 \dot{p}_{\perp}^2), \tag{2.80}$$

where $\dot{p}_{\parallel}$ stands for the momentum change in the direction of propagation, while $\dot{p}_{\perp}$ is perpendicular to the motion. Therefore, the energy loss through a trajectory L will be dominated by the acceleration perpendicular to the particle motion and will follow:

$$W = \int_L \frac{P}{\nu} ds \approx \frac{4\pi r_e}{3(m_0 c^2)^3} \frac{E_0^4}{\rho}, \tag{2.81}$$

and energy loss per turn for an electron in a constant magnetic field in practical units:

$$U_0 \text{ [keV/turn]} = 88.46 \frac{E_0^4 [\text{GeV}]}{\rho[\text{m}]}. \tag{2.82}$$

The damping ring (DR) cools the beam emittance in 3 dimensions thanks to synchrotron radiation and acceleration of the particles along z-axis in the cavity. Therefore, its energy as well as radius are determined primarily based on Equation 2.82, as will be discussed in detail in Chapter 7. Moreover, there are also *wiggler magnets* which are series of dipoles which create small orbit bumps where the radiation occur, as depicted in Figure 2.11.

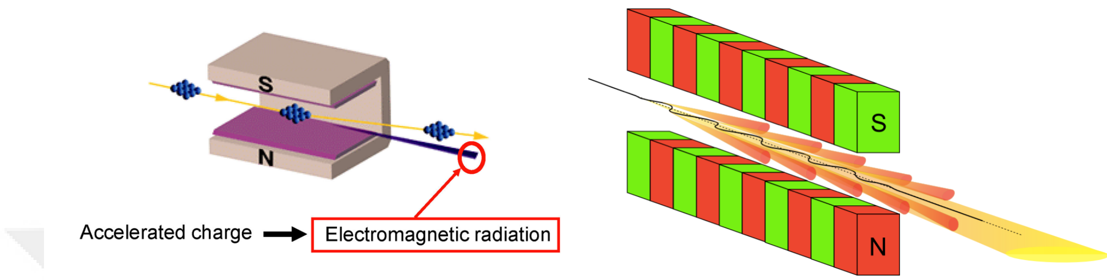

Figure 2.11. Synchrotron radiation from a dipole (left), and a cone of radiation stemmed from a series of dipoles, so-called wiggler magnet (right). Credit: L. Rivkin, and [25].

Taking synchrotron radiation into account is also crucial for the design of an electron ring as it limits the reachable energy of a circular lepton accelerator, just like in the case of the FCC-e^+e^- collider. The radiated power results in heating on the beam screen, which needs to be cooled. The dissipated energy needs to restored back to the particles to keep them in the orbit. Apart from the restoration energy, more RF power is needed to further accelerate the particles, however as the particles' energy get increased, they will radiate even more, proportional to the fourth power of their energy. In a very radiative synchrotron, the magnet strengths are needed to be *tapered* in an accordance with the local energy at that magnet[4] . In other words, energy loss through an arc needs to be estimated and/or monitored and the magnet strengths need to be lowered compared to the bare lattice design.

[4]Recall that any deviation from the present trajectory causes the beam to radiate. For a high energy lepton collider, such as the FCC-e^+e^-, the SR due to quadrupole and sextupole magnets needs to be also taken into account.

2.6.1. Quantum Excitation

Basically, synchrotron radiation is a release of photons which are emitted with a discrete energy, the discrete diffusion of the bunch energy results in a random motion in the bunch amongst the particles, resulting in so-called *quantum fluctuations* [26]. Typically, the circular lepton accelerators are built parallel to the ground, in other words, the beam is bent through the horizontal axis, so the quantum excitation becomes the dominant reason for the equilibrium emittance and beam width in horizontal direction, and it is negligible in the vertical axis resulting in a *ribbon* like electron or positron beams. Actually, the vertical equilibrium emittance of a synchrotron ring stems from the coupling of x-y axes. This partial transverse coupling can be due to the random imperfections or can be created intentionally as in the FCC-e$^+$e$^-$ damping ring.

2.7. Tune, Chromaticity and Resonances

The motion of a particle in a circular accelerator dictates the periodicity of the β-function, however periodicity is not required for the phase advance. The circular motion can be easily interrupted leading to a non-ideal trajectory due to any imperfection in the lattice. For instance a dipole kick due to a misaligned quadrupole, will drive the beam to a *resonance* and result in particle loss eventually due to the impact pile-up on the beam throughout many turns in the machine. All in all, the resonances in synchrotrons are needed to be well defined and manipulated. To start with, the motion from s_0 to s_1 in a circular accelerator can be defined:

$$\begin{pmatrix} x(s_1) \\ x'(s_1) \end{pmatrix} = \begin{pmatrix} a & b \\ c & d \end{pmatrix} \cdot \begin{pmatrix} x(s_0) \\ x'(s_0) \end{pmatrix}, \tag{2.83}$$

where $x(s_0) = \sqrt{\epsilon\beta}\cos(\varphi)$ and $x' = -\alpha\sqrt{\frac{\epsilon}{\beta}}\cos(\varphi) - \sqrt{\frac{\epsilon}{\beta}}\sin(\varphi)$ are the solution for the Hill's equation in Eqs. 2.41 and 2.43, respectively. The counterparts for the location s_1 are:

$$x(s_1) = \sqrt{\epsilon\beta}\cos(\varphi + \mu), \tag{2.84}$$

$$x'(s_1) = -\alpha\sqrt{\frac{\epsilon}{\beta}}\cos(\varphi+\mu) - \sqrt{\frac{\epsilon}{\beta}}\sin(\varphi+\mu), \tag{2.85}$$

where μ is the total betatron phase advance over one complete turn. Recalling the periodicity condition for the betatron function $\beta(s_1) = \beta(s_0)$ in a circular accelerator, the transport matrix in Equation 2.83 will result in:

$$\begin{pmatrix} a & b \\ c & d \end{pmatrix} = \begin{pmatrix} \cos\mu + \alpha\sin\mu & \beta\sin\mu \\ -\gamma\sin\mu & \cos\mu - \alpha\sin\mu \end{pmatrix}. \tag{2.86}$$

Thus, Equation 2.86, *one turn matrix*, will depend on the initial point s_0 yet will transport the (x, x') doublet over one complete turn around the machine. It is also noteworthy to define the *tune* of the machine, which is the number of betatron oscillations per turn:

$$Q = \frac{\mu}{2\pi}. \tag{2.87}$$

For instance, $Q = 23.25$ corresponds to complete 23 oscillations and a quarter where quarter refers to $\pi/2$ phase advance. This quarter will lead the beam oscillation to repeat itself after 4 turns. Generally, the integer part of the tune is neglected, and the *fractional tune* is associated with the resonances. The order of a resonance is defined as n:

$$n \times Q = \text{integer}. \tag{2.88}$$

Hence, our example of a machine with the tune $Q = 23.25$ has the 4^{th} order resonance. The resonance in this case can be defined as the enhancement to the amplitude of the oscillation due to the imperfections. For instance, a dipole kick error in the machine which is set to an integer tune such as $Q = 23$, will result in a shift in the beam phase space both in (x, x'), causing the beam to leave the acceptance of the machine. For this reason, it will be said that the beam is lost due to the 1^{st} order resonance. For example, the revolution frequency of the beam in the LHC is 11 kHz. Thus, if there is a 1 mm horizontal kick to the beam, this kick will become 11 meters in 1 second, whereas the beam pipe radius is 23 mm causing the beam to be lost in a very small fraction of a second if the LHC was set to an integer tune. On the other hand, $Q = 23.5$ would have been stable to the dipole error since the beam will experience one time positive kick and once negative kick which will cancel each other at the next turn. However, the circular machine also have quadrupole magnets and their imperfection will also result in a resonance which is order of 2^{nd}. To sum up, the motion is stable if the resonance order n is bigger at least by two than the magnet order n, such as machine containing sextupole $n = 2$ (see Equation 2.32) magnet should have $Q = .25$ fractional tune (i.e. the decimal part of the tune) referring to $n = 4$ resonance. However, choosing a tune, also known as *working point* selection is not only bounded to the resonance line but it needs to be an island in the tune diagram since tune shift is inevitable in a lepton synchrotron due to the radiation. The typical tune diagram consists of sum of both horizontal and vertical tunes (i.e. Q_x and Q_y, respectively) in order to avoid mutual amplification of horizontal and vertical betatron oscillations due to the coupling of the planes. Therefore, the working point of a circular accelerator should also avoid:

$$aQ_x + bQ_y = \text{integer}. \tag{2.89}$$

where a and b are integers, and the resonance order is given by $a + |b|$. Therefore, not only the sum but also the difference of the transverse tunes should not be an integer. If Equation is plotted, it will be easier to locate the working point which does not intercept any of the resonance lines, as illustrated in Figure 2.12.

The working point is optimized during lattice design. Nonetheless, a profound beam optics design should allow the operator to be able to scan the tune and find the most optimum working point of the real accelerator. The tune scan is generally done with the quadrupoles at the straight section of the circular accelerator. Normally, the quadrupoles in the arc are powered together, those magnets are said to form *one family* of quadrupoles, yet the quadrupoles at the straight section can be set individually in order to control the tune. Furthermore, recalling the quadrupole strength in Equation 2.38 and the beam rigidity in Equation 2.39, we can state that the momentum

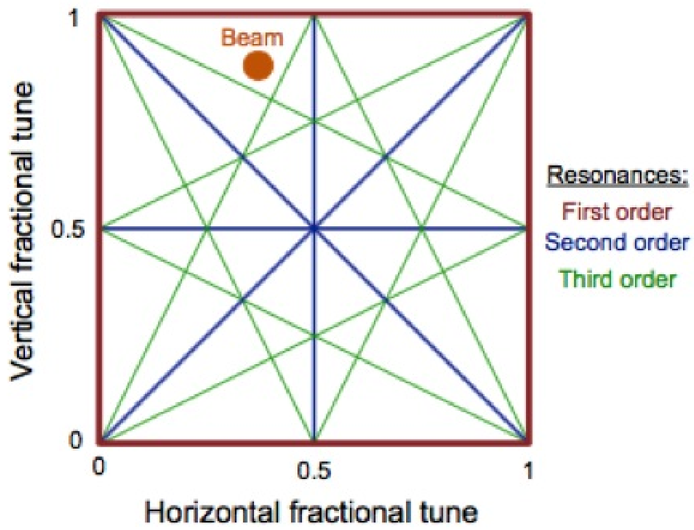

Figure 2.12. Tune diagram showing resonances up to third order, and arbitrarily chosen working point for the beam is shown. Notice that the working point is not just a dot but an island bounded by the third order resonances allowing the tunes to have a safety margin to the resonance lines when the tunes are shifted during operation.

spread in beam also causes spread in focusing strength:

$$\frac{\Delta k}{k} = -\frac{\Delta p}{p}, \tag{2.90}$$

which follows the equation below since the tune depends on the quadrupole gradient up to a constant:

$$\frac{\Delta Q}{Q} = \xi \frac{\Delta p}{p}, \tag{2.91}$$

where the constant ξ is the *chromaticity.* The chromatic impact will result the lower momentum particles to be focused more by a quadrupole magnet, therefore resulting in a higher betatron oscillation over one turn corresponding to a higher tune. Therefore, the chromaticity needs to be controlled, which is done by the sextupole magnets. In order to find an explicit chromaticity relation, we need to start with the tune change due to small focusing quadrupole gradient change Δk with length ds [17]:

$$\Delta Q = \frac{1}{4\pi}\beta \Delta k ds, \tag{2.92}$$

Hence, Equation 2.91 will become as follows by substituting Equation 2.90:

$$\frac{\Delta Q}{Q} = \left(-\frac{1}{4\pi}\beta\frac{k}{Q}ds\right)\frac{\Delta p}{p}. \tag{2.93}$$

Therefore, to correct chromaticity we need a magnet which will focus the higher momentum particles more, and focus lower momentum particles less. In the end, the off-momentum particles trajectories will approach to the reference particle trajectories. The magnet which corrects chromaticity is the sextupole. Indeed, the sextupole magnet supplies a magnetic field $B_y = Cx^2$ from Equation 2.32 where C is a constant coefficient. Therefore, the gradient of the sextupole is $k = \frac{1}{B\rho}\frac{dB_y}{dx}$ and the gradient spread Δk will read:

$$\Delta k = \frac{2C}{B\rho}\Delta x. \tag{2.94}$$

where the change in beam width Δx can be substituted from Equation 2.58 and the coefficient $C = \frac{1}{2}\frac{d^2 B_y}{dx^2}$. All in all, the tune change-chromaticity relation in Equation 2.93 will become:

$$\frac{\Delta Q}{Q} = \frac{1}{4\pi} l\beta(s)\frac{d^2 B_y}{dx^2}\frac{\eta(s)}{(B\rho)Q}\frac{\Delta p}{p}. \tag{2.95}$$

Therefore, if Equation 2.95 is satisfied, the natural chromaticity of the machine can be controlled [17].

2.8. Beam Injection

The transfer of the beam from an accelerator into another is made via beam transfer lines, and the injection can be made using magnets such as a septum and a kicker, as illustrated in Figure 2.13. The septum, as the name evokes, produces a dipole field between two separated regions. The septum can be electrostatic, as well. The kicker is a fast pulsing dipole. For instance, injection from linac into the damping ring requires the damping ring to have an acceptance of the phase space $(3\sigma)^2$ or even $(4\sigma)^2$ of the rms emittance. To illustrate, 1 nm emittance beam can be safely injected into a circular accelerator which has more than 16 nm acceptance. The beam injection also requires matching of Twiss parameters, dispersion function as well as the matching of the time derivative of dispersion function, as can be formulated for an injection from a location s_0 to s_1:

$$(\beta_x, \alpha_x, \beta_y, \alpha_y, \eta, \eta')_{s_0} = (\beta_x, \alpha_x, \beta_y, \alpha_y, \eta, \eta')_{s_1}. \tag{2.96}$$

Figure 2.13 is a comprehensive depiction of the safe injection mechanism which refers

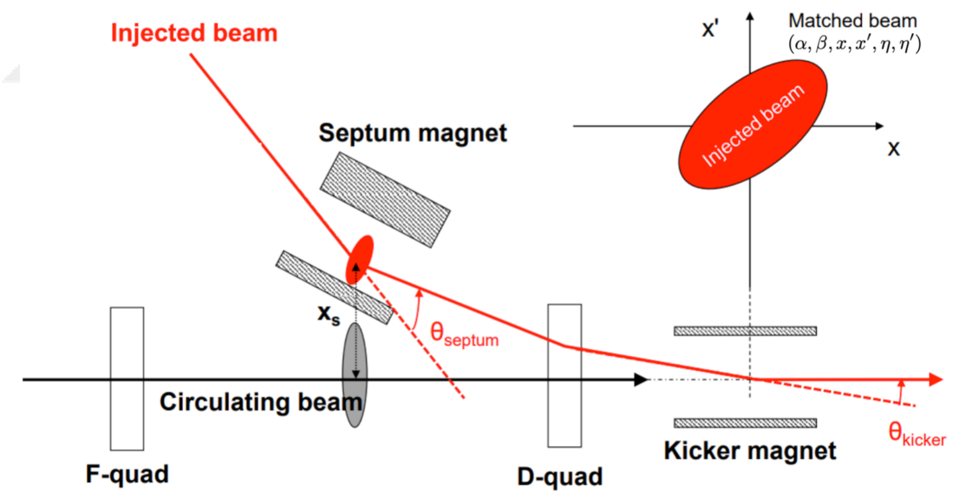

Figure 2.13. An illustration of single-turn injection in which the beam is sent to defocusing quad by the septum magnet, and the kicker magnet kicks the beam onto the reference axis [27].

to the injection without beam loss. The on-axis injection requires the injected beam to have the position at the septum x_s which must be larger than the sum of the followings [27]:

- injected beam envelope,
- circulated beam envelope,
- thickness of the septum blade,
- beam size increase due to the energy spread,
- closed orbit distortions,
- alignment errors.

All in all, typically the dominant factors for the injection are the beam size including the dispersion and the septum blade thickness which is typically 3-4 mm. Generally, the clearance to the septum is asked to be 1 mm. A picture of the CERN PS septum is presented in Figure 2.14.

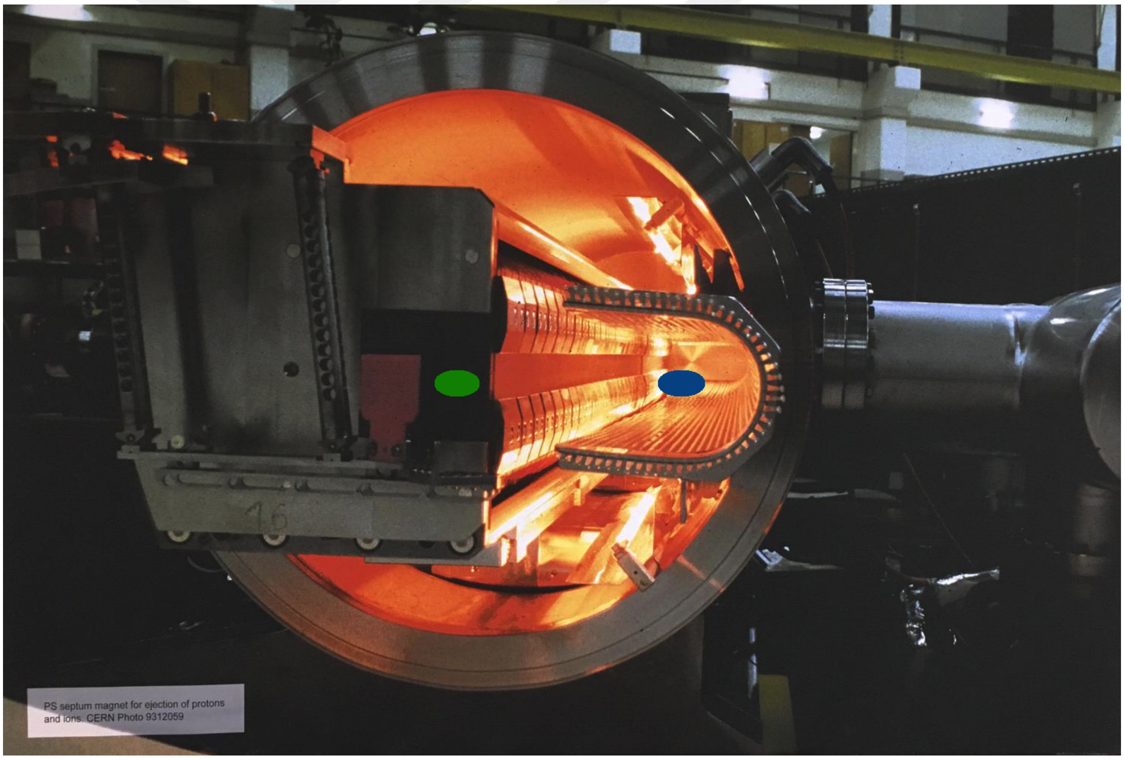

Figure 2.14. Septum magnet of the CERN PS. The green ellipse refers to the ejected beam, while the blue ellipse is the circulating beam. The metallic wall between the beams is the septum blade. Credit: CERN Photo 9312059.

3. COLLECTIVE EFFECTS

The motion of particles in a particle accelerator gets rigorous when the external and internal interactions are included. Especially, for a project like the FCC-e^+e^-, which stands at the very limits of the conventional technology, the collective effects are determinant. Both the charge in a bunch and the total charge in the collider are limited by the collective effects and the synchrotron radiation on the beam screen or pipe. On the other hand, the high bunch charge with low emittance can be regarded as the quality of the beam. This quality actually will bring about higher transmission since the beam is small both in spatial and momentum spaces avoiding the diluting effect of the wakefields. There are a variety of effects categorised as collective effects [28], such as:

- Space charge,
- Wakefields,
- Coherent synchrotron radiation (CSR),
- Scattering,
- Beam-beam collisions,
- Gas ionization,
- Secondary electrons (i.e. electron cloud effect),

and there can be even more considered as collective effects, such as the micron-size dust particles causing beam loss in the LHC, occurences known as *unidentified falling objects* (UFO). We may only cover the first four which have very vital impact on the beam dynamics of the linear and circular accelerators that are the foci of this thesis. We will leave out the discussions of: the beam-beam physics, and gas ionization which is the topic of vacuum. In addition, the electron cloud effect is left to the care of those experts who study the design of the beam screen and inner coating of the beam pipe [29]. Instead, we will concentrate on space charge, wakefields, CSR and briefly mention scattering.

3.1. Space Charge

A particle in a free space creates an electric field around a Gaussian sphere of radius r pointing outwards as:

$$E_r = \frac{q}{4\pi\varepsilon_0}\frac{1}{r^2}. \tag{3.1}$$

However, as the particles are accelerated along the z-direction, the EM field components go through Lorentz transformation due to the boost and become as follows in the cylindrical coordinates (r, θ, z) [30]:

$$E_r(z=0) = \frac{q}{4\pi\epsilon_0}\frac{\gamma_{rel}}{r^2}, \tag{3.2}$$

$$B_\theta(z=0) = \frac{q\beta_{rel}}{4\pi\epsilon_0 c}\frac{\gamma_{rel}}{r^2}, \tag{3.3}$$

$$E_z(r=0) = \frac{q}{4\pi\epsilon_0}\frac{1}{\gamma_{rel}^2 z^2}. \tag{3.4}$$

Therefore, in Equation 3.4, E_z gets contracted as γ_{rel} increases or when it goes away from $z = 0$, as a result it starts resembling a pancake rather than a sphere, as shown in Figure 3.1.

Particles in a bunch are accelerated when they are synchronised to the sinusoidally varying electric field. Therefore, to maximize the gain, the bunch needs to be short in length, so that it can catch the crest of the wave and transversely it needs to be small so that it does not get affected from the emittance diluting effects. Actually, small beam size is the keystone for reaching high luminosities at the first place. Yet, a small bunch needs to overcome the nature of charged particle due to the Coulomb repulsion. In order to model the phenomenon, we assume an ultra-relativistic bunch having a charge distribution along the $x - y$ plane, yet located at the same z location. Using

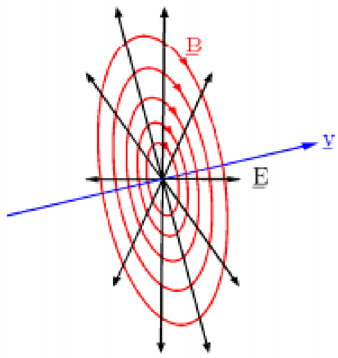

Figure 3.1. The longitudinal component of electric field shrinks as it experiences Lorentz boost along the z-axis [31].

the Bassetti-Erskine formula [32], the approximate transverse electric field components can be found:

$$E_x \approx \frac{e\lambda}{2\pi\varepsilon_0}\frac{x}{\sigma_x(\sigma_x+\sigma_y)}, \tag{3.5}$$

$$E_y \approx \frac{e\lambda}{2\pi\varepsilon_0}\frac{y}{\sigma_x(\sigma_x+\sigma_y)}, \tag{3.6}$$

where $e\lambda$ is the linear charge density in the z-direction and σ_x and σ_y correspond to the rms beam size along the x and y axes, respectively. Moreover, the Lorentz force for a relativistic particle is:

$$\gamma_{rel} m\ddot{y} = e(E_y + \beta_{rel} c B_x), \tag{3.7}$$

where the dots refer to the time derivative. Therefore the derivative with respect to s is linked as $y'' = \frac{\ddot{y}}{\beta_{rel}^2 c^2}$ and using B_x from Equation **??**, the equation of motion for a particle in the relativistic bunch becomes:

$$y'' = \frac{eE_y}{\beta_{rel}^2\gamma_{rel}^3 mc^2}. \tag{3.8}$$

Therefore if we substitute Equation 3.6 into Equation 3.8, and the space charge force acting on y along z can be found as:

$$\frac{dp_y}{ds} \approx \frac{e^2\lambda}{2\pi\varepsilon_0}\frac{y}{\beta^2\gamma^3 mc^2}. \tag{3.9}$$

Hence, we can conclude that space charge creates a repulsive force and vanishes proportional to $1/\gamma_{rel}^2$ as particles gain energy by substituting the normalised emittance $\epsilon_{norm} = \beta_{rel}\gamma_{rel}\epsilon_{rms}$ from Equation 2.52 into Equation 3.9.

3.2. Wakefields

The cavities, beam pipes, diagnostics elements are all mainly metals, thereby they create impedance with respect to the charged beam. Wakefields can be defined as the inverse Fourier transform of the impedance, namely the potential occurring due to the electromagnetic (EM) interaction of the beam with its surrounding environment. The moving charge induces electromagnetic field, and we have already discussed in Figure 3.1, the electric field resembles a pancake for a relativistic particle, and it follows $cB_\varphi = E_r$ when $\nu = c$. Therefore, the image charge created by an ultra-relativistic beam on the perfectly conducting smooth beam pipe will be exactly equal and opposite of the bunch. Hence, there would be no wakefield. Typically, expected smoothness of beam pipe at the order of μm, and surely it is not perfectly conducting, as the particles may not be relativistic enough [33]. Therefore, perfect cancellation of wakefields cannot be achieved.

Actually, the wakefields become a problem when the metallic structure has discontinuity and some EM fields in a sense get trapped in the discontiniuous region resulting in a deflection when the beam enters the structure off-axis [34]. For instance, the accelerating structure consists of cavities (in a sense discontinuities) and the head of an ultra relativistic bunch entering the structure with an offset from the structure's symmetry axis will induce a potential near the cavity aperture. This will deflect the tail of the bunch causing the bunch tail to shape like a gulf club or banana. This deformation will result in the tail oscillating, eventually causing beam break-up instability. This instability was first observed in SLAC cavities, which are similar to what FCC-e^+e^- would utilise, and its depiction is presented in Figure 3.2.

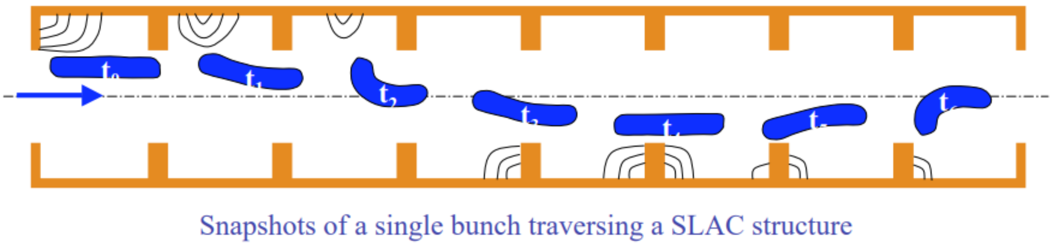

Figure 3.2. Transverse wakefield induced by the head of the bunch causes its tail to wiggle. The shape of the distorted bunch resembles a banana [34].

The preservation of the emittance suffers from the transverse wakefields, while the longitudinal wakefields will affect the tail to gain less energy. Therefore, the phase advance in the cavity needs to be adjusted in a way that the gain of the energy through the bunch length is kept controlled. The phase advance optimisation and suppression of head-tail instability will be discussed in Section 5.2.

The calculation of wakes are of great importance for the simulation of a real-like accelerator. The short-range formulas [35] are used to see the effect within the bunch itself. In Figure 3.3, geometry of a linac structure has been presented where a refers to the cavity aperture, b is the radius of the cavity (i.e. a cell) and g is the gap length. Here, we assume that b is associated with the delay of the reflected wave, and the wakefield calculations are valid for the range s which is limited by $s \leq \sqrt{g^2 + 4(b-a)^2}$. The short-range formulas of the longitudinal and transverse wakefields per unit length can be calculated respectively as follows [35]:

$$W_L(s) = \frac{cZ_0}{\pi a^2}[1 + W_{L_1}\sqrt{\zeta} + W_{L_2}\zeta + W_{L_3}\zeta\sqrt{\zeta}], \tag{3.10}$$

$$W_T(s) = \frac{cZ_0}{\pi a^4}s[1 + W_{T_1}\sqrt{\zeta} + W_{T_2}\zeta + W_{T_3}\zeta\sqrt{\zeta}], \tag{3.11}$$

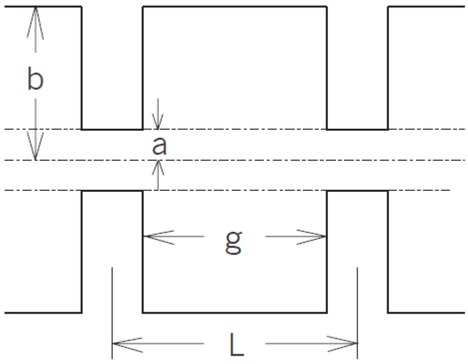

Figure 3.3. Geometric depiction of a traveling wave structure deployed in linac [35].

where c is the speed of light, Z_0=377 Ω is the impedance of the vacuum, and $\zeta = \frac{Ls}{a^2}$, and the coefficients can be parametrised using $r = \frac{a/\lambda}{0.15}$ as follows:

$$W_{L_1} = -1.614r^{0.122}, \qquad W_{L_2} = 1.012r^{0.169}, \qquad W_{L_3} = -0.231r^{0.111},$$
$$W_{T_1} = -2.781r^{0.217}, \qquad W_{T_2} = 1.637r^{0.511}, \qquad W_{T_3} = -0.364r^{0.793}.$$

The FCC-e^+e^- deploys $2\pi/3$ mode cavities, which means in each wavelength λ there are 3 cavities, i.e. the distance L is equal to $\lambda/3$, and λ needs to be replaced by $3L$ if the cavity phase advance is not $2\pi/3$. Using Equations 3.10 and 3.11, we can calculate and plot the longitudinal and transverse wakefields per unit length of the high gradient cavities used for the FCC-e^+e^- linac, respectively in Figure 3.4 and 3.5. Furthermore, in order to implant those wakefields into a linac simulation, for instance in *SAD* [16], we need to multiply those wakes with the length of the accelerating structure.

The impact of the wakefields induced by a bunch is not limited only to the tail of that bunch, but also to the adjacent bunch. For this reason, the bunch-to-bunch spacing in a linac must be adjusted in a way that the effects of the long-range wakefields can be subdued. Since the FCC-e^+e^- linac deploys the same cavities as Stanford Linear

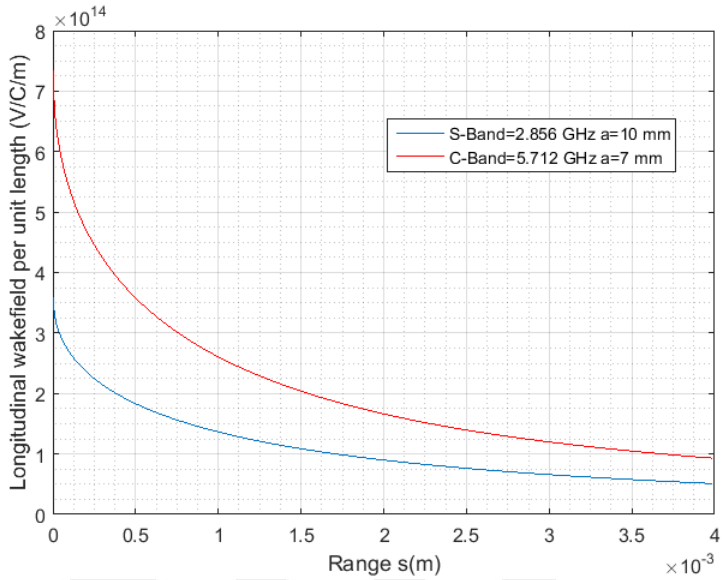

Figure 3.4. Short range longitudinal wakefields per unit length of the linac cavities for the utilised frequencies.

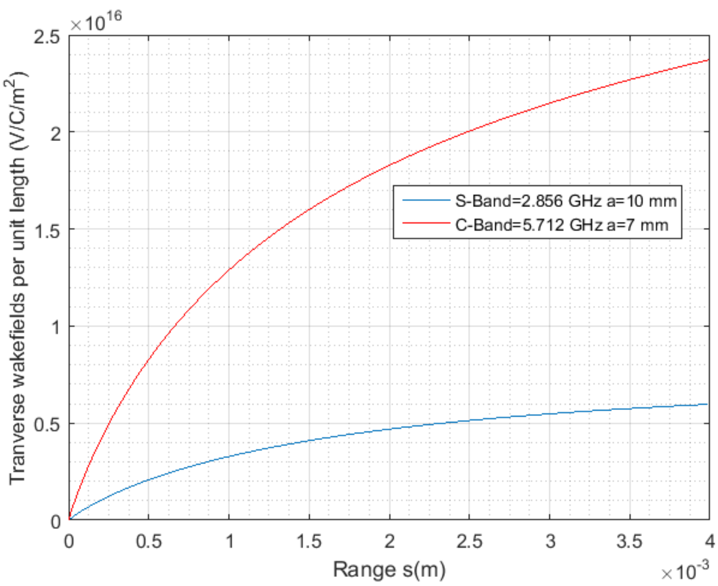

Figure 3.5. Short range transverse wakefields per unit length of the linac cavities for the utilised frequencies.

Collider with similar charges [36], the bunch to bunch spacing in a pulse needs to be about 50 ns where the oscillation of the lowest transverse dipole modes almost flatten, as can be concluded from Figure 3.6. Therefore, this parameter would be determinant in linac bunch to bunch spacing. For this reason, it has a substantial role in the determination of the damping ring circumference, as well.

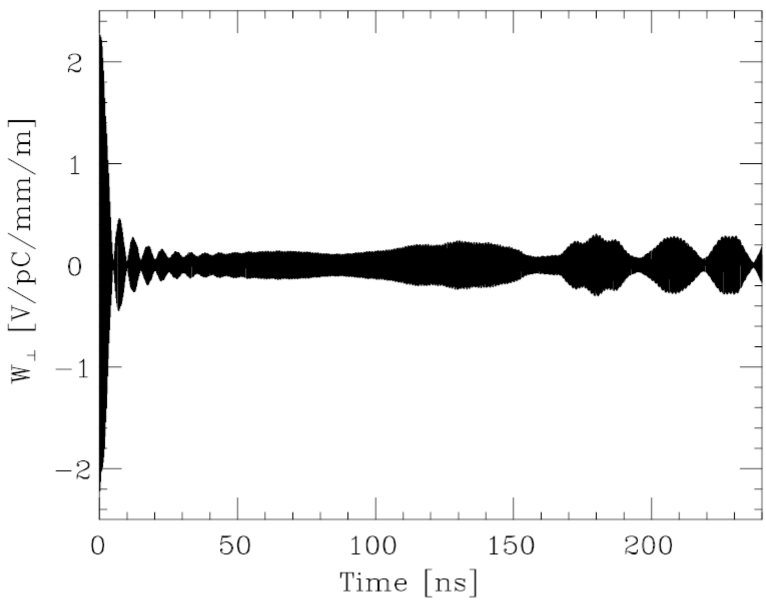

Figure 3.6. Theoretical long-range wakefield calculation of SLAC structure [36].

3.3. Coherent Synchrotron Radiation

The charged particles radiate once their present courses are perturbed. Therefore, the emitted synchrotron radiation culminates through the bends, as we discussed in Section 2.6. The synchrotron radiation (SR) from the bunch results in a superposition of radiation, so-called coherent synchrotron radiation (CSR) if the bunch length of the bunch is smaller than the wavelength of the radiated photons. In other words, a bunch of length σ_z will radiate coherently at wavelengths [37]:

$$\lambda \geq 2\pi\sigma_z. \tag{3.12}$$

Actually, the first observation of the CSR has challenged the theory of the SR that we discussed in Section 2.6. The SR is proportional to the charge as in Equation 2.82, however, the observation of photons with the wavelength comparable to the bunch length has demonstrated a relation proportional to the square of the number of particles N in a Gaussian bunch. The enhancement of the radiated power to the classical SR due to the CSR is [38]:

$$\Delta P_{CSR} \approx 0.028 N^2 \frac{ce^2}{\epsilon_0 \rho^{2/3} \sigma_z^{4/3}}. \tag{3.13}$$

Therefore, Equation 3.13 sets forth that the CSR power will increase if the bunch length σ_z is short, or bending radius ρ is small, or more importantly if the charge of the bunch is high. Indeed, those factors are all demanded for a high quality beam. For better understanding of the phenomena, the CSR can be considered as a retarding potential just like in the case of the wakefield. The CSR acts on the beam, and re-distributes the momentum, causing an additional momentum spread. The bunch head and tail start to exchange photons, yet the power loss will cause the emittance dilution. Therefore, the impact of the CSR needs to be cancelled which can be done with some beam optics techniques [39, 40]. On the other hand, the CSR may even be avoided from the beginning by optimising the bunch length of the beam by decreasing the voltage in the cavity, furthermore the radius of the beam pipe can be also set to a value in which the photons (the SR waves) are not given enough space for superposition.

3.4. Scattering

Regarding the fact that a bunch consists of same charge particles subject to Coulomb interaction, some particles may scatter or collide with other particles in a bunch, resulting in a redistribution of momenta altering the beam emittance. This internal scattering within the beam is called intra-beam scattering (IBS). Reasonably, IBS is likely to occur in a high charge low emittance beams at low energies stored in a circular accelerator. Consequently, IBS may lead to emittance dilution and particle loss. All in all, scattering limits the beam lifetime in an accelerator. The emittance growth with respect to time due to IBS is as follows [31]:

$$\frac{\epsilon_x}{dt} = \frac{2}{T_x}\epsilon_x, \tag{3.14}$$

$$\frac{\epsilon_y}{dt} = \frac{2}{T_y}\epsilon_y, \tag{3.15}$$

$$\frac{\sigma_\delta}{dt} = \frac{2}{T_\delta}\sigma_\delta, \tag{3.16}$$

where T_x and T_y are the horizontal and vertical IBS growth times, while T_δ is the energy spread growth time. Therefore, simply we can relate IBS growth rate as follows:

$$\frac{1}{T_{x,y,\delta}} \propto (log)A. \tag{3.17}$$

where (log) stands for *Coulomb log* factor and A as respectively as follows:

$$(log) \approx \ln\left(\frac{\gamma_{rel}^2\sigma_y\epsilon_x}{r_e\beta_{rel,x}}\right), \tag{3.18}$$

$$A = \left(\frac{r_e^2 cN}{64\pi^2\gamma_{rel}^4\epsilon_x\epsilon_y\sigma_z\sigma_\delta}\right). \tag{3.19}$$

The exact calculation of the growth times require rigorous mathematics referring to the Legendre Functions. The details can be found in [41]. Therefore, we can simply state that the IBS goes inversely proportional to the fourth power of relativistic gamma.

A particle accelerator may have various reasons causing particle loss. The vacuum or RF failures, physical or impedance mismatch between the components, misalignments, magnetic field errors, or simply any external force to the accelerator or the beam may gradually lead particle loss. The scattering of particles is not limited within the bunch itself (i.e. IBS), the particles in a bunch can also get scattered by the residual gas atoms in the vessel, as well. However, the aim in this subsection is to focus on the dynamics of the beam and interaction of the bunch within itself and the freed particles from the surrounding media. For this reason, we may categorize the particle loss as due to scattering which is mainly dominant reason in transport lines, and the instabilities which is usually seen in circular accelerators especially storage rings [18].

Particle loss occurs when the particle can no longer be kept in the dynamic aperture. Dynamic aperture is the 6D manifold in which the particles are controlled and kept alive via electric and magnetic fields, namely it is the created survival zone for the particles. Recalling Chapter 2, the trajectories of a particle is bounded by the beam envelope and RF bucket. However, due to the impact of synchrotron radiation to the beam, the energy and the angle of the particle will have jumps, and at some point, the particle will leave either momentum or transverse acceptance, eventually particle will hit the physical aperture and get lost. In consequent, the time span in an accelerator due to aforementioned mechanism is called *quantum lifetime*.

3.5. Instabilities

Beam generates EM fields with its surrounding so called the wakefield, as discussed in Section 3.2. The generated wakefield acts back to the beam, disturbing its present course. The beam may enhance the wakefield even further. For instance, when the beam dilutes due to transverse wakes, it gets bigger physically, thus it will get affected from the wakes and diluted even more. Therefore, this effect would accumulate resulting in an instability. That kind of piling up impact of interactions are examined under so-called *collective instabilities.* The instabilities indeed are the ultimate limiting factors of the accelerator requiring a thorough investigation.

Depending upon the bunch distribution and the shape of the bunch, there are certain modes of wakefields induced, as shown in Figure 3.7.

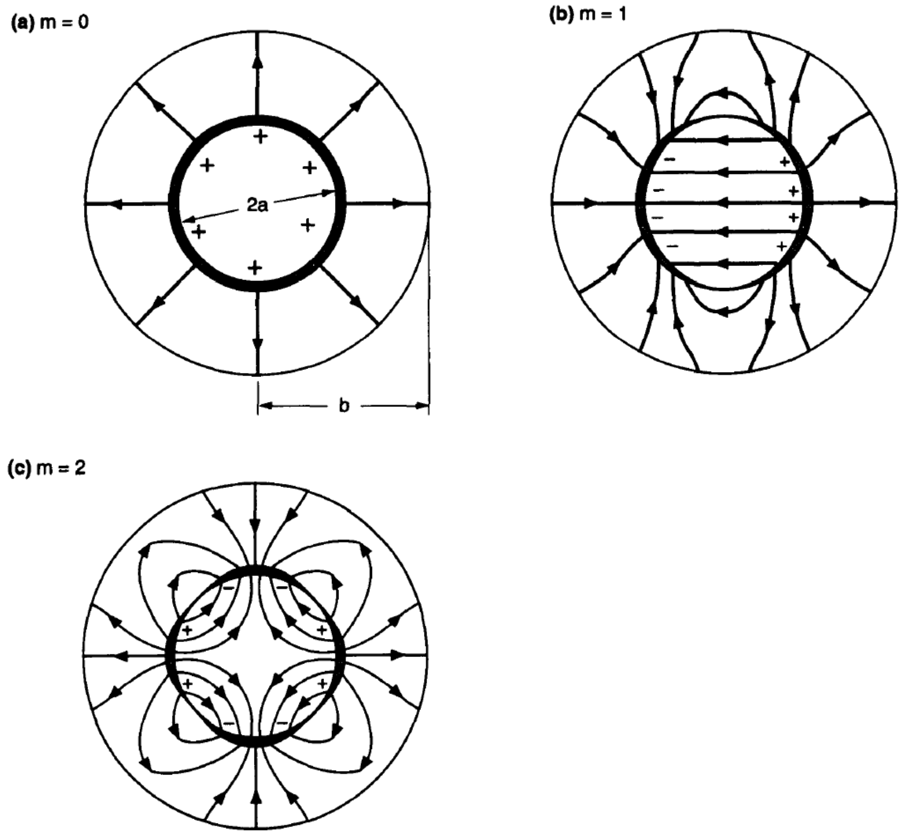

Figure 3.7. The wakefield induced by the bunch, shown as the thick inner circle. Depending upon the bunch shape a different field will be induced creating different modes of the wakefield [43].

- *m=0 mode wakefield* results in parasitic energy loss and causes energy spread through the bunch length. Particles ahead of the synchronous particle will lose energy meanwhile the tail of the bunch may gain or lose energy. This mode can be compensated by phasing the RF voltage of the linac accelerating structures.
- *m=1 mode wakefield* causes a dipole mode instability called the *dipole beam breakup* in linacs or *transverse mode coupling instability* in storage rings. Orbit steering or Balakin-Novokhatsy-Smirnov damping [42] can cure this instability.
- *m=2 mode wakefield* is the quadrupolar wakefield mode. Thus, as the name evokes, it will focus or defocus the beam leading an additional oscillation than the betatron oscillation controlled by the electromagnets. It can be generated if the beam pipe is not circular. It becomes crucial if the transverse beam size is comparable to the radius of the beam pipe.

The first two modes are quite dominant and apparent issues seen in cutting-edge accelerators, whose short-range formulas were given in Section 3.2. Also, we will discuss the compensation of these two modes in Section 5.3. The instabilities are very wide topic, for instance any undesired coupling between the planes, or even coupling of synchrotron oscillations of the beam with the fundamental resonant oscillation of the cavity will raise the so-called *Robinson instability.* Instabilities are not limited to the wakefields, nor space charge. Actually, the coupling of motion in any two or three planes would result in an instability such that the coupling of longitudinal synchrotron motion to the transverse betatron motion will result in *synchrotron sidebands of betatron coupling resonances* [44]. Further details of collective instabilities can be found in [43].

4. BASELINE FOR THE INJECTORS

A well-planned time schedule is necessary for the injector complex due to multi-use of accelerators and minimization of the time required to fill the collider from scratch. The injectors will be used both to create and accelerate both species alternatively. Hence, we need to calculate and optimize the store times of the beam in each circular accelerator so that the beam can reach equilibrium emittance of the machine leading to a preservation or cooling of beam emittance. In contrast to the collider which will go through upgrades by increasing the number of RF cavities at each stage of the four different operational modes, the injectors will stay intact in terms of hardware, however cycle differently, with their operational parameters being varied, as listed in Table 4.1.

High luminosity reduces the beam lifetime, hence it requires fast cycling injectors to fill up and top up. The FCC-e^+e^- requires 200 Hz linac repetition with 2 bunches per RF pulse particularly for the Z-operation mode, as tabulated in Table 4.1 [9]. In fact, the pulse compressors feeding the cavities can be arranged in a way to accelerate 4 bunches. This option is considered for the case of FCC-e^+e^- positron production only, in which the power pulse would carry 2 e^+ bunches to be injected into the pre-booster, and 2 high charge e^- bunches to hit the target which are directed via a magnetic separator. The newly created 2 e^+ bunches go through a flux concentrator, an adiabatic matching device, and finally a pre-injector linac surrounded firstly by a focusing solenoid and followed by quadrupole triplets. The positron linac will be embedded into the electron linac by compatible optics. The positrons accelerated up to 1.54 GeV in the last part of the linac will be transferred into the DR for emittance cooling. Then they will be transferred back to the linac at 1.54 GeV part via the bunch compressor [8].

The main idea of top-up injection is to sustain the luminosity at the peak by recovering the charge missed in the collider buckets due to collisions. The most challenging operation mode for the pre-injectors is the Z-mode since it requires the highest total current accumulated in the collider, whereas producing the heavier particles (W,

Table 4.1. Baseline parameters for the FCC-e$^+$e$^-$ injectors

operation mode	Z		W		H		$t\bar{t}$	
type of filling	Full	Top-up	Full	Top-up	Full	Top-up	Full	Top-up
energy [GeV]	45.6		80		120		182.5	
lifetime [min]	68	68	59	59	38	38	47	47
τ_{inj} [s]	122	122	44	44	31	31	32	32
linac bunches	2	2	2	2	1	1	1	1
linac repetition rate [Hz]	200	200	100	100	100	100	100	100
linac RF frequency [MHz]	2855.98							
linac bunch population [10^{10}]	2.13	1.06	1.88	0.56	1.88	0.56	1.38	0.83
SPS bunch spacing [MHz]	400							
SPS bunches/injection	2	2	2	2	1	1	1	1
SPS bunch population [10^{10}]	2.13	1.06	1.88	0.56	1.88	0.56	1.38	0.83
number of linac injections	1040	1040	1000	1000	328	328	48	48
SPS supercycle duty factor	0.84	0.84	0.56	0.56	0.36	0.36	0.14	0.14
SPS number of bunches	2080	2080	2000	2000	328	328	48	48
SPS current [mA]	307.15	153.57	130.22	39.07	51.18	15.35	4.77	2.86
SPS injection time [s]	5.9	5.9	10.7	10.7	3.98	3.98	1.18	1.18
SPS ramp time [s]	0.2							
SPS cycle length [s]	6.3	6.3	11.1	11.1	4.38	4.38	1.58	1.58
BR bunch spacing [MHz]	400	400	400	400	400	400	400	400
number of SPS injections	8	8	1	1	1	1	1	1
BR number of bunches	16640	16640	2000	2000	328	328	48	48
BR bunch population [10^{11}]	0.21	0.11	0.19	0.06	0.19	0.06	0.14	0.66
BR cycle time [s]	51.74	51.74	13.3	13.3	7.58	7.58	6.28	6.28
booster ramp time	0.32	0.32	0.75	0.75	1.25	1.25	2	2
transfer efficiency	0.8							
no. of injections/collider bucket	10	1	10	1	10	1	20	1
total number of bunches	16640	16640	2000	2000	328	328	48	48
filling time (both species) [s]	1034.8	103.48	266	26.6	151.6	15.16	251.2	12.56
required bunch population [10^{11}]	1.70	0.085	1.5	0.045	1.5	0.045	2.2	0.066

H and $t\bar{t}$) requires a higher extraction energy of the booster, but lower beam intensity from the injector. Thereby, it will be the focus of the calculations and the main effort of the pre-injectors at the Z-mode will be to foresee the charge loss in a bucket since the injector cycle is 51.7 seconds and we can inject once into the same bucket in 2×51.7 s. This time interval stems from the fact that the collider will have two beam pipes, one for each species, yet the rest of the pre-injector synchrotrons can accumulate and accelerate solely one kind at a time. On the other hand, the beam lifetime is short due to high collision rates, plus the collider will be filled by interleaving the species, while keeping the current of two species within a $\pm 5\%$ asymmetry. Therefore, a bunch schedule assisted by a simulation code has been developed to operate such a complex scheme within given constraints, including short beam lifetime, asymmetry limit for the charge of species, bootstrapping, and pre-compensation of the charge loss.

4.1. Schedule for the Damping Ring

The linac will operate at 200 Hz with two bunches per RF pulse. Therefore, there will be two electron bunches sent from the RF gun in every 5 ms. However, the positrons will be created by impinging into a target at 4.46 GeV of the linac in order to generate and capture same amount of positrons in a bunch as the electrons. It is noteworthy to recall that the FCC-e^+e^- is a symmetric collider smashing beams of equal energy and with the same bunch population in a bucket. Furthermore, the number of buckets filled into the collider are the same for both species. For this reason, in order to overcome the time delay arising due to the positron creation and acceleration, four bunches per RF pulse will be sent in which two positron bunches will be followed by two electron bunches, which will be further discussed in Section 5.8. The first two positron bunches will be accelerated to 6 GeV and injected into the PRB, meanwhile the following electron bunches will be separated via magnetic field to hit the positron target to create positron bunches, which will be accelerated in the linac up to 1.54 GeV and injected into the DR.

The first fill of the DR happens at T=40 ms of operation time, as presented in Table 4.2. The DR can host 8 trains (i.e. 8 pairs of 2 bunches), which can be supplied by sending a pair of electron bunches per RF pulse from the thermionic gun to generate a pair of positron bunches to be injected into the DR. After the first fill of the DR, linac will switch to 4 bunch-acceleration mode in one RF pulse where a pair of positrons will be followed by a pair electrons with 50-nanosecond spacing. Actually, the designed DR in Chapter 7 is 241.8 meters long corresponding to about 807 nanoseconds for $\beta_{rel} \approx 1$. This circumference is chosen to space the 16 bunches stored equidistantly by approximately 50 ns. Indeed, this 50 ns spacing complies with the bunch-to-bunch spacing limited by longitudinal wakefield in Section 3.2 as well as with the beam loading compensation which will be discussed in Section 5.8. Naturally, this orientation requires a kicker magnet with a rise and fall time with less than 50 nanoseconds for the safe injection and extraction of a train.

The steady state condition of the DR to host 16 bunches, as depicted in Figure 7.1. In the DR, a pair of bunches stayed 40 ms is extracted. Those e^+ bunches will then meet at 1.54 GeV of the linac with the RF pulse which has already carrying 2 bunches of electrons. The RF pulse in total will have 2 e^+ and 2 e^- bunches between 1.54-4.46 GeV energy sector of the linac. The 2 e^- bunches will hit the converter, whereas the 2 e^+ bunches will follow the orbit bump and accelerated to 6 GeV and injected into the PRB. Therefore, the steadiness of the DR charge has a perturbation in charge during injection/extraction for the time period of the new bunches arriving from the same RF pulse. The positron flow continues in this manner until one tenth of the positron buckets in the collider are full in order to ensure interleaving injection of two species. However, the electron beam injection mode requires steadily 2 bunches per RF pulse in all parts of the linac from the RF gun, and similar table as Table 4.2 can be developed to allow 40 ms of store time in the DR for the electrons, as well.

4.2. Schedule for the Pre-injector Synchrotrons

The injection from linac into the PRB will happen fastest during the first fill of the collider for the Z-pole operation. The PRB will accumulate 2080 bunches in this operation mode, namely 1040 injections from the linac which will correspond to 5.2 seconds of linac injection then the linac will stop. The PRB will stay at 6 GeV, in other words, at flat bottom energy till the injection of 2080 bunches are complete. Afterwards, the PRB will damp the injected beam by turning the wigglers on for 7 damping times that corresponds to 0.7 seconds since the PRB damping time is optimized to be 0.1 s at flat-bottom energy. The emittance cooling of electron bunches is mandatory since some bunches would have already circulated in the PRB for 5.2 seconds while the last injected ones are still oscillating inside the RF bucket due to off-axis injection type, a behaviour will be explained in the next paragraph. After bunch accumulation of 5.2 s plus emittance cooling for 0.7 s, the PRB will ramp-up in 0.2 second to accelerate the beam from 6 GeV to 20 GeV by assuming an acceleration of 70 GeV/s which includes

Table 4.2. The time schedule of the positrons in FCC-e^+e^- pre-injectors. The positron bunches extracted from the DR are those that have been injected 40 ms earlier.

RF time [ms]	number of bunches		
	linac	damping ring	pre-booster
0-5	2 e^-	2 e^+	empty
5-10	2 e^-	4 e^+	empty
10-15	2 e^-	6 e^+	empty
15-20	2 e^-	8 e^+	empty
20-25	2 e^-	10 e^+	empty
25-30	2 e^-	12 e^+	empty
30-35	2 e^-	14 e^+	empty
35-40	2 e^-	16 e^+	empty
40-45	2 e^- & 2 e^+	16 e^+	2 e^+
45-50	2 e^- & 2 e^+	16 e^+	4 e^+
50-55	2 e^- & 2 e^+	16 e^+	6 e^+

energy loss of electrons due to synchrotron radiation, thus it is compatible with the current RF system of the SPS filling LHC with 100 GeV/s energy gain [10]. Therefore, the beam will be extracted from the PRB into the BR, however PRB needs to ramp down the magnets in 0.2 s, i.e. the same as it ramps up. In total, the PRB cycle is $5.2 + 0.1 \times 7 + 0.2 \times 2 = 6.3$ s for the Z operational mode. The similar accumulation will take place in the booster ring (BR) until its 16640 buckets with the same charge as the PRB are filled. The accumulation in the BR will be supplied through 8 injections, 7 damping times for emittance cooling with the BR damping time of 0.1 s plus ramp up and down times of 0.32 s resulting in requiring $6.3 \times 8 + 0.1 \times 7 + 0.32 \times 2 = 51.74$ s. All these parameters tabulated in Table 4.1.

The injection type into a synchrotron is also crucial in determination of the kicker rise time, and more importantly the required dynamic acceptance of the ring. For instance, the bunches in the linac has a separation of 50 ns, therefore the single turn injection with the kicker can be applied to accept that bunch into the DR if the kicker rise/fall time is shorter than 50 ns. The kicker puts the beam coming with an angle with respect to the ring trajectory *on-axis* matching the beam location and angle to the ring trajectory (see Section 2.8 for beam injection elements and matching). On the other hand, the PRB bunch spacing is determined to be 2.5 ns, thus it is extremely challenging to deploy a kicker with rise time below 2.5 ns at 6 and 20 GeVs for injection and extraction, respectively. Therefore, the injection needs to be done without kicker by injecting from the transfer line into the PRB via a septum magnet without a kicker steering beam onto the reference line of the synchrotron. Therefore, the beam injected *off-axis* will oscillate around the bucket center. Naturally, the beam is supposed to be smaller than the 6-Dimensional acceptance of the ring, since it will oscillate and may filament in the RF bucket. For this reason, the dynamic acceptance of the ring has to be large enough allowing these oscillations without loss. Fortunately, this oscillation will be damped thanks to the synchrotron radiation, and the injected bunch will become on-axis eventually. The injection types into the FCC-e^+e^- rings are listed in Table 4.3 [11].

Table 4.3. Injection types into the circular accelerators.

accelerator	injection type
damping ring	on axis
pre-booster	off-axis
top-up booster	on-axis
collider	off-axis

4.3. Bootstrapping and Top-up Injection

The PRB and BR will have one beam pipe, therefore they will either accelerate electrons or positrons by keeping the same polarity alternatively, yet having the beam circulating oppositely. Therefore, in order to start collisions and top-up the charge loss due to the collisions at the earliest, it is necessary to have the ability to inject into all buckets of the collider specific charge needed as soon as possible. This is why the number of buckets filled into the BR is the same as the collider. Normally, by foreseeing the state of a collider bucket, the pre-injectors can prepare exactly needed charge and satisfy the need. This is actually pre-compensation of the loss because the injectors can inject into a collider bucket earlieststst in 51.74 seconds×2 (recall that the injectors are alternatively used for the two species), therefore it is wiser to prepare a charge which is lost already and will be lost additionally in 51.74×2 s. Therefore, the sufficiency and efficiency of this mechanism are needed to be optimized, especially for the Z-mode demanding the highest charge from the injectors. This is why, the following preliminary results are meant for the Z-mode.

Each ring of the collider will contain 16640 RF buckets at Z-pole filled with 1.7×10^{11} (i.e. full charge) particles, one ring reserved for e^-, and another for e^+. The BR will carry only a fraction of the full charge, but will also have 16640 RF buckets filled. The main issue arises when the collider buckets get almost full. If we keep injecting regularly, for example, 10% of the full charge, the asymmetry between the charges may cause the species with the comparatively lower charge to decay faster, and in the end result in a forfeited collider bucket. The beam lifetime of Z-mode operation has been determined to have an asymmetry budget of ±5%. However, this limit is approached when the bunch charge gets close to full, but is not yet important for the first fill of the collider when injecting from zero. In Table 4.1, one can see that the injectors are in general optimized to accumulate the collider charge in 10 injections. However, these 10 injections may not necessarily be with the same charge each. For example, the low emittance RF gun of the FCC-e^+e^- can provide 4×10^{10} electrons in a bunch [12], so that we can start by injecting that charge into the collider, and lower the injection amount later in time. Figure 4.1 shows an example of such a case starting with a high charge and continuing with lower charge.

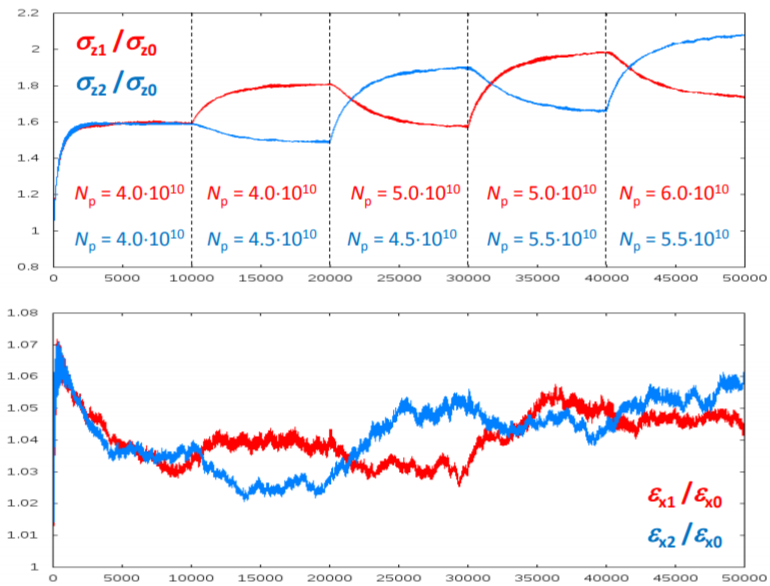

Figure 4.1. An illustration of bootstrapping, showing the relative bunch length in mm and emittance fluctuations in nm, respectively, while additional bunches are injected throughout the turns, where blue and red colors refer to e$^-$ and e$^+$ respectively [45].

Particles will always collide after the first injection of both species. The amount of surviving particles in collisions can be described as an exponential decay:

$$N = N_0 e^{-t/\tau}, \tag{4.1}$$

where N is the final amount of particles left after a time t, when initially N_0 particles were present with beam lifetime τ. The beam lifetime τ is 70 minutes for Z-operation mode, but τ gets increased when only some fractions of the full charges are available in the collider. In Figure 4.2, the interleaved first fill of the collider is presented. Here, the calculated charge losses in two booster cycles are already added to the preceding bunch while respecting the charge asymmetry limit between the species. The collider bucket is filled in 10 Booster cycles. Since we started with e$^-$, we include additional e$^+$ that would be lost within one Booster cycle. For this reason, e$^+$ surpasses the full charge line (shown in green) in Figure 4.2.

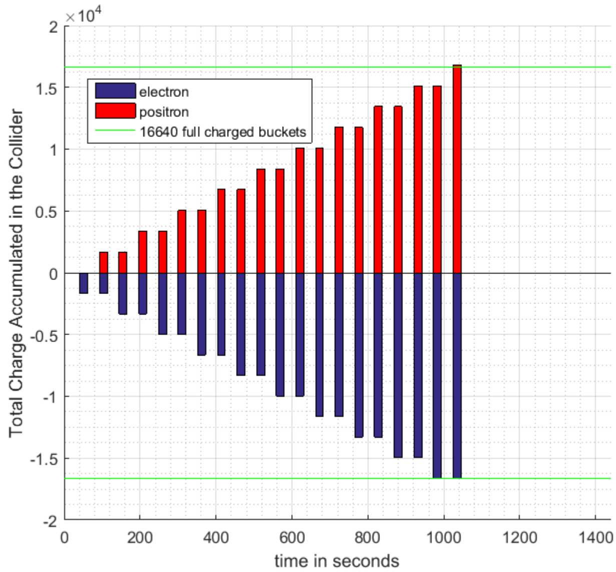

Figure 4.2. The first fill of the collider is complete after 1035 seconds. The vertical axis shows the total charge accumulated in the 16640 buckets where the full charge is normalized to unity.

As a safety margin, we may send twice intensity of e^- at 4.46 GeV to impinge on the target to yield the required amount of e^+ at the end of linac. Furthermore, the charge available in the SPS should stay within the capabilities of the SPS RF system. Therefore, the charge flux accelerated in the pre-injectors should respect all limitations of the downstream accelerators. To illustrate, if a bunch population of $4{\times}10^{10}$ is intended in the pre-injectors, $8{\times}10^{10}$ e^- can be required to get $4{\times}10^{10}$ e^+. On the other hand, even if the linac can accelerate such a high charge, the current stored in the SPS would become more than 600 mA which may not be sustainable with the existing SPS RF system. All in all, 10 injections with pre-compensation of the charge result in around $2.1{\times}10^{10}$ particles in a bucket and just above 300 mA in the SPS, which seems to be adequate and sustainable.

On the other hand, the top-up injection will be maintained by injecting 2.4% of the full charge starting with e^- and continuing with alternative charge and so on. Therefore, the charge asymmetry always stays within $\pm 1.2\%$. Figure 4.3 shows the top-up injection for the Z-mode, the injection repetition is one booster cycle (i.e. 51.74

s), yet alternating between the species. One can see that the time average of both species is the full charge (i.e. shown as 1), which corresponds to full bunch by bunch luminosity excluding the effect of other parameters on luminosity.

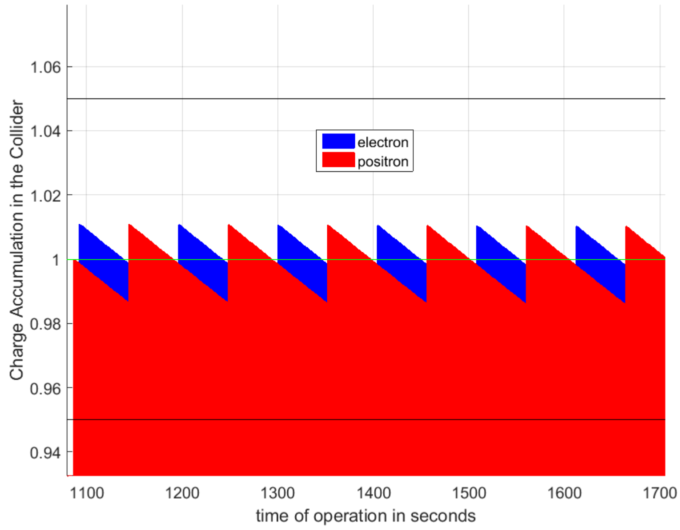

Figure 4.3. Top-up injection can be arranged to keep the charge imbalance to less than ±5% (shown as horizontal black lines). Also, the time average of both charges is kept around the full charge (shown as 1 in vertical axis).

5. LINAC

Linear accelerators are the most common injectors for colliders since they cycle with high repetitions providing low emittance high charge beam and allowing high gradient acceleration. The normal conducting S-Band cavities are chosen for the FCC-e^+e^- injector linac with a frequency 2855.98 MHz as it is exploited at KEK and SLAC. The normal conducting linac will be fed by two different electron sources, one will be the RF gun for the low emittance e^- beam, and the second is the thermionic gun for providing higher charge for creating more positrons by impinging on a target. The thermionic gun is a conventional electron source which can be similar to KEK's gun [46] and for this reason, it is omitted, instead the novel RF gun designed for the FCC-e^+e^- linac will be briefly discussed.

5.1. RF Gun

The RF gun is custom designed to have low emittance beam by suppressing the emittance blow due to space charge by deploying permanent magnets in the irises. Not only the magnetic field adjustment, but also the electric field needed for acceleration is a distinguished technique which is to couple the parallel cavities [12], [47], as depicted in Figure 5.1. The idea underlies behind the parallel coupling is to feed each cell directly from the source so that the cavities (i.e. the cells) do not affect each other meanwhile the voltage kept high and beam loading is compensated. Another subtle parameter of the RF gun is the photocathode, since the beam is very intense, the photocathode needs to be robust and reliable. For this reason, material based on IrCe alloy [48]-[49] will be used in the photocathode. Such material provides acceptable life time with high charge extraction up to 6.5 nC and a high pulse repetition of 200 Hz with 2 bunches per pulse. The prototype of the RF gun has been produced at Budker Institute of Nuclear Physics (BINP) in Russia [50] and some parameters of the gun are presented in Table 5.1.

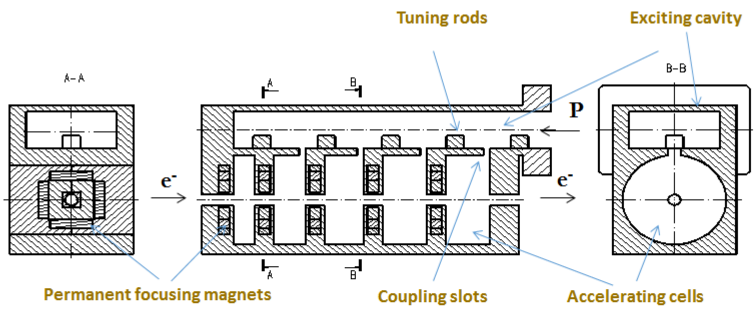

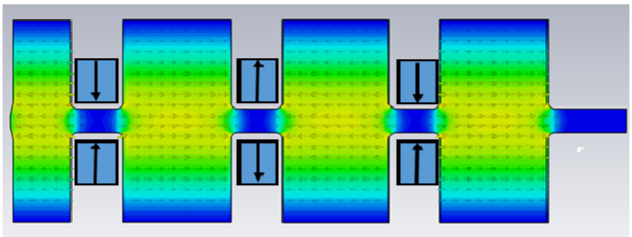

Figure 5.1. Sketch of S-Band RF gun using parallel coupling accelerating structures with permanent magnets in the irises, and its corresponding electromagnetic simulations are shown beneath.

Table 5.1. RF Gun parameters

Parameter	Value
total charge	6.5 nC
laser pulse duration	8 ps
peak accelerating field	100 MV/m
focusing solenoid field	0.5 T
beam length (σ_z)	1.5 mm
normalized transverse emittance	3 π.mm.mrad
energy	9.8 MeV
energy spread	0.6 %

In conclusion, the initial parameters of the linac simulations starts with the RF gun parameters. Actually, the linac assumes less stringent parameters that can be achieved from the RF gun, therefore more challenging scenario to mitigate for the linac, yet a safety margin to the RF gun.

5.2. Misalignments and Impact of the Wakefields

The transverse and longitudinal wakefields calculated in Section 3.2 have been included in linac simulations. Indeed, the transverse wakefields do not affect the beam unless the beam enters the cavities off-axis. For this reason, the misalignments and offsets tabulated in Table 5.2 are also taken into account in the simulations.

Table 5.2. Misalignments and offsets applied to the linac elements. The rms errors are applied independently in horizontal and vertical directions. Gaussian random distribution is applied with no truncation.

Parameter	Simulated Error
spatial injection offsets (h/v)	0.1 mm
angular injection offset (h/v)	0.1 mrad
quadrupole misalignment (h/v)	0.1 mm
cavity misalignment (h/v)	0.1 mm
BPM's misalig. w.r.t. cavity (h/v)	30 μm

The BPM errors tabulated are with respect to the cavity center, where one BPM is attached to the cavity entrance and another one to the exit, as depicted in Figure 5.2. The impact of transverse wakefields brings additional driven force to the Hill's equation in Equation 2.40. Due to the causality, this force created by the tail of the relativistic bunch can *drive* the tail of the bunch resonantly and this oscillation might get enhanced while propagating along the accelerator. 2-particle model explains the phenomena thoroughly in which the head and tail correspond to one macro-particle each, and the beam centroid, in a sense, is the rod linking these two macros, as depicted in Figure 5.3.

The transverse wakefields in the presence of misalignments cause the emittance blow-up, and eventually beam loss. On the other hand, longitudinal wakefiels cause the tail of the bunch gain less energy, as discussed in Section 3.5. Together with the transverse wakefields, the tail of the bunch gets elongated while oscillating. Therefore,

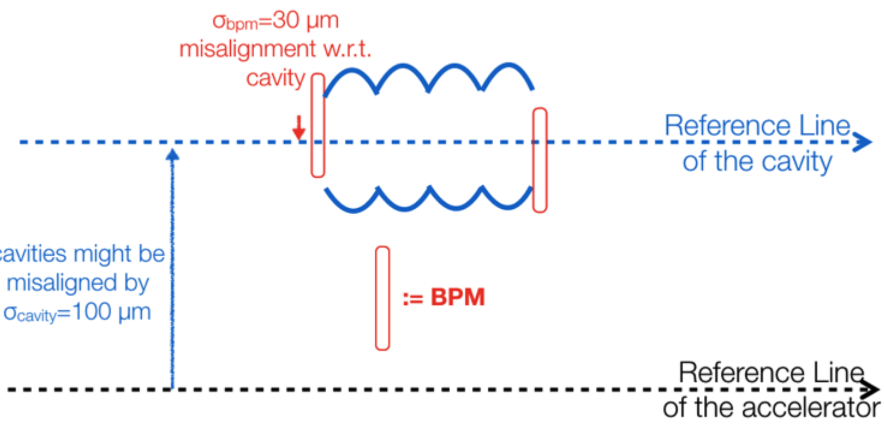

Figure 5.2. Accelerator elements can be aligned with respect to (w.r.t.) a reference line which is usually determined by a laser alignment technique. Moreover, the accelerating structure has two BPMs: one attached to its entrance and another to its end which can be also misaligned independently w.r.t. the cavity.

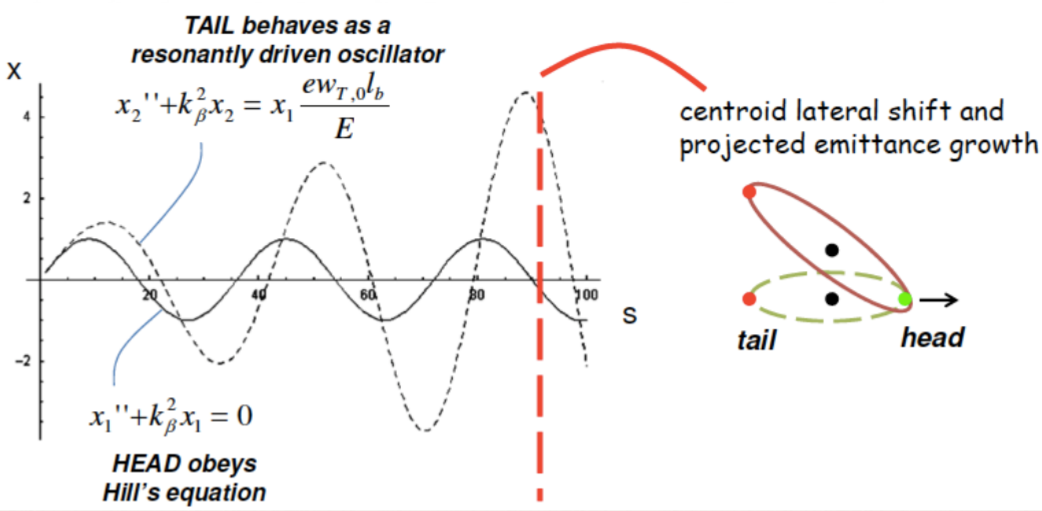

Figure 5.3. Head of the bunch can resonantly drive the tail due to the transverse wakefields. This oscillation may result in single-bunch beam break-up and beam tail loss. Courtesy: Alexander Wu Chao.

an efficient orbit steering or mitigation of wakefields' impact is crucial and will be discussed in Section 5.4.

5.3. Accelerating Structures

The accelerating structures consist of cells or disks (i.e. we call both cavities) and the voltage occurs between the gap of the irises (i.e. the aperture), therefore the energy gain of the charge q depends on the number of gaps N_{gap} and RF voltage V_{RF} as follows

$$\Delta E = qN_{gap}V_{RF}. \tag{5.1}$$

Also, considering the fact that the voltage is inversely proportional to the distance, it can be concluded that the smaller iris aperture results in higher gradients. The linac consists of S-band structures up to 6 GeV, whereas the C-band high gradient accelerating structures are utilised between 6-20 GeV. The C-band extension in the linac is for the direct injection option into the top-up booster. The C-band frequency is exactly 2 times of the S-band in order to ease the pulse synchronization. The higher frequency corresponds to the smaller wavelength, therefore more frequently deployed irises, and thus more gaps for acceleration. To illustrate, S-band accelerating structures have 3 cells in 10.5 cm length, whereas C-band structures have 6 cells at the same reference length where both structures oscillate with $2\pi/3$ mode. Number of disks/cells per wavelength is called the *cavity mode*, for instance $2\pi/3$ mode means there are 3 disks in one wavelength, similarly π-mode means 2 disks per wavelength and so on. The utilised cavities for the linac has been presented in Table 5.3.

Table 5.3. Linac travelling wave accelerating structures.

Cavity	S-Band	C-Band
frequency (MHz)	2855.98	5711.96
length (m)	2.97	1.80
cavity mode	$2\pi/3$	$2\pi/3$
aperture diameter (mm)	20	14
unloaded cavity gradient (MV/m)	25	50

The accelerating structures can be categorised as superconducting or normal conducting depending on the operation temperature and materials of the composition. The superconducting (SC) cavities can hypothetically transfer all the input RF power into to the passaging beam, hence they are useful when used in circular accelerators, since the beam is passing too often inside the cavity, as a result all the FCC-e^+e^- synchrotrons as well as the damping ring utilize SC cavities. Therefore, the operational cost of the superconductivity will be negligible in that case. On the other side, the normal conducting (NC) cavities are useful since they are easy to operate and they can provide high gradients, as a result they are deployed in the FCC-e^+e^- linacs. The accelerating structures can also be defined in terms of power fed as travelling wave or standing wave structures. In the FCC-e^+e^- pre-injectors, SC cavities with standing waves are used in the circular accelerators including the damping ring while the NC cavities with travelling wave structures used for the linacs. The S-Band cavities will be used in the FCC-e^+e^- linac is going to be similar to the structure of KEK, as presented in Figure 5.4.

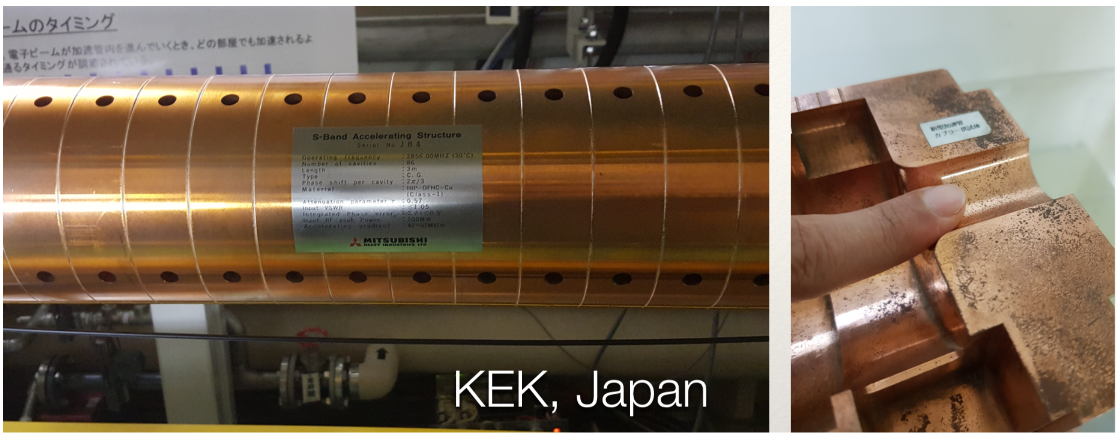

Figure 5.4. The FCC-e^+e^- linacs will utilise the similar cavities used at KEK. 3-m long S-Band structure has been shown on left, and the aperture of the cavity is pointed by a finger on the right.

The disc loaded structure as shown in Figure 5.4 consists of pillbox cavities resonating with the TM_{010} mode which was explained in Subsection 2.5.1.

5.4. Orbit Correction and RF Cavity Phasing

The transverse wakefield driven oscillation, also known as the head-tail instability, is needed to be suppressed, otherwise it will dilute the emittance and gradually result in beam loss, as discussed in Section 3.5. In order to damp the oscillation amplitude, Balakin-Novokhatsky-Smirnov (BNS) damping [42], [51] or off-axis injection can be applied. The intentional off-axis injection of the beam into the linac is to experience random deflections on the tail so that the kicks cross-cancel each other. In short, this method utilizes the wakefield itself to cancel its impact. On the other hand, BNS damping makes use of chromatic effect such that the energy of the bunch tail is needed to be adjusted so that quadrupoles can *re-align* the tail towards the centroid considering the fact that the field of the quad is stronger to the particles away from the center. However, we choose another option, instead of chromatic correction or cross-cancellation of deflection, we choose the steering the beam to the cavity centers and avoid emittance dilution before it occurs. First, the wakefields dilute the emittance of the beam most in the cavities because of the continuities, also because the cavity aperture is smaller than the beam pipe. Second, the beam is deflected dramatically when they pass off-axis of the strong quadrupole. To sum up, the beam should traverse through the cavity center. In order to cancel out the impact of the misaligned quadrupoles, we deployed two steerers in a row which both can steer in $x - y$ axes. Indeed, one steerer can direct the beam to the reference line of the cavity, however by deploying two steerers we can also cancel out the angular divergence of the beam together with aligning spatially. The depiction of the steering algorithm which uses *two steerers and two BPMs* is demonstrated in Figure 5.5.

The beam orbit correction scheme is indeed a beam transport matrix problem in which the response matrix R_{ij} is needed. Simply, we have two BPMs which are attached to the cavity entrance and exit. First, we will assume these two BPMs are ideally aligned to the cavity reference line. To start with, 2D transport matrix from

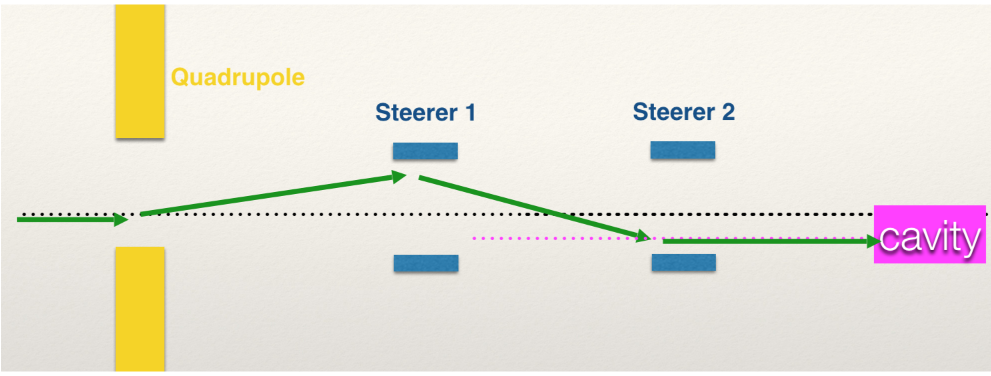

Figure 5.5. Automatic orbit correction code is written in which two steerers direct the beam simultaneously in x and y axes to the cavity center. By deploying two steerers, both spatial and angular divergence of the beam are cancelled, as a result beam enters the cavity on axis and is not affected from the wakefields.

location 1 to location 2 is:

$$R = \begin{pmatrix} R_{11} & R_{12} \\ R_{21} & R_{22} \end{pmatrix}, \tag{5.2}$$

where the transport matrix elements [52] are

$$R_{11} = \sqrt{\frac{\beta_2}{\beta_1}}(\cos\Delta\varphi + \alpha_1 \sin\Delta\varphi) \tag{5.3}$$

$$R_{12} = \sqrt{\beta_1\beta_2}\sin\Delta\varphi, \tag{5.4}$$

$$R_{21} = -\frac{\alpha_1 - \alpha_2}{\sqrt{\beta_1\beta_2}}\sin\Delta\varphi + \frac{1 + \alpha_1\alpha_2}{\sqrt{\beta_1\beta_2}}\cos\Delta\varphi, \tag{5.5}$$

$$R_{22} = \sqrt{\frac{\beta_1}{\beta_2}}(\cos\Delta\varphi - \alpha_2 sin\Delta\varphi), \tag{5.6}$$

where $\Delta\varphi$ is the phase advance in between and Twiss parameters at the specific location is denoted with the corresponding location. The none negligible element is R_{12} since it is the deflection to the beam needs to be calculated between the steerers and the BPMs of the cavity and then corrected. For this reason, the acceleration inside the cavity should be also taken into consideration. Therefore, R_{12} including acceleration becomes:

$$R_{12}^{rel} = \frac{(\gamma_{rel}\beta_{rel})_2}{(\gamma_{rel}\beta_{rel})_1}\sqrt{\beta_2\beta_1}\sin\Delta\varphi. \tag{5.7}$$

Apart from the angular divergence, we need to also correct the orbit spatially. The orbit (i.e. beam centroid or the synchronous particle) location is read from the BPMs, Therefore, the beam orbit at location dx needs to spatially directed to the cavity located at dxc, so the beam needs to be re-directed by an amount of $x = (dx - dxc)$. Simply, we have to linear solve following:

$$M = [R_{12}^{rel}, x]. \tag{5.8}$$

The solution of matrix M is indeed the angle needed to steer the beam therefore corrector is set to that strength, on the orbit correction in horizontal axis is provided. Similarly, the skew component of the steerer (i.e. vertical steerer referring to the Figure 2.3) will go through similar calculation of R_{12} for y-axis, also the cavity offsets in vertical directions need to be used. However, the calculated angle for the vertical axis needed to be set with a minus sign since the skew component definition in the code *SAD*. The impact of misalignments is almost perfectly cancelled for the case of ideally deployed BPMs. Even though we deploy two BPMs to each cavity, they can be aligned up to a point that is 30 μm of rms precision, as presented in Figure 5.2 and Table 5.2. Last but not least, the linear solution of the matrix M can be done up to a tolerance value which can be also used as a free parameter to further optimize the orbit steering algorithm. Physically, it means that the beam is not exactly steered to the cavity reference line, but a little bit up or down so that we can also utilise the cross-cancellation of the transverse wakefields.

In conclusion, some simulations with different charge and randomization have been performed to study reliability of the linac with orbit steering. Small emittance blows have arisen yet this can be further mitigated in a real machine by performing a beam-based alignment for the quads, such as Ref. [53] or the novel method presented in Section 8.1.

5.5. Linac Up to 1.54 GeV

The low energy part of the linac starts with the beam from the RF gun whose specifications are given in Table 5.1. However, the rms bunch length of 1.5 mm from the RF gun needs to be shortened to the rms 1 mm, this can be easily achieved thanks to a chi-cane bunch compressor. The bunch compressor will squeeze the bunch length in exchange of energy spread since the longitudinal normalized emittance is conserved. Basically, the 1.5 mm bunch length times 0.6% energy spread is transformed to 1 mm bunch length with 1% energy spread leaving some additional safety margin for the blow-up during the compression. The injection parameters into the first sector of the linac is given in Table 5.4. It is note-worthy to highlight the fact that this low-energy part of the linac will be only used by the electron beam. The positron acceleration up to 1.54 GeV, will be supplied after they are created at 4.46 GeV (energy of the electrons) and onwards.

Regarding the fact that space charge and wakefields are more disruptive at low energies, we need strong focusing there so that we keep the beam focused entering the cavities with small size. It is not contradictory to keep the beam small since the space charge will loosen just after the first cavity for reasons that will be explained in the next paragraph. By performing strong focusing at low energy sector, the beam stays spatially small during acceleration, and thus as acceleration continues, the beam emittance experiences adiabatic damping. Therefore, it gets more rigid and less vulnerable to the wakefields as the acceleration continues and beam stays small. This is why the first sector of the linac contains singlets, doublets and triplets. Unlike the FODO lattice singlets which consists of single quadrupole spaced by more than its focal length to the next quad, doublets and triplets respectively refer to two or three quadrupoles

Table 5.4. Injected beam parameters into the linac up to 1.54 GeV sector.

Parameter	Value
length	79.1 m
number of cavities and quadrupoles	21 and 14
RF pulse repetition and bunches per RF pulse	200 Hz and 2
injected emittance (x/y)	0.35/0.5 μm
rms bunch length at injection	1 mm
rms energy spread at injection	1%
final emittance w/o blow up (x/y)	2.7/3.8 nm
average extracted emit. (h/v)	6.4/5.0 nm
transmission for 3.5 nC	100%

which are located with respect to each other less than their focal lengths resulting in a strong focusing simultaneously in both transverse directions. Needless to say that, the quadrupoles are with alternating orders in all cases. For instance, the LHC squeezes the particles at the detectors for collisions thanks to a triplet of quadrupoles for each beam [54]. Basically, the triplets make the beam size smaller, in other words, makes the β function smaller, this transverse beam size minimization is called *low-β insertion*. All in all, the first portion of the linac is presented in Figure 5.6.

Here the accelerating structures come with the two steerers in front referring to Section 5.4, and except quadrupole locations, the linac has a unit cell as shown in Figure 5.7. Actually, 21 accelerating structures stated in Table 5.4 refer to 21 low energy linac unit cells shown below.

Following the single particles dynamic design, the multi-particle tracking simulation is due. The space charge is included in the RF gun and in the first cavity of the linac simulations, in other words, the impact of the linac is studied up to 85 MeV which corresponds to $\gamma_{rel} \approx 167$ and omitted for the rest of the linac since the impact of the space charge fades away by $1/\gamma_{rel}^2$ referring to Equation 3.9. For this reason, the realistic misalignment scenarios and free randomization of all errors together with

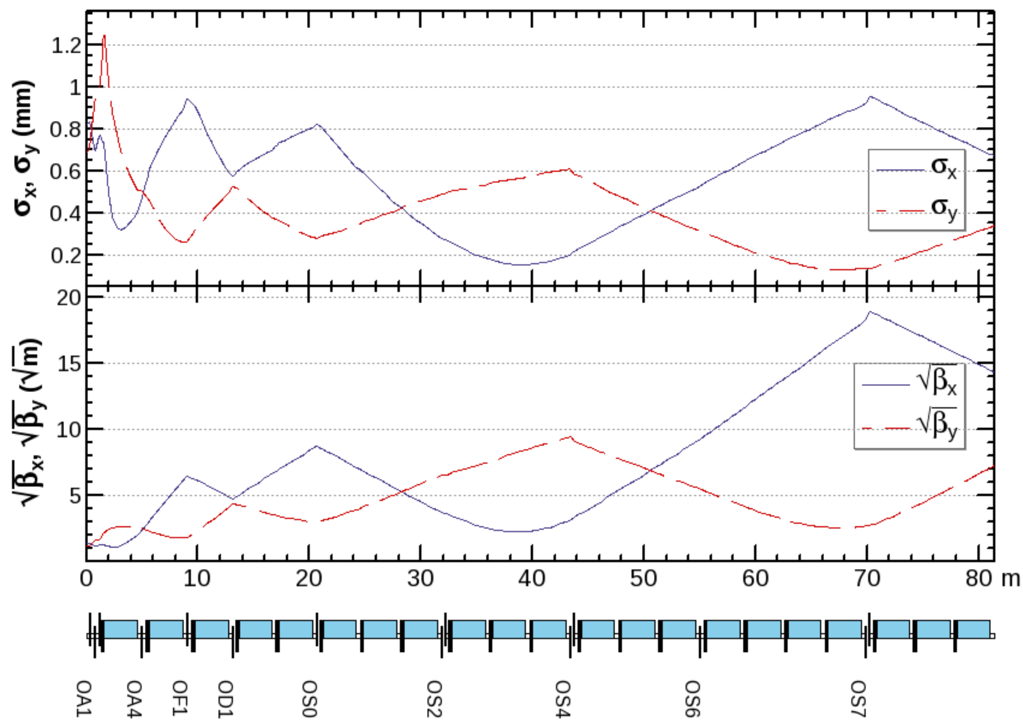

Figure 5.6. Beam optics of the linac accelerating electrons up to 1.54 GeV. The upper plot shows the 1-σ beam size in horizontal and vertical axes, while the corresponding β-functions are shown below. The vertically aligned strings located under x-axis are the quadrupole names, and the small blue boxes indicate the S-band cavities.

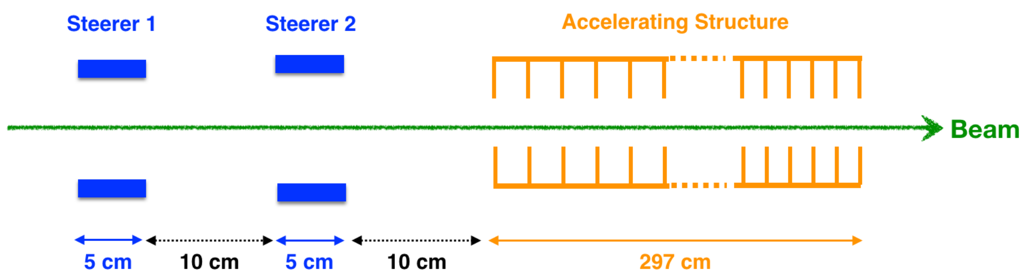

Figure 5.7. The unit cell used in the low energy part of the linac. The linac has 21 of these (not to scale).

the automatic orbit steering have been performed for different random seeds. Hundred thousand Gaussian random macro-particles are used when the space charge is on, while one million macro-particles are used for tracking simulations performed on SAD in order to check the efficiency of the orbit steering in the presence of errors[5] . The horizontal/vertical (h/v) emittance would have been 2.7/3.8 nm in the absence of the misalignments and errors. To sum up, including all major internal and external interactions within the linac simulations, the linac can achieve the results presented in Table 5.5.

Table 5.5. Tracking results in the linac up to 1.54 GeV.

Parameter	Result
final emittance without blow up (h/v)	2.7/3.8 nm
average extracted emittance (h/v)	5.5/6.0 nm
average longitudinal emittance	1.9 μm
transmission for 3.5 nC	100%
the final bunch length	1 mm
the final energy spread	0.2%

There is an emittance blow of approximately factor 2, which is high, however it can be easily cooled in the DR, therefore the most important parameter for the initial part of the linac is to transmit the beam into the DR without any loss while staying below 1 μm transverse emittance for the DR acceptance, which is achieved in our design. The beam profile at the end of 1.54 GeV is presented in Figure 5.8. The RF phase in all cavities are chosen to be $-94°$, therefore the 1% less than the nominal acceleration is achieved which can be seen in bottom right plot of the Figure 5.8. Actually, this is expected due to non-crest acceleration (i.e. $-90°$) and the longitudinal wakefield (see Section 3.2). This is why the cavity phase has been adjusted to $-94°$, so that the energy spread had two horns in a sense the energy spread inside the bunch kept narrow. Basically, the 1% shortcoming in the final energy can be compensated by increasing the cavity voltage or by simply adding one more accelerating structure at the end if it exceeds the cavity voltage limit.

[5]Typical number of particles per bunch is at the order of 10^{10}-10^{11}, however the simulation codes can manipulate 10^6 particles at most, this is why they are called macro-particles.

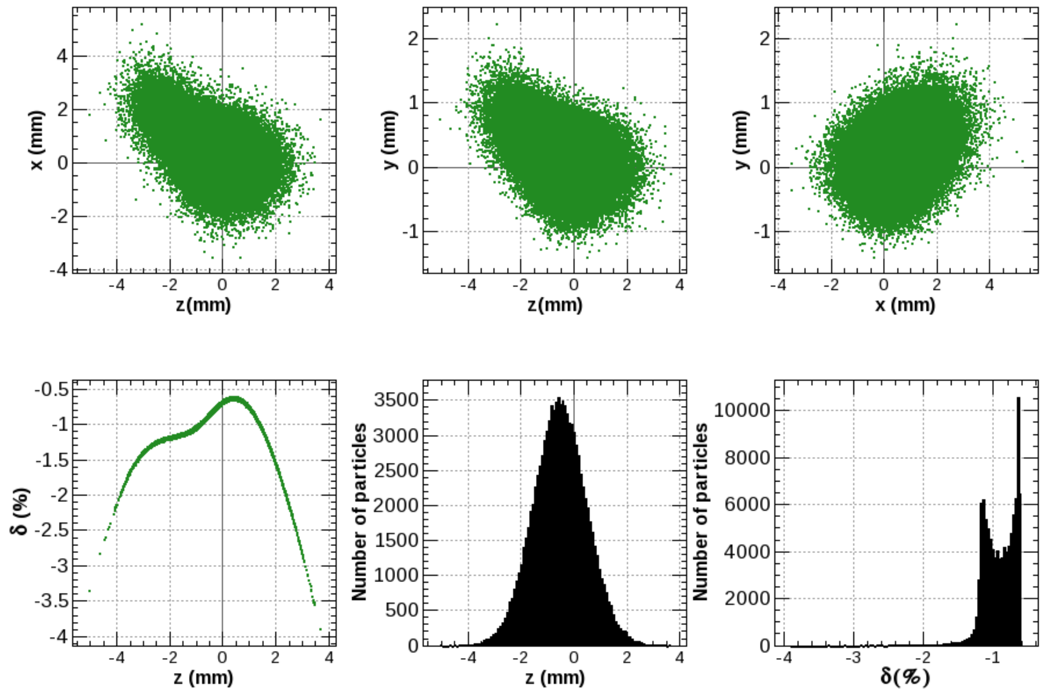

Figure 5.8. Beam profile at the end of 1.54 GeV linac by tracking of 10^5 macro-particles. The first row shows the beam in the spatial axes, and the second row figures are energy spread along the bunch length; particle distributions along the bunch length, and lastly the distribution of the energy spread, respectively.

5.6. Linac 1.54-6 GeV

The linac at 1.54 GeV has a branching point for e^- beam cooling in the DR during e^- beam delivery to the collider. On the other hand, the electrons will be directly accelerated to 4.46 GeV to hit the target during positron production, thus no emittance cooling for the primary e^- beam is allocated, but emittance cooling is mandatory for the secondary e^+ beam generated. Actually, the usage of DR for e^- is a little bit precaution rather than necessity in case of probable emittance dilution due to misalignments and space charge, also to keep the compatibility of the two species. Electrons will be stored for 40 ms (see Section 4.1) in the DR that can eliminate the emittance blow up even if it is about 1000 times then the nominal geometric emittance. Therefore, again the main concern is the positrons. For this reason, we take the positron beam and inject them into DR, after emittance cooling they are extracted to be transferred back to the linac via the turnaround loops and bunch compressor [8]. Therefore, the beam is tracked in the DR, bunch compressor then some beam transfer lines to match the beam to the injected accelerator, the injected and extracted parameters of the 1.54-6 GeV linac are given in Table 5.6.

Table 5.6. Some parameters of the 1.54-6 GeV linac.

Parameter	Value
length of the accelerator	248.5 m
number of cavities and quadrupoles	60 and 12
injection-extraction energy	1.54 GeV-6 GeV
RF pulse repetition and bunches per RF pulse	200 Hz and 2 (4*)
injected emittance (h/v)	1.9/0.4 nm
final emittance w/o blow up (h/v)	0.48/0.10 nm
average extracted emit. (h/v)	0.55/0.11 nm
average extracted emit. (long.)	1.1 μm
final rms bunch length	0.4 mm
final rms energy spread	0.5%
transmission for 3.5 nC	100%

*During positron beam delivery.

Like in the case of low energy linac, the middle energy linac also has a unit cell depicted in Figure 5.9.

In 6 GeV linac option, the beam will be injected into a newly designed pre-booster damping ring or SPS which would be slightly modified for the FCC-e^+e^- [6]. The emittance and transmission are well preserved in the linac, actually the horizontal blow is about 15% on the average for different seeds. The acceptance of the SPS is 10/100 nm (h/v), which leaves a very large safety margin to the linac for the extracted emittance. The beam optics of 6 GeV linac is given in Figure 5.10 and tracked beam with 20 macro-particles representing 3.5 nC bunch charge is presented in Figure 5.11.

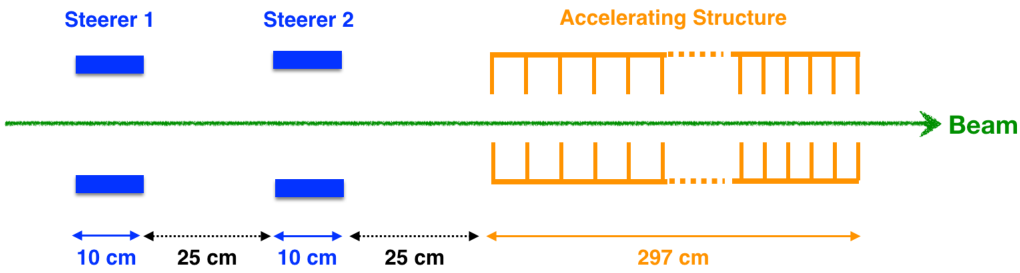

Figure 5.9. The unit cell used in the middle energy part of the linac. The linac (1.54-6 GeV sector) has 60 of these (not to scale).

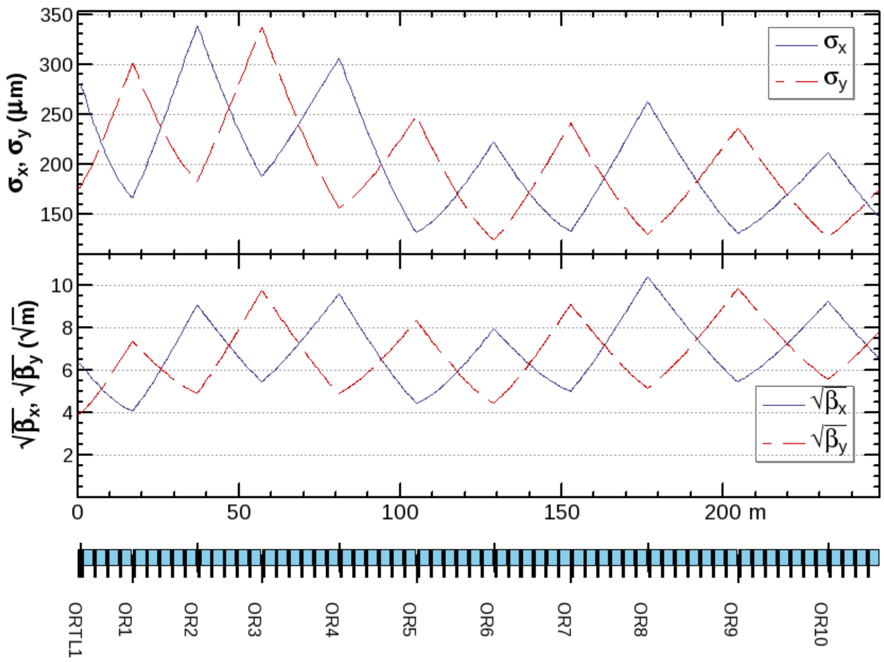

Figure 5.10. Optics of 1.54-6 GeV part of the linac.

5.7. Linac 1.54-20 GeV

The 20 GeV linac presented in Figure 5.12 actually contains the S-band linac presented in Figure 5.10 up to the quadrupole named $QC0$. The extended part can be easily distinguished since the blue boxes representing the accelerating structures up to 248.5 meter of the accelerator are larger than the downstream ones, since the earlier

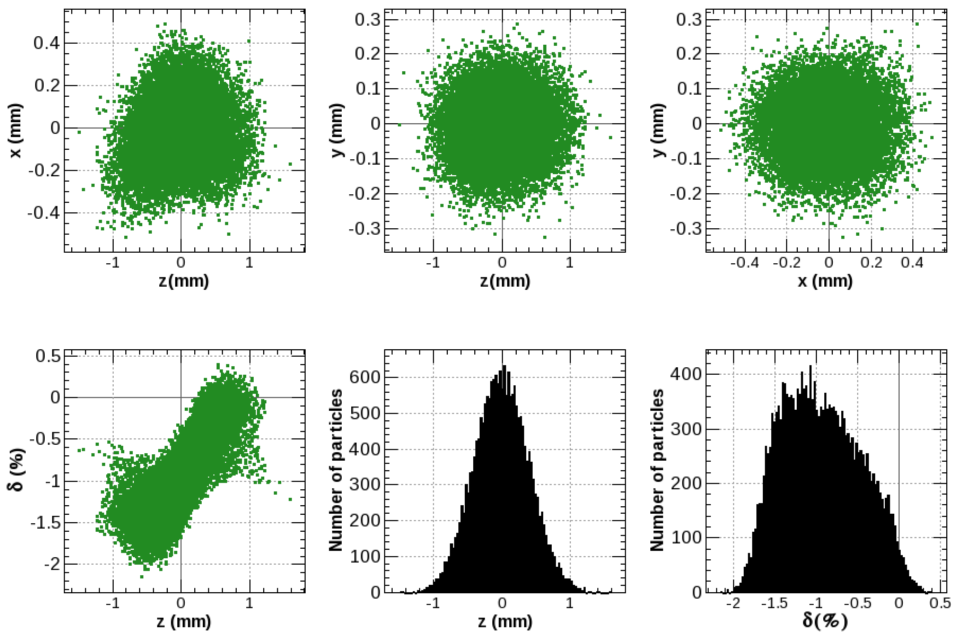

Figure 5.11. Beam Profile of 1.54-6 GeV part linac tracking with the positrons cooled in the DR.

part makes use of 3 meter-long S-band whereas the posteriors are 1.8 m-long C-band structures. Therefore, 1.54-6 GeV middle energy linac has the unit cell presented in Figure 5.9, meanwhile 6-20 GeV high energy part has the linac cell demonstrated in Figure 5.13.

20 GeV linac is the alternative option of designing a new synchrotron which seems to be 2.9 km in circumference or to use already existing SPS yet deploying wigglers and operating its optics with different phase advance [11]. When the linac is compared to the a pre-booster as a pre-injector, the linac steps forward. To illustrate, for the Z operation mode, the PRB accumulates 2080 bunches in 5.2 sec, however its cycle is 6.3 seconds, therefore 1.1 s is lost at each PRB injection compare to direct injection into the BR, therefore the delay caused due the PRB cycle is 88.8 seconds compared with the fill time 1034.8 s (see Section 4.2). Furthermore, the extraction emittance of 1.18/0.05 nm is also within the acceptance of the 98-km booster ring (BR) [7], the results of the high-energy linac are presented in Table 5.7. The disadvantage of the linac would be the emittance blow, however as long as the beam is within acceptance of

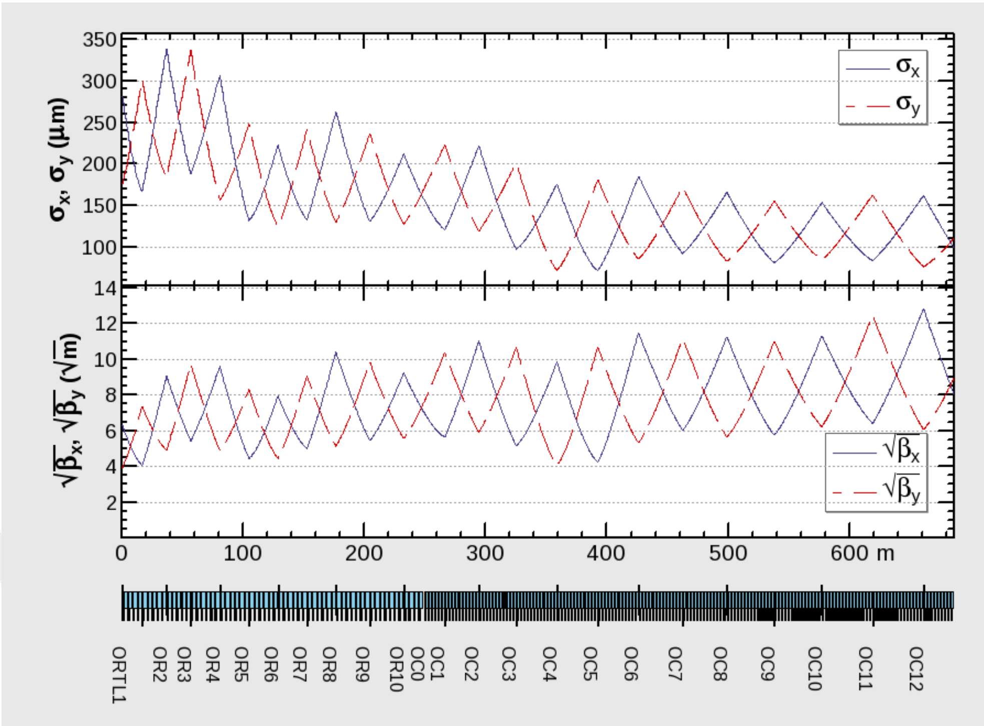

Figure 5.12. Optics of 1.54-20 GeV linac. Notice that the C-band structures start at QC0, where the S-band structures end corresponding to a beam energy of 6 GeV.

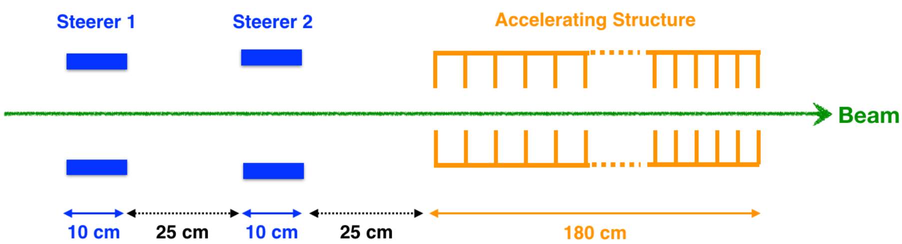

Figure 5.13. The unit cell used in the high energy part of the linac. The C-band linac (6-20 GeV sector) has 156 of these (not to scale).

the BR, the beam emittance can be cooled inside the BR, which has already assumed to store the beam for 7 damping times which will damp the injected emittance more than 3 orders of magnitude up to the BR natural emittance.

Table 5.7. Some parameters of the 1.54-20 GeV linac.

Parameter	Value
length	685.9 m
number of S-band and C-band cavities	60 and 156
number of quadrupoles in the S-band and C-band sections	12 and 13
RF pulse repetition and bunches per RF pulse	200 Hz and 2 (4*)
injection-extraction energy	1.54 GeV-20 GeV
injected emittance at 1.54 GeV (h/v)	1.9/0.4 nm
final emittance w/o blow up at 20 GeV (h/v)	0.15/0.03 nm
average extracted emittance at 20 GeV (h/v)	1.18/0.05 nm
Transmission for 3.5 nC	100%

*During positron beam delivery.

Since the high energy linac is the extension of the 6 GeV linac, the injected parameters of the beam at 1.54 GeV is the same, therefore the positron beam cooled in the DR is injected. The tracking results for 20 thousand macro-particles simulating 3.5 nC charge is presented in Figure 5.14. The banana or golf-club shape seen in the left-top and on its right are due to transverse wakefields (see Section3.2).The synchronous phase in the cavities is set to $-94°$ referring to the energy gain equation in Equation 5.1. Again, the energy gain is 1% behind the nominal as can be seen in right-bottom corner which is why the accelerator nominally designed to achieve 20.2 GeV so that with the 1% less energy gain it becomes 20 GeV, as planned.

High energy linac is the best place to discuss concepts used in linac optics design. The linac optics presented in Figure 5.6, 5.10 and 5.12 have subtle similarity in quadrupole location. The FODO lattice actually had better located if the distance between the focusing and defocusing quadrupoles spaced with the same distance. However, in aforementioned figures, the distance between the quadrupoles are increasing. It is indeed because of the Lorentz contraction, or in other words, or the distance between the quadrupoles in laboratory frame in which optics are shown needs to be increased so that the particles accelerated see the distance between the quadrupoles

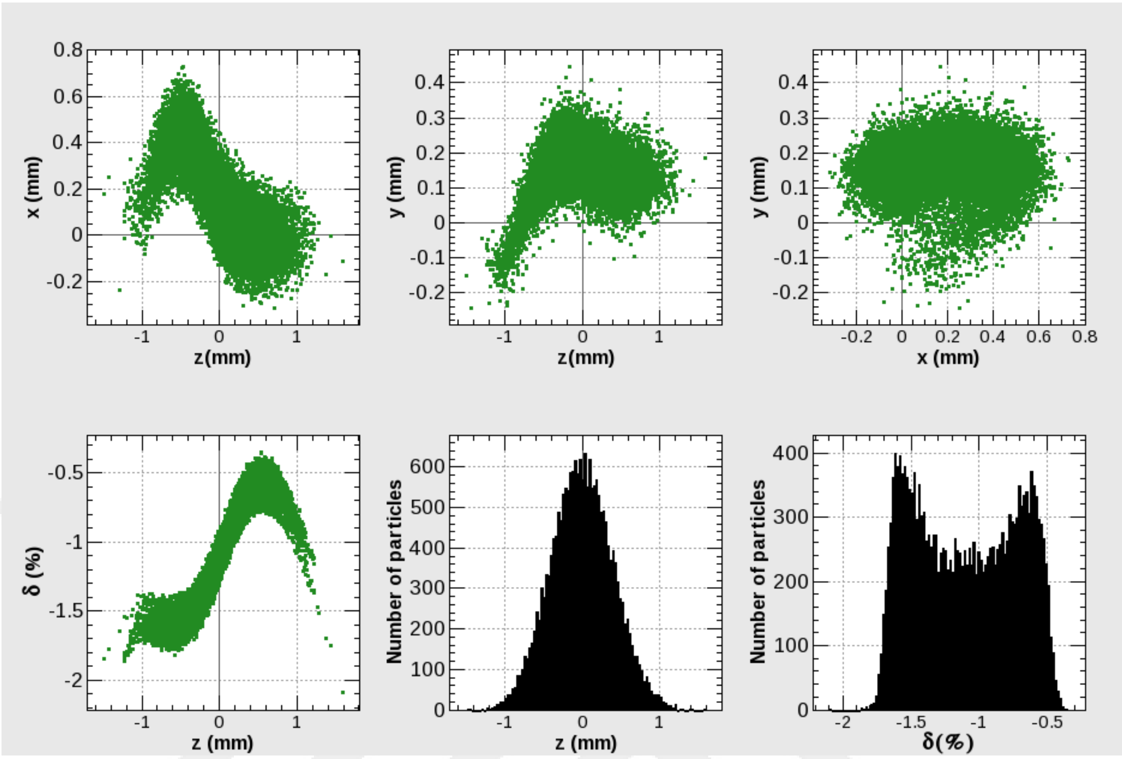

Figure 5.14. Beam Profile of 1.54-20 GeV part linac.

almost the same [55]. Surely, the spacing has to be an integer multiple of a linac cell, and this can be achieved up to a point. All in all, in a linac consisting of FODO lattice, the quadrupoles need to be located by a constant separation L^* in the particle frame, therefore the quadrupoles in laboratory frame have to be located in a distance $\tilde{L}$ which are related as:

$$\tilde{L} = \gamma_{rel} L^*. \tag{5.9}$$

The orbit steering algorithm has demonstrated tremendous results leading 100% transmission and very acceptable extraction emittance. However, recalling that the linac is normal conducting both in terms of cavities and magnets, the strength of the steerers have to be checked so that they stay within normal conducting limit. If we recall Equation 2.38, we will see the magnetic field of the steerer (which is a dipole):

$$B_{corrector} = \frac{B\rho}{l_{steerer}} K_0 \tag{5.10}$$

where $l_{steerer}$ is the steerer length which is determined to be 10 cm up to 20 GeV section, as shown in Figure 5.13. It turns out that the strength of steerer deployed will vary below 100 Gauss. Similarly the quadrupole strengths are all below 0.8 Tesla, which is the limit, for an aperture of 15 cm, and the quadrupole lengths are 35 cm at high energy region. All in all, it will be useful to see the orbit oscillations controlled by the steerers (i.e. corrector) to overcome misalignments, which is shown in Figure 5.15.

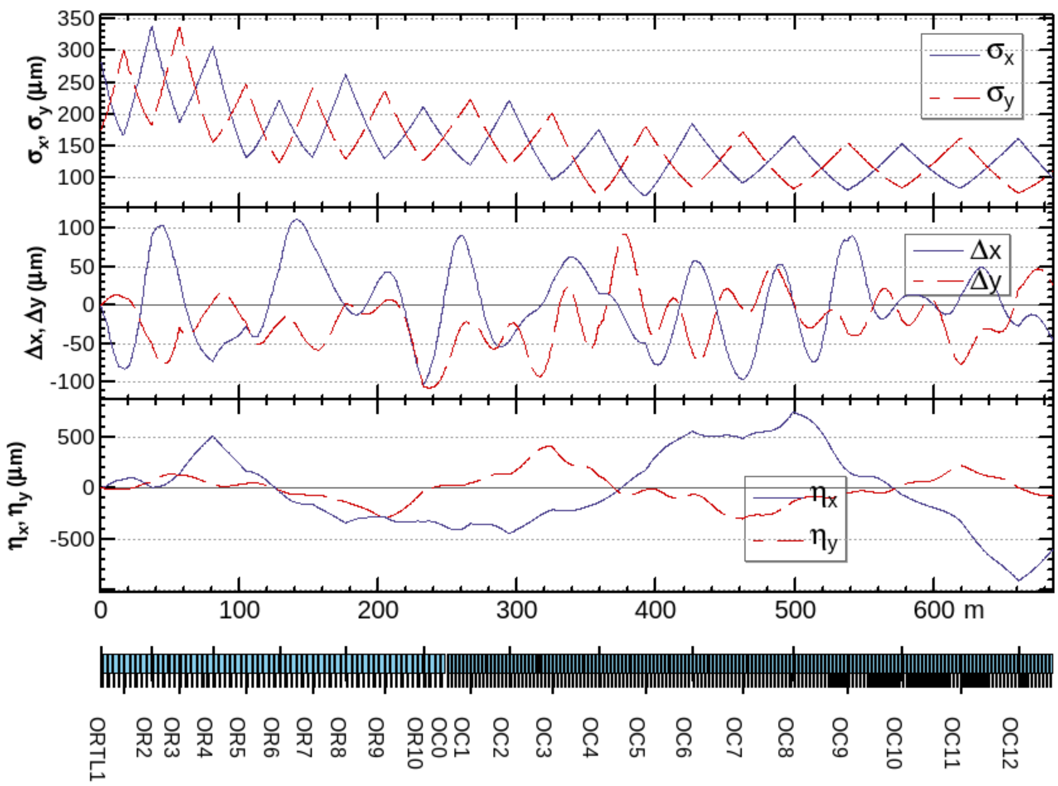

Figure 5.15. Beam size, orbit oscillation, and dispersion function of 1.54-20 GeV part linac, respectively.

5.8. Beam Loading and SLED

The accelerating structures used in the linac are traveling normal-conducting structures in where the RF power is fed from one end and exit from the other end, as shown in Figure 5.6.

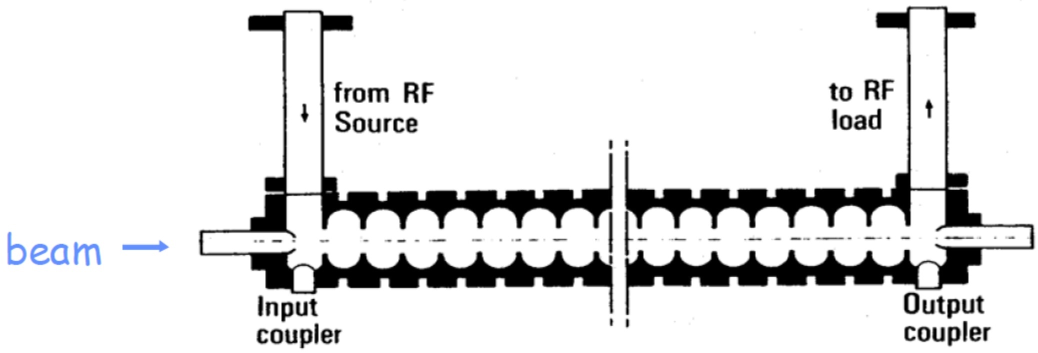

Figure 5.16. In travelling wave structure, the RF wave is fed from the entrance (w.r.t. the beam) and circulating out from the exit.

In this section, the aim is to stress conceptually how we are going to feed the cavity so that the gradient of 25 MV/m with Φ =20 mm in S-band and 50 MV/m with Φ =14 mm can be achieved. Apart from the high gradients, we also push the limits of linac repetition which is in our case 200 Hz and 2-4 bunches per pulse. Therefore, a standard klystron feeding mechanism would not be enough, but a combination of them would suffice. The concept RF power waves superposition was the key advancement to reach Stanford Linear Collider [56], and therefore to reach even more challenging FCC-e^+e^-. Basically, to increase the strength of RF power output, two waves from two klystrons are set to constructively superpose their power waves, which is known as SLAC Energy Doubler (SLED) can be found in details in Ref. [57]. Indeed the SLED power output is such an advancement giving way to achieve higher gradients in the cavity as well as multi-bunch acceleration within one pulse. The SLED could carry even more bunches if the power gain versus beam loading compensation is handled. For instance, SLC had accelerated 3 bunches per RF pulse as shown in Figure 5.17. Moreover, the multi-bunch acceleration of high intensity short bunch length has been

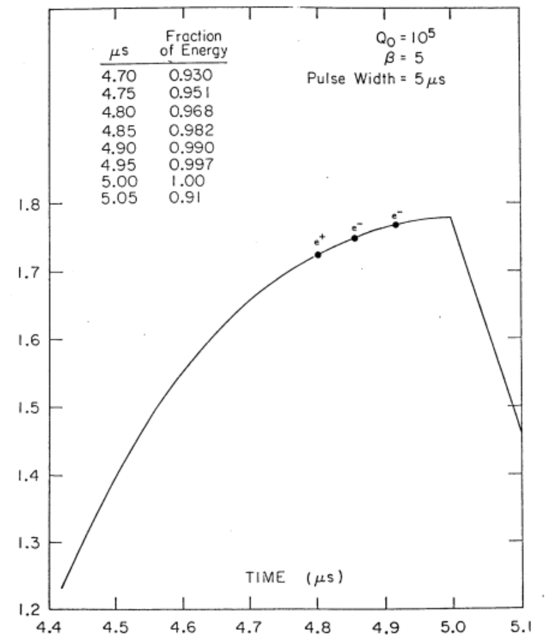

Figure 5.17. SLED II type RF pulse accelerating 3 bunches [58]. The energy gain of a bunch depends on the arrival time to the pulse, and the beam loading should be ramped such that the beam loading and the rise of the power are equal. In the end, the energy gain of the three bunches become the same.

also studied at KEK, 5 bunches of 10 nC each are successfully accelerated in one RF pulse [59]. All in all, we can conclude that the power compressor would be sufficient to satisfy the assumptions made for the linac. The exact calculation of beam loading, and accordingly tapering of the cavity aperture in order to keep the field uniformity etc. will be studied by the CERN RF Engineering group.

6. POSITRON BEAM AND BEAM TRANSFER LINES

The positrons will be generated by impinging electrons on a target inside the linac at 4.46 GeV. Wherefore, their 6D phase space distribution is more randomized compared to the electrons which are created by a laser flashing on a photocathode, in which the pulse length, transverse emittance can be easily manipulated. Therefore, except the low energy linac in Section 5.5 which will be used merely by the electrons, the pre-injectors take positron beam as reference since it is more challenging. Regarding the probable transmission loss in the capture and acceleration of positrons inside the remaining 1.54 GeV part of the linac, some safety margin is allocated for the incident electron charge into the positron target. In other words, the FCC- e^+e^- injectors can impinge the target with up to 10 nC of electron bunch at 4.46 GeV in order to achieve 3.5 nC of positrons at 1.54 GeV at the end of 6 GeV linac [11].

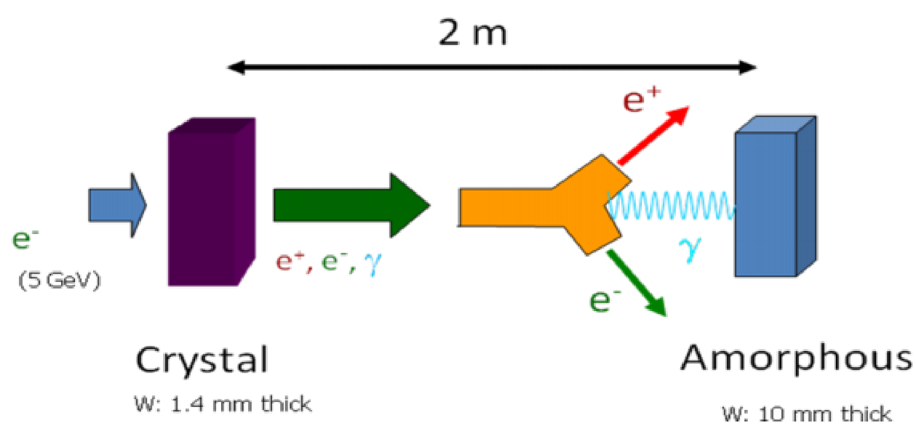

Figure 6.1. The hybrid target scheme consists of a crystal followed by an amorphous, considering the yield and energy expectations, the FCC-e^+e^- hybrid target scheme may resemble to CLIC [60] .

The positron-converter simulations are retained for both conventional and hybrid targets. The conventional target refers to a single refractory material with high atomic mass to increase interaction cross-section, whereas the hybrid target, as the name evokes, consists of a crystal and an amorphous targets, as depicted in Figure 6.1. The hybrid target selection makes use of challenging radiation i.e. photons for the positron generation. Besides, the two-step converter has a better heat dissipation and is a better absorber of the shock wave created by the impinging high energy and high charge electron beam. Commonly, in both converter types, tungsten like materials as crystal are used. Distinctively, the thick tungsten is replaced with a thinner tungsten crystal for radiation generation and then it is followed by a granular or bulk amorphous which is the converter in the hybrid scheme [61].

In Figure 6.2, the conventional target length versus positron production yield has been presented, and the target thickness would suffice the FCC-e^+e^- demands determined to be 15.75 mm thick tungsten foil where the tungsten radiation length is denoted as X_0 corresponding to 3.5 cm. The power deposited in the target is calculated to be 2.8 kW per pulse. For max e^- charge of 8.8 nC (i.e. net of transmission loss out of 10 nC e^- in a bunch sent from the thermionic gun), e^- beam energy is 76 J (2 bunches per RF pulse with 200 Hz of linac repetition), in other words, the average e^- beam power on the target is 15 kW [62].

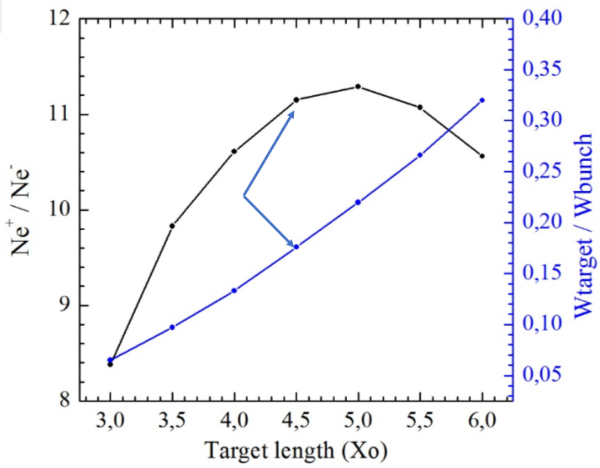

Figure 6.2. Optimisation of conventional positron target thickness with positron yield (left vertical axis), and total energy deposition in tungsten target is normalised by the total electron bunch energy (right vertical axis) [62].

6.1. Positrons Injected into the DR

The optimisation of positron targets, flux concentrator as well as accelerating structures surrounded by the solenoids and triplets are currently on going for the FCC-e^+e^- [63, 64]. Meanwhile, the e^+ beam used in the FCC-e^+e^- injector simulations are taken from KEK [65]. At KEK, the positrons generated from the 14 mm tungsten (i.e. conventional) target goes through an adiabatic matching device which can provide a pulsed magnetic field of 6.2 T at peak where the flux concentrator is spiral shaped and tapered [66]. After the adiabatic capture section, the generated large emittance beam is kept focused transversely and accelerated at the same time thanks to cavities surrounded by the approximately 15 meter long solenoid. The aim is again to keep the transmission high and accelerate as much as possible so that the adiabatic damping will take place and make the beam smaller. The KEK positron capture, and the sketch of the pre-injector linac can be seen in Figure 6.3 and Figure 6.4, respectively.

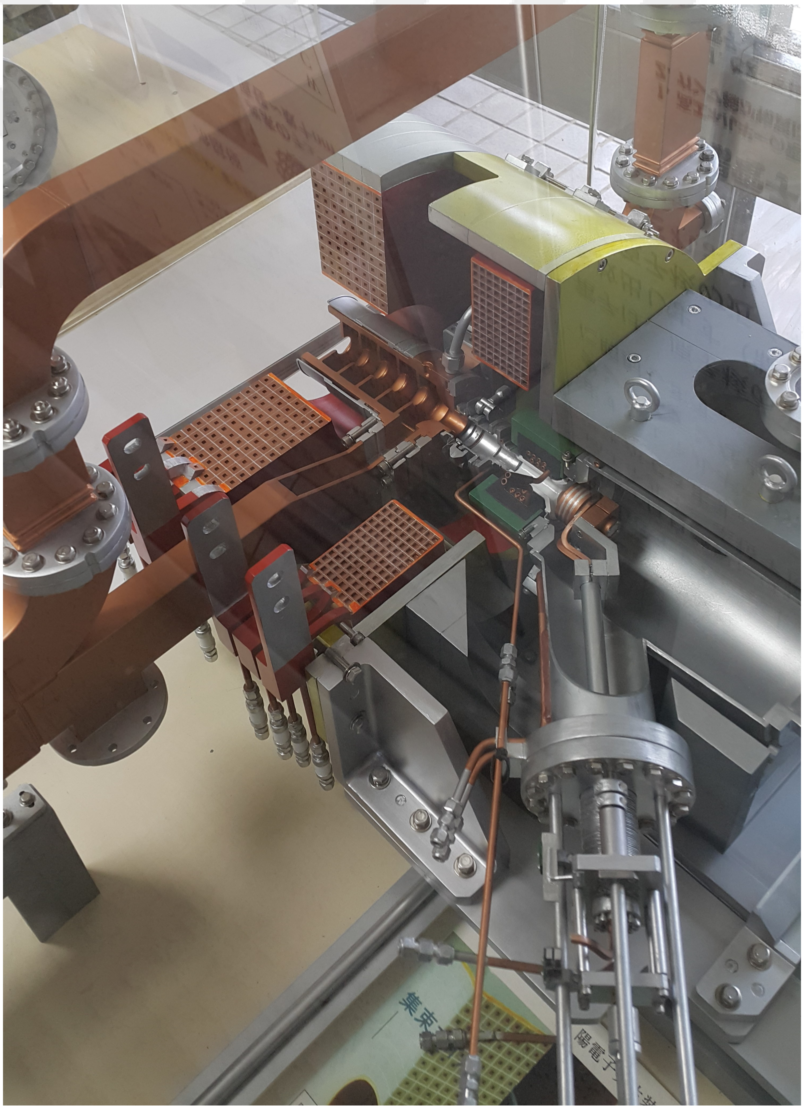

Figure 6.3. KEK positron generator and capture section exhibited in the KEK linac control room.

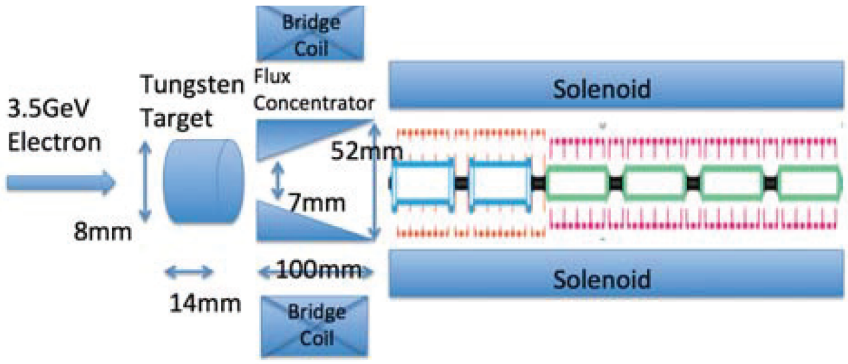

Figure 6.4. Sketch of the KEK positron generator and capture section. The capture section is followed by the accelerating structures with larger (i.e. 15 mm radius) and standard S-band structure of 10 mm radius which are all surrounded by a solenoid for transverse focusing during acceleration (not to scale) [66].

After, the positron capture section in SuperKEKB linac, the S-band cavities of 2 m length are surrounded by the triplets quadrupoles are accelerated up to 1.1 GeV in the linac. However, the large emittance beam cannot be all injected into the DR. SuperKEKB first collimates the energy spread ±12% (in total) positron beam to ±5% (in total). Those positrons goes through energy compressor system (ECS) in which their energy spread is altered thanks to the cavities and chi-cane magnet orientation. The ECS compresses the beam energy spread to one fifth, resulting in 1% (in total) so that the beam is matched to energy acceptance of the SuperKEKB damping ring [67–69]. On the other hand, the energy acceptance of the FCC-e$^+$e$^-$ DR is about ±7%. Therefore, it makes the ECS unnecessary in terms of energy spread-bunch length manipulation. The problem of not deploying an ECS before the DR would be not being able to alter longitudinal β function, which will be discussed in the Chapter 7. All in all, the collimated positron beam of KEK simulated up to 1.1 GeV is injected into their ECS which is shown in Figure 6.5.

Therefore, the beam shown in Figure 6.5 is the beam to be adjusted to the FCC-e$^+$e$^-$ parameter selection and used in the DR. Therefore, the injected beam needs to be matched to the DR in Chapter 7 thanks the designed beam transfer line (BTL)

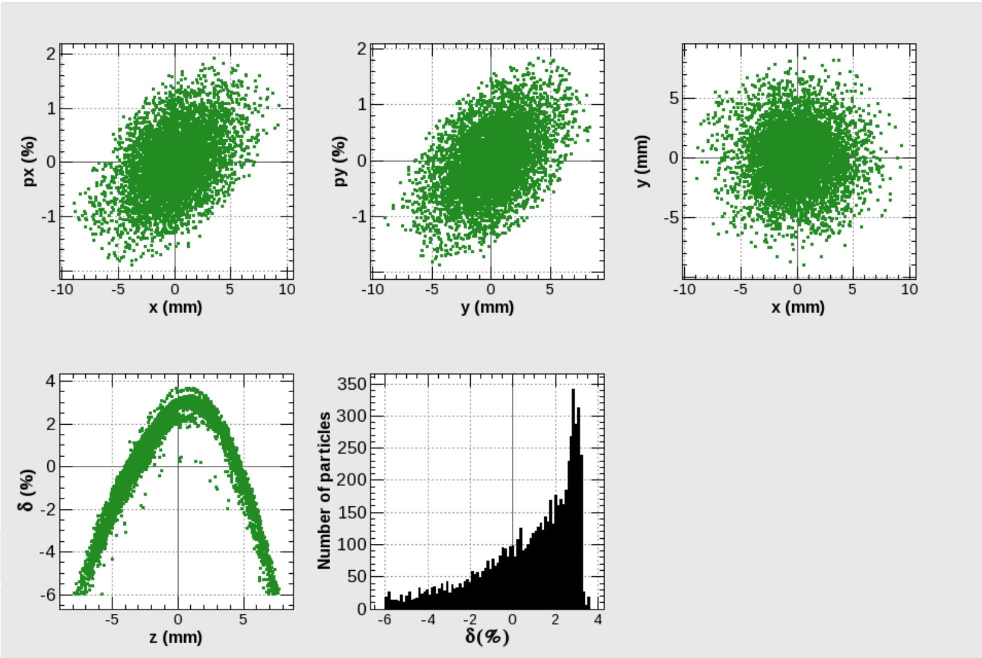

Figure 6.5. Collimated KEK positron data to be fed into their ECS as well as into the FCC-e^+e^- LitoDR.

presented in Figure 6.6 and the parameters listed in Table 6.1.

Table 6.1. The beam parameters transformed by the LitoDR.

Parameter	before LitoDR	after LitoDR
ϵ_x	1.26 μm	1.26 μm
ϵ_y	1.21 μm	1.21 μm
ϵ_z	75.5 μm	75.5 μm
α_x	-0.47	0.006
α_y	-0.51	0.006
α_z	-0.15	-0.15
β_x	4.71 m	4.00 m
β_y	4.74 m	6.38 m
β_z	0.15 m	0.15 m

Table 6.1 is the perfect spot to stress the underlying reasoning behind the beam transfer line. A beam transfer line is meant to keep the emittance intact meanwhile

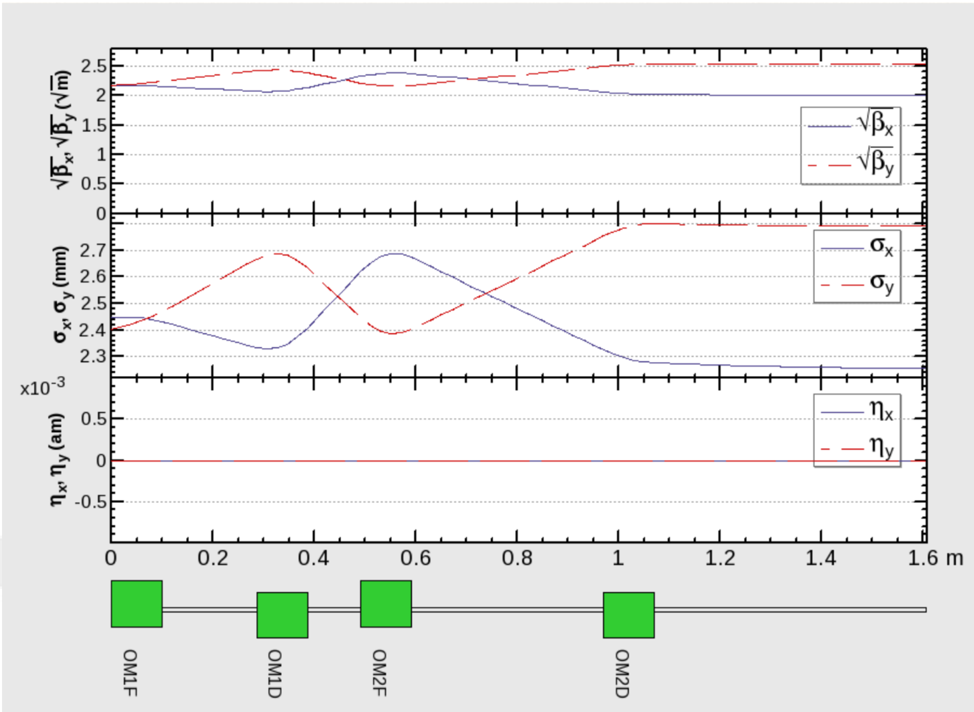

Figure 6.6. Beam transfer line designed to match positrons from linac to the DR (LitoDR).

matching the α, β transfer parameters for the 3D spatial plane. Recalling from Section 2.8, the required parameters to be matched are $(\beta_x, \alpha_x, \beta_y, \alpha_y, \eta, \eta')$. We matched the first four, and kept dispersion and its derivative zero meanwhile emittance is preserved. However, LitoDR presented in Figure 6.6 is a BTL merely matching the transverse Twiss parameters, namely α_x, β_x,α_y, β_y where DR ring has $\alpha_{x,y}$=0 at injection point. Furthermore, the DR has β_x=4.00 m and β_y=6.38 m which are matched. However, the longitudinal plane has β_z=2.97 m which is clearly not matched. Actually, without a cavity and chi-cane (an orbit bump consists of 4 or more dipoles to alter the energy spread of the bunch), the longitudinal parameters cannot be matched. Therefore, if the beam, whose parameters are tabulated in the right column of Table 6.2 and whose profile is presented in Figure 6.7, is injected into the DR, it will longitudinally filament within the RF bucket, and those particles which exceed the bucket height or length will be lost.

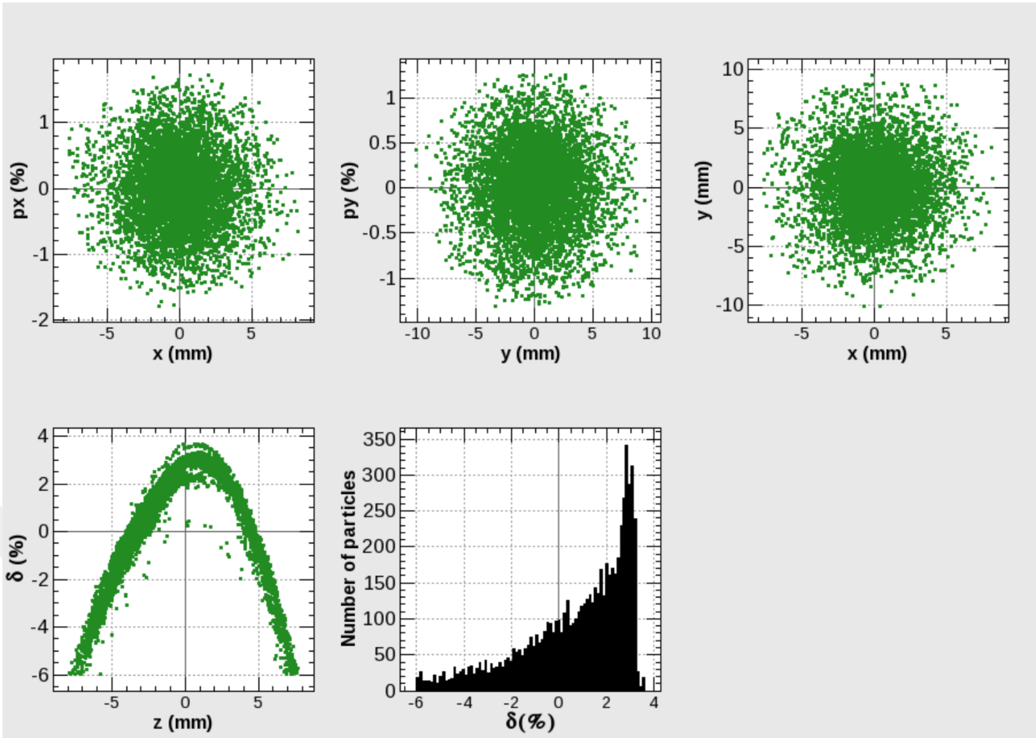

Figure 6.7. The transversely matched beam which will be injected into the DR. The weighted average of the beam is put to the longitudinal center. Transversely, the beam becomes a circle and $\alpha_{x,y} = 0$ are achieved, which refer to an ellipse that is not tilted in the phase space.

6.2. Matching the Beam from DR to Linac Re-injection Point

Ring and transport line (a line which is not periodic, eg. linac) have specific characteristics in terms of Twiss functions. For instance, linac results in a smaller bunch length, yet with larger energy spread in contrast to a ring. Therefore, as we may need an energy compressor before injecting into the DR, we need the bunch compressor to do the opposite transformation, namely to shorten the bunch length and increase the energy spread. The bunch compressor of the FCC-e^+e^- can be found in Ref. [8], which is depicted in Figure 6.9. The beam profile acquired by tracking through the BC is presented in Figure 6.9. Indeed, the bunch compressor diminished the rms bunch length from approximately 5 mm to 0.5 mm. The short bunch length is crucial for the linac since the S-band RF wave is as short as 10.5 cm yet the whole bunch needs to catch approximately the crust of the sine-wave for high-gradient acceleration.

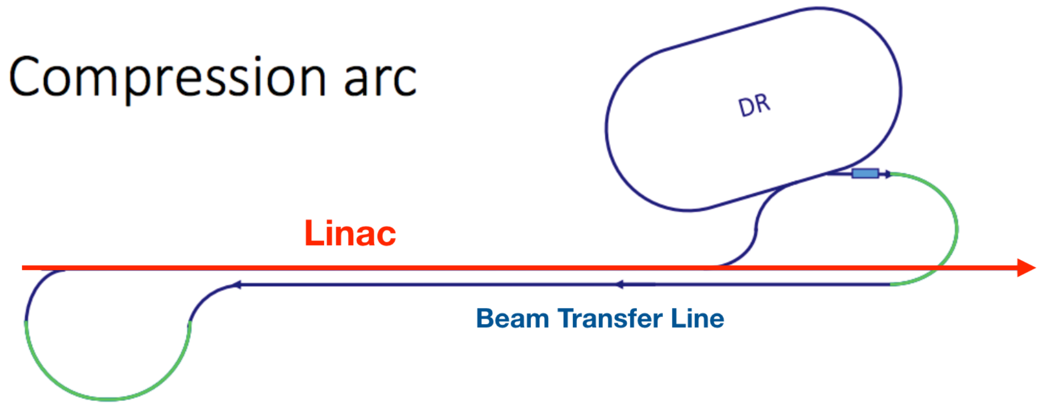

Figure 6.8. The dogleg bunch compressor (shown in green) will squeeze the bunch length and increase energy spread extracted from the DR for linac re-injection [8].

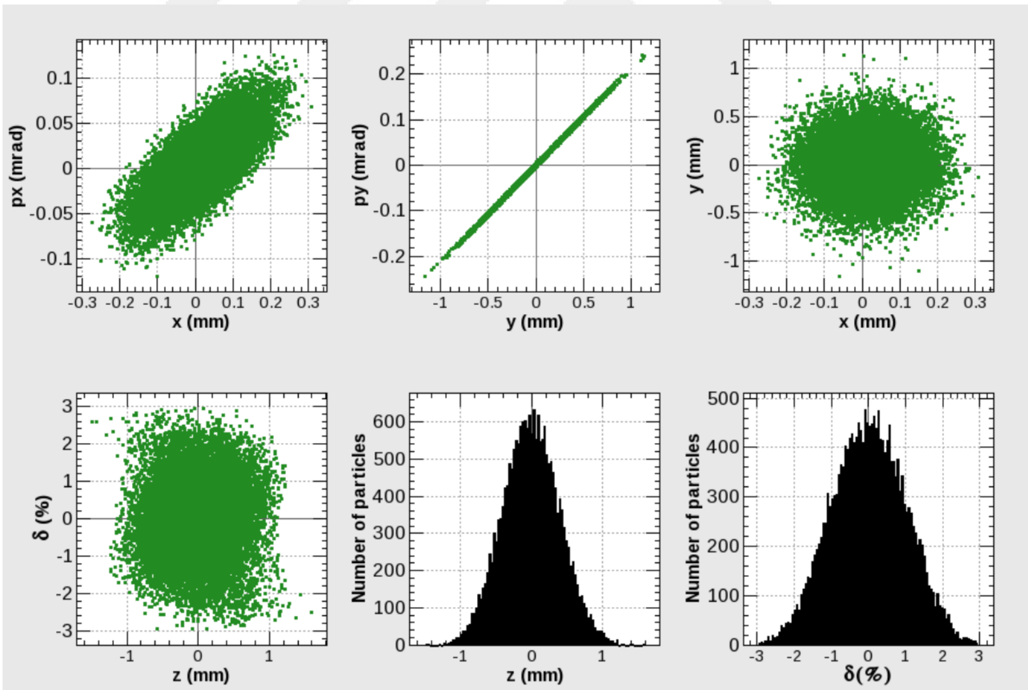

Figure 6.9. The beam profile tracked through the bunch compressor.

The beam presented in Figure 6.9 is matched to the linac via the BTL, called BCtoLinac, shown in Figure 6.10. Therefore, the BTL designed simply transforms the parameters tabulated in Table 6.2.

Table 6.2. Parameters of the bunch compressor (BC) is matched to the linac via the beam transfer line (BCtoLinac).

Parameter	before BCtoLinac	after BCtoLinac
ϵ_x	1.86 nm	1.86 nm
ϵ_y	0.44 nm	0.44 nm
β_x	3.49 m	39.5 m
β_y	145.8 m	15.6 m
α_x	-1.08	0.006
α_y	-31.31	0.085

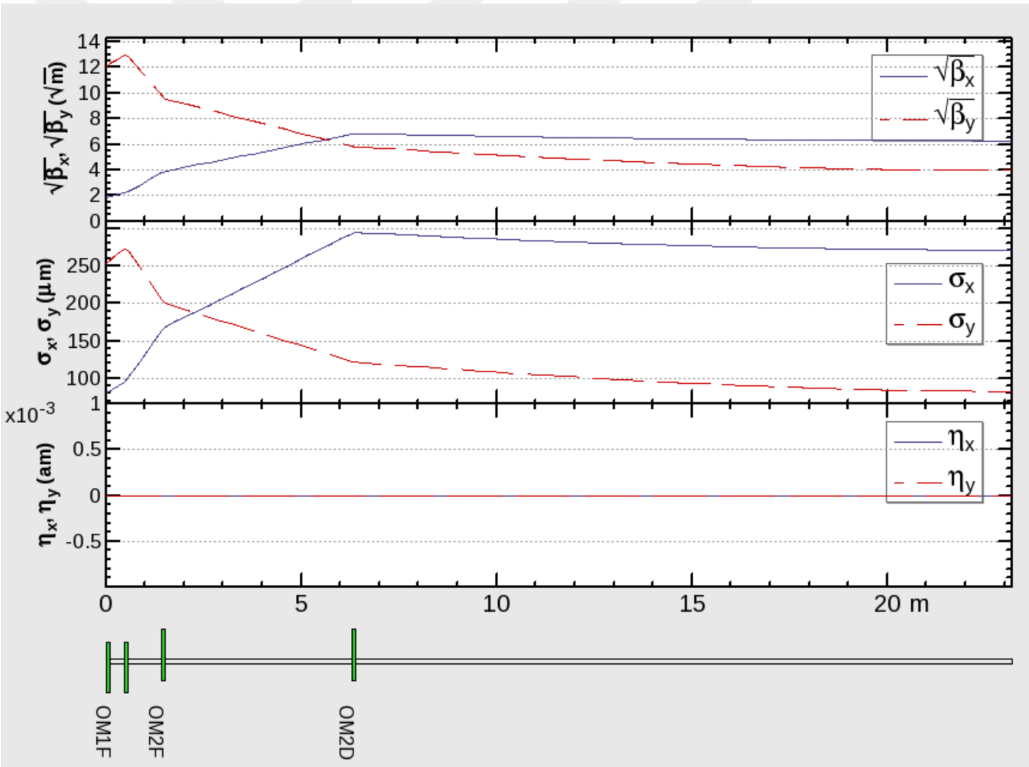

Figure 6.10. Beam transfer line designed to match the beam from bunch compressor to the linac at 1.54 GeV re-injection point.

This matching has better done at the turnaround loops, yet this BTL was needed solely to proceed with the linac simulations. In the end, the beam is ready to be injected back to the linac at 1.54 GeV, as seen from its profile presented in Figure 6.11. This beam is utilized in Sections 5.6 and 5.7.

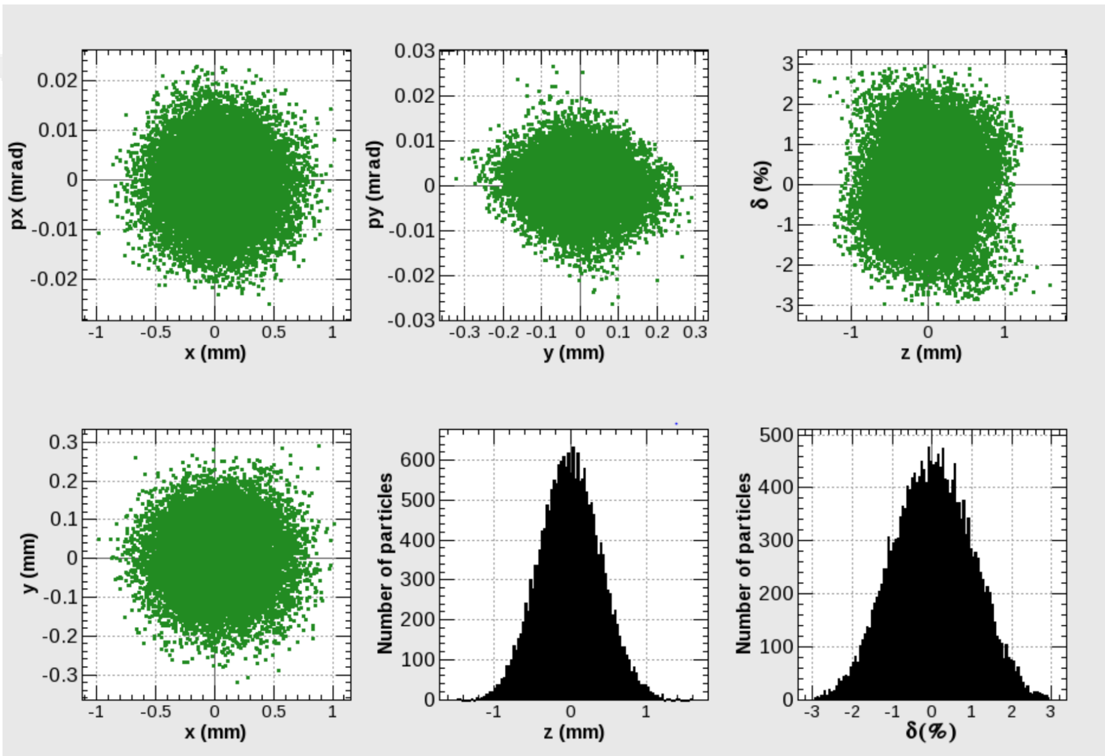

Figure 6.11. The beam is tracked through the BCtoLinac. This is the beam injected to the linac at 1.54 GeV.

7. DAMPING RING

The damping ring (DR) cools the beam emittance in 3 dimensions thanks to synchrotron radiation and acceleration of the particles along z-axis in the cavity. Therefore, its energy as well as radius are determined primarily based on Equation 2.82. Nonetheless, there are many more requirements to meet such as large enough 6D dynamic aperture for the acceptance of positrons, spin tune polarization, instabilities, circumference to determine the number of bunches/trains to host, etc. The DR will host 8 trains, each with a pair of bunches. The spacing of 16 bunches will be about 50 ns and keep each of them inside for 40 ms (see Section 4.1). Therefore 800 ns at 1.54 GeV DR energy would refer to a circumference of 240 m ($\beta_{rel} \approx 1$), which turns out to be 241.8 m ($\sim$807 ns at $\beta_{rel} \approx 1$) in our DR. The depiction of the DR is shown in Figure 7.1.

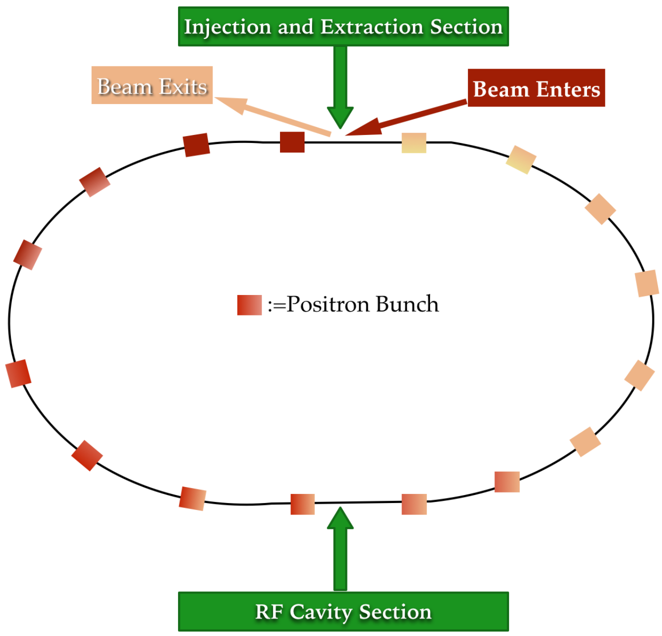

Figure 7.1. The DR will host 8 trains, each of which conveying a pair of bunches. As the bunches circulate in the DR, their emittance will be cooled. The last injected pair is shown darker, and the first injected pair is shown in a lighter color, associating the radiation cooling to the gradual lightening of the color.

The primary reason of having the DR is to cool the positron beam since positrons created by hitting the target, their energy spread and beam size are way larger than the electrons at the same energy. Therefore, it is reasonable to take the positron beam as reference and continue calculations with those even though the electrons will be cooled in the DR, as well. The emittance of the beam depending on the store time t in the ring is:

$$\epsilon(t) = \epsilon_{inj} e^{-2t/\tau} + \epsilon_{eq}\left(1 - e^{-2t/\tau}\right), \tag{7.1}$$

where ϵ_{inj} is the injected emittance, ϵ_{eq} is the equilibrium (a.k.a. natural) emittance of the ring with the damping time of τ [31]. Equation 7.1 is natural to be exponential like in the case of radiation decay, and the power 2 of the exponential is due to the emittance which has dimension of area, also it is valid for the emittance in x, y and z. Therefore, we can reflect on this equation immediately. The positron emittance at 1.54 GeV is at the order of few μm in transverse (i.e. almost radially symmetric) therefore if we need to damp them in 40 ms, we need to have a transverse damping time of 10 ms so that the extracted emittance become at the order of nm. Indeed, this statement is the summary of the whole design of the DR.

The optimization of the DR is to achieve small damping time τ and appropriately small equilibrium emittance. Hence, we need to increase the emitted synchrotron radiation while keeping the dynamic aperture large which can all be achieved by deploying *wigglers* in dispersion free section (i.e. straight section of the circular accelerators). The DR consists of two straight and two arcs. Therefore, we will discuss the structure of the DR, then return back to the whole overview.

7.1. Arc

The circular part of the ring consists of two arcs closing the trajectory. Each arc has 57 unit cells. The unit cell is a FODO lattice with sextupoles, as shown in Figure 7.2. The FODO lattice simply contains 2 dipoles, 2 quadrupoles and 2 sextupoles. A rectangular dipole in the arc is 21 cm, creating 0.66 Tesla field bending

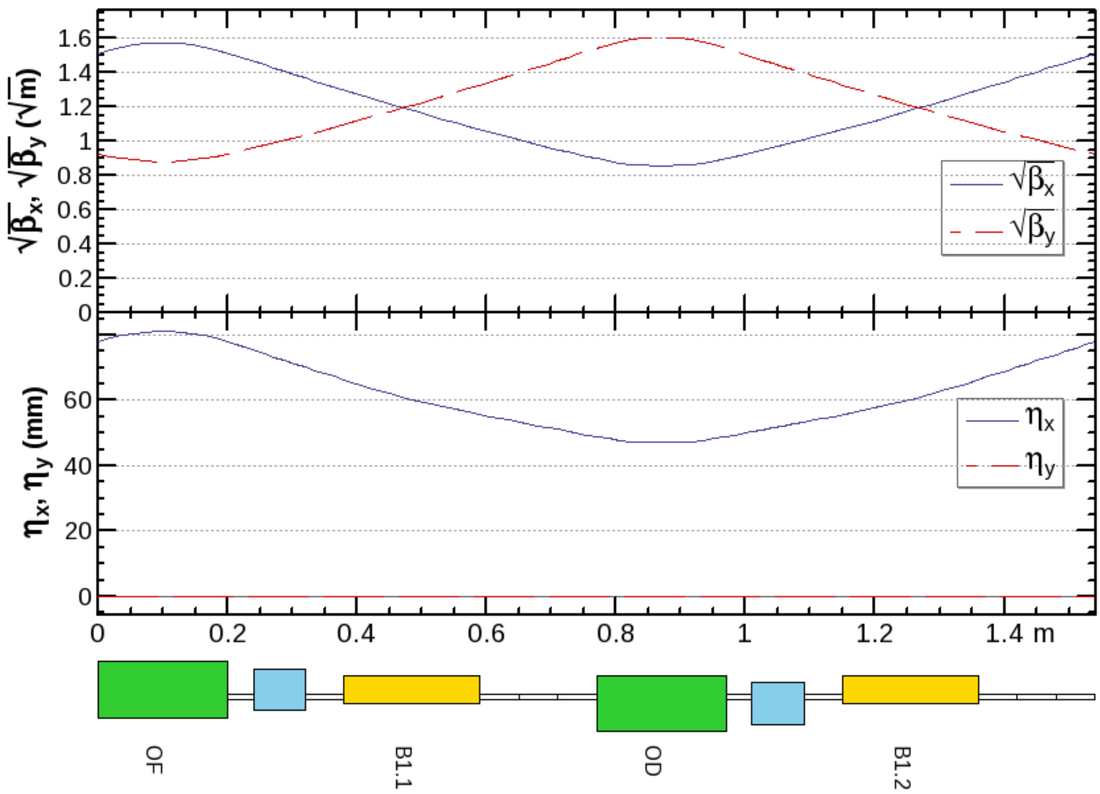

Figure 7.2. Unit cell made of FODO lattice. The green boxes are the quadrupoles, blues are the sextupoles, and the yellow rectangles are the dipole bends.

the beam by approximately 1.552°. Quadrupoles and sextupoles in the arc are placed with alternating older, to focus and to correct chromaticity respectively. The phase advance chosen is optimized to be 69.5°/66.0° (h/v) respectively. Totally, there are 114 unit-cells in the DR. Therefore, each cell has the same Twiss parameter at its start and end to conserve the periodicity. The natural emittance of the lattice is 1.3 nm, and a ring consisting of this cells would have reached a similar equilibrium emittance, however the ring will have wigglers in the straight section to reach just below 1 nm equilibrium emittance which is our goal.

7.2. Straight Section

There are two different straight sections designed, one is used for the injection and the extraction of the beam and the opposite section is used to deploy the RF cavities. In the arcs we have bended the beam by 114×2×1.552°=353.86°, actually we reserve 4 more dipoles of the same kind to complete the circle. The four dipoles will put to the end and start of the each straight section to form *missing dipole dispersion suppressor* [20]. Dispersion suppressors are needed to enter the cavity and wigglers dispersion free in order to avoid emittance blow, and to let cavity and wiggler do their job and cool the emittance. One of the dispersion suppressor is presented in Figure 7.3. In each straight section there are two dispersion suppressors due to the symmetry.

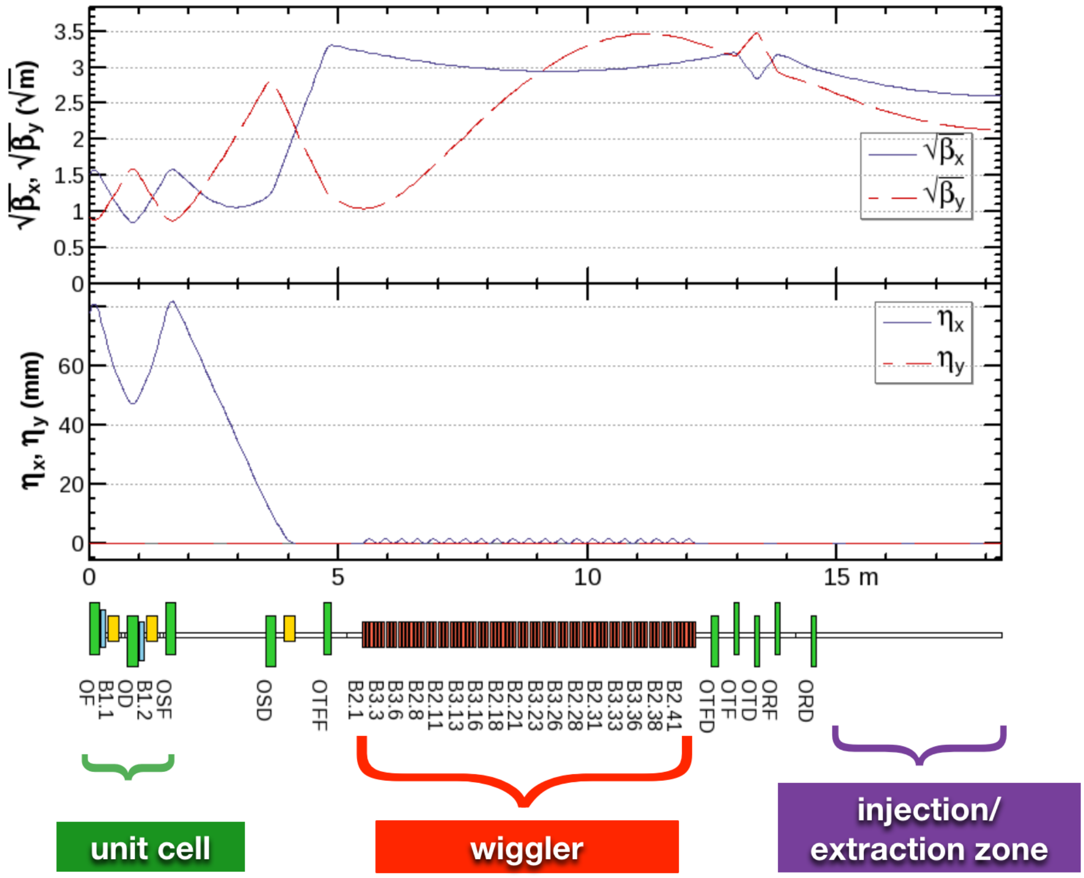

Figure 7.3. Missing dipole dispersion suppressor with the drift space for injection/extraction. Notice that the yellow boxes refer to the dipoles, the green ones are quadrupoles, light blue are the sextupoles, and the wiggler dipoles are in red.

When a ring is designed, normally we design one half of it and the other half is its mirror image, and of course, these two are to match in 6D with precision well-below 1 μm and 1 μmrad in spatial and momenta spaces respectively. Therefore, we will simply formalize the geometry of the DR as (suppressor #1, arc, suppressor #2) and then its mirror image will the other half. Keeping the same analogy, suppressor #1 was Figure 7.3, suppressor #2 is the one with the RF section presented in Figure 7.4.

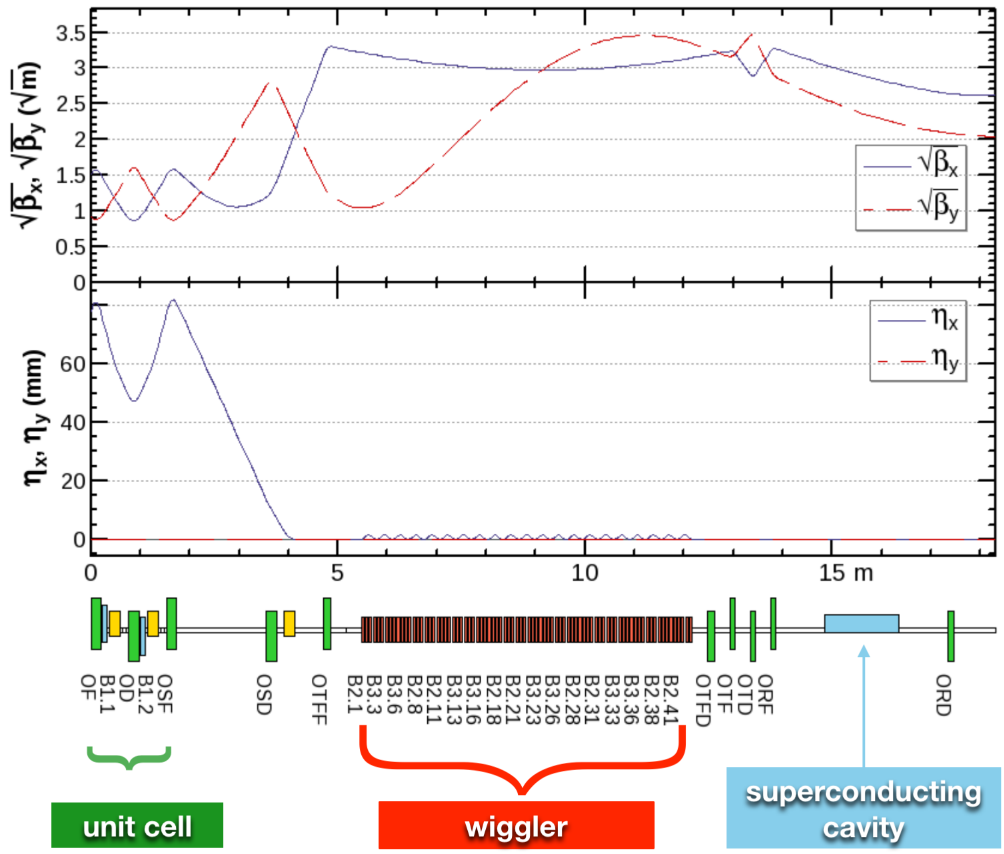

Figure 7.4. Missing dipole dispersion suppressor with RF section. Notice that the yellow boxes refer to the dipoles, the green ones are quadrupoles, light blue are the sextupoles, and the wiggler dipoles are in red.

Figure 7.4 also demonstrates the extension for the cryogenics. Since the cavity is superconducting, we need to also allocate some space for its cooling system, therefore even though the cavity length of the DR is determined to be 1.5 meter, the space allocated is 3.5 m, in other words, 1 meter drift space each in optics given from upstream and downstream of the cavity.

7.2.1. Cavity

Regarding the fact that the revolution frequency of the beam is very high in the DR such that $1/807$ ns ≈ 1.2 MHz, it is reasonable to deploy super-conducting cavities in which the energy fed is transferred almost fully to the beam compared to the normal-conducting cavities. After choosing the type, the frequency is also a matter of optimisation. The smaller frequency means larger wavelength, therefore larger separatrix (i.e. longitudinal acceptance), which is in favour of the designer. On the other hand, smaller frequency limits the achievable cavity voltage. To sum up, we have chosen LHC type superconducting RF cavities to utilize in the DR, and even keep the gradient 5 MV/m as in the LHC. Actually, higher gradients for 400 MHz have been already achieved, however we aim to be able to re-use the already available cavities at CERN. An exhibited cavity of LHC can be seen in Figure 7.5. The number of cells in the cavity will be determined by the CERN RF group later on.

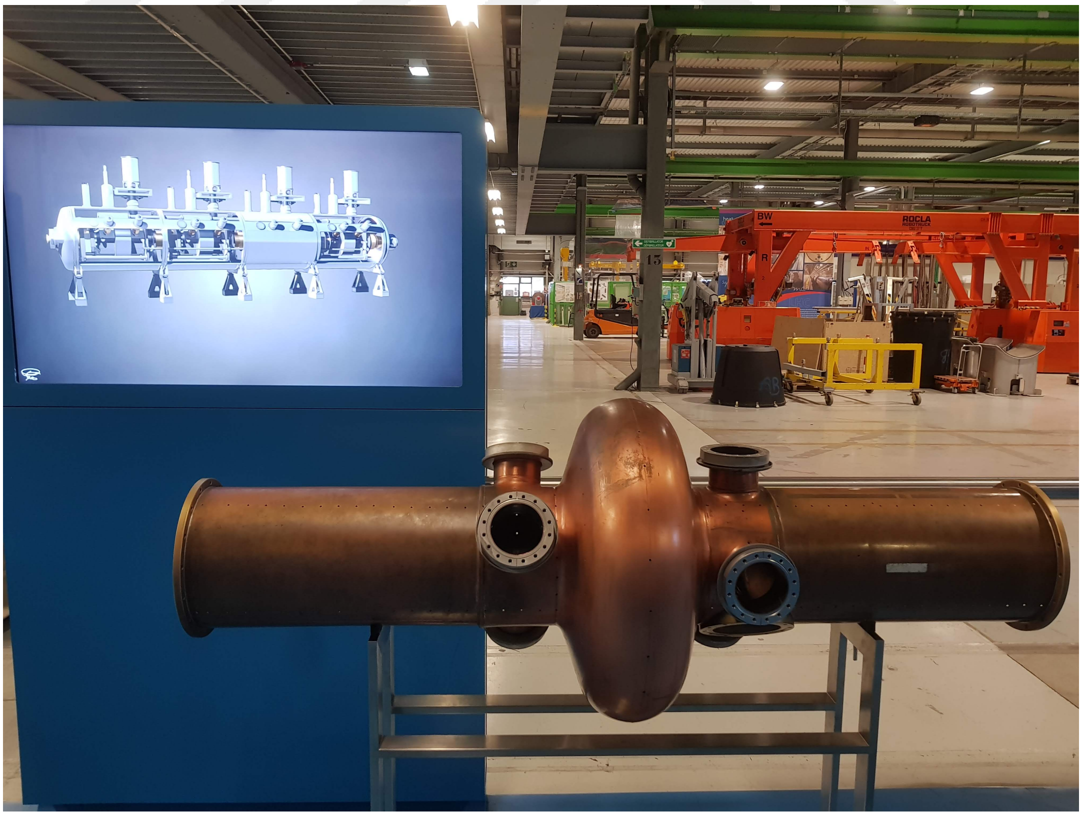

Figure 7.5. Superconducting cavity of the LHC. The similar cavity will be deployed for the FCC-e^+e^- ring. Credit: CERN SM18.

7.3. Wiggler

We have two different straight sections, each has 2 suppressors of its own kind. However, the common element for the 4 dispersion suppressor sections is the wiggler magnet, as shown in Figure 7.6. Thus, there are 4 wigglers in the DR, two located at each side. The wiggler length is 6.64 m. The wiggler period is repetition of a chi-cane: North-South-South-North poles or vice versa, therefore creating a bump on horizontal axis, and closing itself as it should be. Each pole is 5 cm and located 3 cm away from the next pole, creating a magnetic field of 1.8 T which is in the normal conducting limit for a dipole.

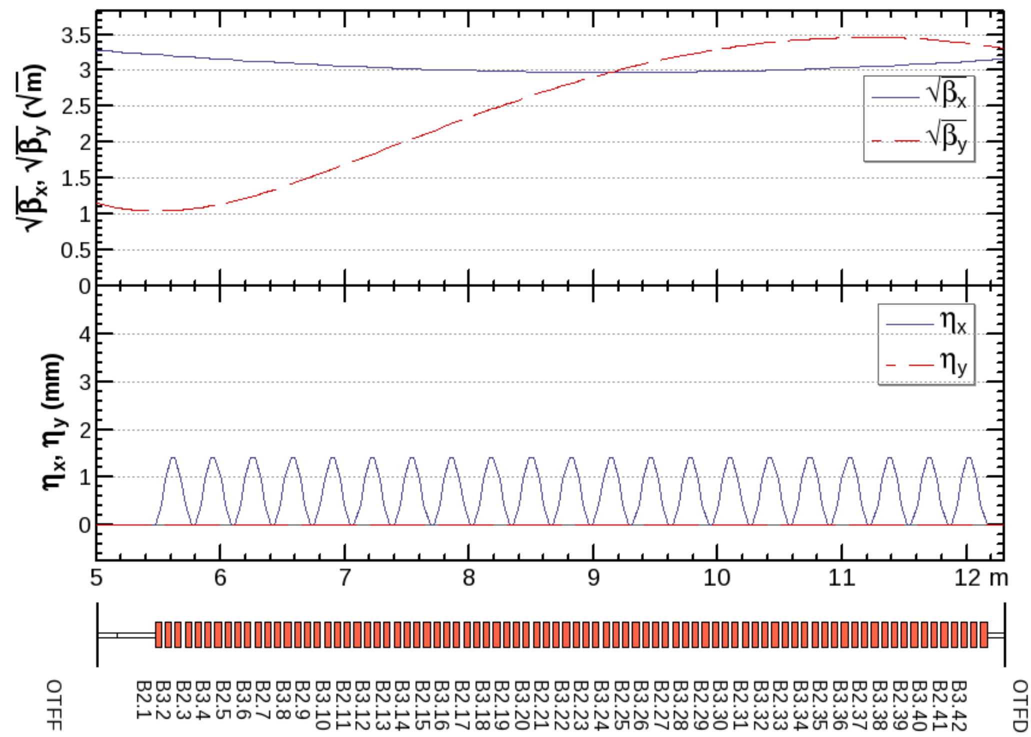

Figure 7.6. Optics of the wiggler in straight section.

7.4. Spin Tune Polarization

The FCC-e^+e^- aims for precision study of the subatomic particles, therefore it requires better definition of initial conditions of the collision. One of the parameters is the spin of the electron and positron beams. The polarization of the electrons can be achieved directly from the RF gun [70]. However, positron spin tune polarization cannot be directly achieved, yet can be obtained in the damping ring by the synchrotron radiation [71]. However, radiative spin tune polarization requires long time namely order of minutes, whereas the allowed storage time is 40 ms in the FCC-e^+e^- damping ring. Therefore, even though currently we don't plan to polarize the positrons (at least in the DR), we need to keep the polarization of the electrons which are pulled from the source with polarization. For this reason, we have chosen the energy[6] where the spin tune polarization is at peak, as shown for the Stanford Positron Electron Asymmetric Rings (SPEAR) collider in Figure 7.7.

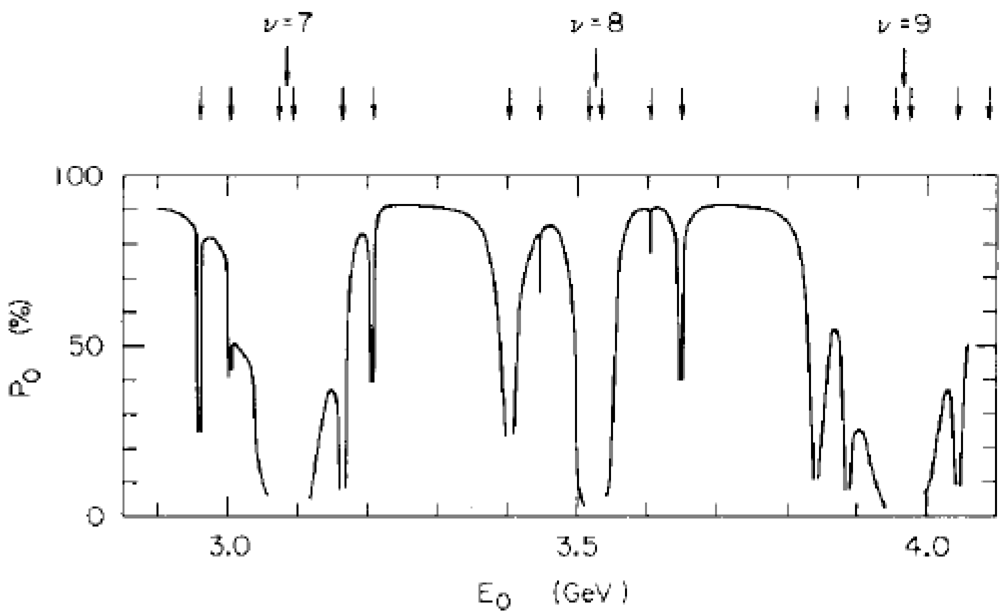

Figure 7.7. The spin polarisation calculation of SPEAR [71].

Figure 7.7 shows the energy of the ring versus the polarisation of the beam. One can notice that the polarization has minima for the integer values of ν=0.44 GeV, and reaches maxima for the half integer. For the FCC-e^+e^- DR, we have chosen ν=3.5 resulting in an energy of 1.54 GeV.

[6]Actually, the polarization is about the magnetic field, yet the magnetic rigidity in a damping ring is constant, therefore energy is directly linked to the magnetic field.

7.5. Damping Ring Optics and Performance

Putting together the two arcs and 2 straight sections each consist of two dispersion suppressors, the DR has become as demonstrated in Figure 7.8. The general parameters of the DR are listed in Table 7.1.

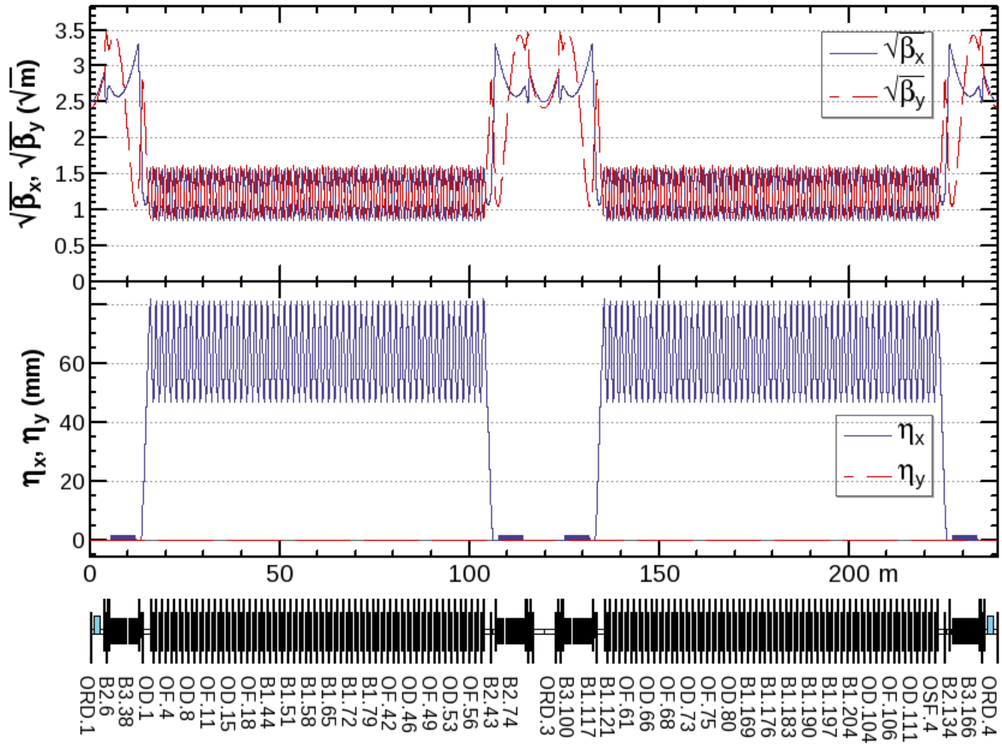

Figure 7.8. Damping ring optics.

Another crucial parameter of a ring is the betatron phase, as discussed in Section 2.7. In order to stay away from the resonances, we have chosen a safe working point: 24.19/23.58 radian horizontal and vertical betatron tunes, respectively. One can see that neither individually, nor their difference or sum are not close to an integer. Actually, in a typical synchrotron we expect a betatron phase shift below ± 0.05 rad which may arise due to any of the collective effects [72]. For this reason, a dynamic aperture survey has been carried out in ± 0.05 rad vicinity of both horizontal and vertical betatron tunes. A safely large island in the resonances plot has been assured.

Table 7.1. 1.54 GeV damping ring generic parameters.

parameter	value
circumference	241.8 m
no. trains, bunches/train	8, 2
train, and bunch spacings	51 ns, 50 ns
train store time	40 ms
energy loss per turn	0.225 MeV
RF voltage, frequency	4 MV, 400 MHz
no. of cells in an arc, cell length	57, 1.54 m
FODO cell phase advance (x, y)	69.5/66.1 deg
betatron tune (x, y)	24.19/23.58 rad
momentum compaction α_p	1.5 $\times 10^{-3}$

In ideal case, the equilibrium emittance was 0.96 nm in horizontal axis and practically zero in vertical axis recalling the quantum excitation in Subsection 2.6.1 to grasp ribbon like beam. Moreover, the rms bunch length was 2.1 mm for 3.5 nC bunch charge, and we had better include the intra-beam scattering (IBS) to simulate real like machine. The impact of the IBS has changed the equilibrium emittance to 2.3/0.23 nm (h/v). The bunch length has increased as well, namely to 2.3 mm. In order to overcome the effect of the IBS on horizontal axis, we have introduced $x-y$ coupling intentionally in order to distribute the blow due to the IBS into two planes [73]. The equilibrium emittance with the IBS together with the 20% coupling to overcome it have resulted in the parameters listed in Table 7.2.

The DR has 22.4 μm transverse and 14.7 mm longitudinal acceptances, as tabulated in Table 7.3. Therefore, 17σ transverse and 189σ longitudinal acceptances have been granted. Therefore, safe injection can be achieved and the tracking with the beam presented in Figure 6.5 (also in Table 6.1) has demonstrated satisfying results. Even though the beam was longitudinally mismatched, the longitudinal emittance is also cooled to a value close to the machine's longitudinal equilibrium emittance. Indeed, we have seen a filamentation due to mismatch in longitudinal plane as presented in

Table 7.2. 1.54 GeV damping ring equilibrium beam parameters with IBS and 20% $x - y$ coupling.

parameter	value
natural emittance (x, y, z)	1.39 nm, 0.28 nm, 1.75 μm
damping time (τ_x, τ_y, τ_z)	10.6/11.0/5.6 ms
bending radius, wiggler field	7.75 m, 1.8 T
acceptance (x, y, z)	22.4 μm, 22.4 μm, 14.7 mm
energy spread	7.74×10^{-4}
bucket height	8.0 %
energy acceptance	$\pm$7.8 %
injected emittance (x, y, z)	1.29, 1.22, 75.5 μm
extracted emittance (x, y, z)	1.81 nm, 0.37 nm, 1.52 μm

Figure 7.9. However, thanks to 7 damping times (i.e. store time divided by the longitudinal damping time), the filamentation is cured at the end of 40 ms, as shown in Figure 7.10.

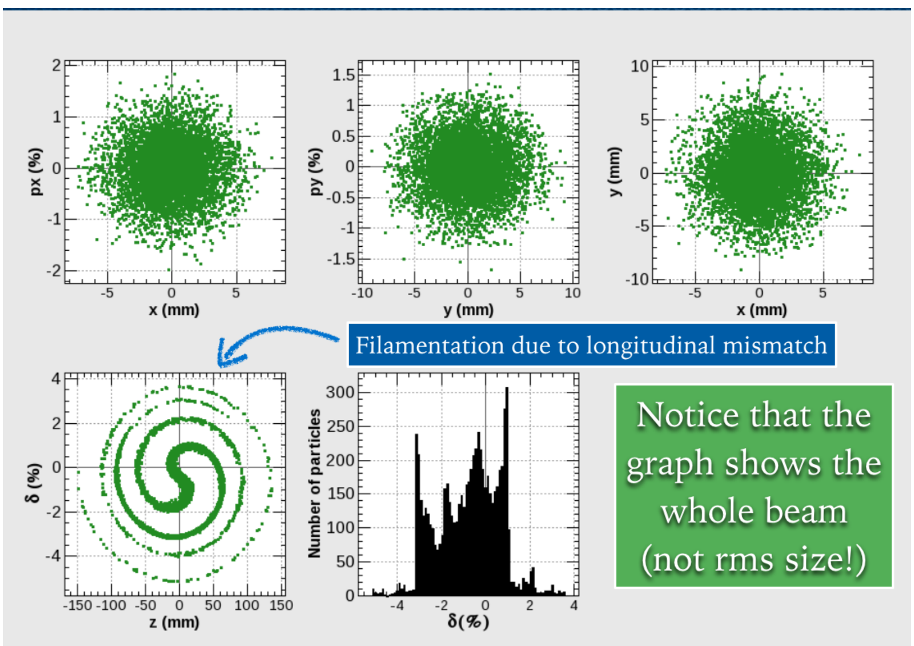

Figure 7.9. DR beam profile after tracking the positrons for 1000 turns with synchrotron radiation cooling.

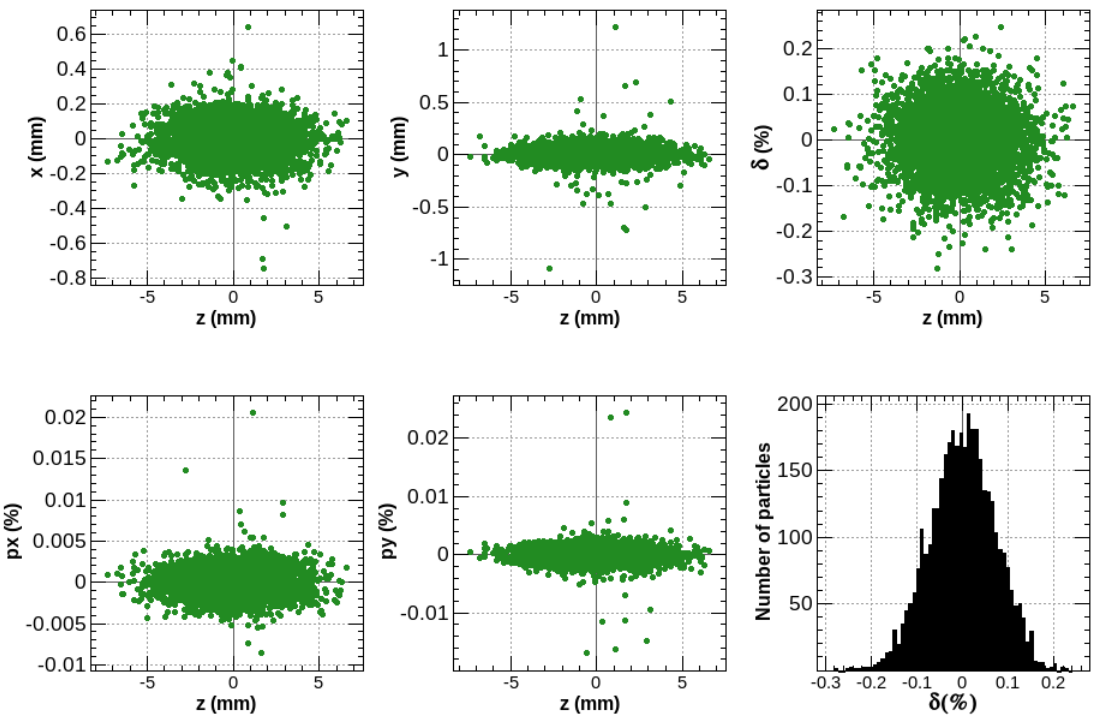

Figure 7.10. DR beam profile after positron beam tracking for 40 ms, i.e. 49593 turns with synchrotron radiation cooling.

Table 7.3. DR performance in tracking positron beam for 40 ms.

parameter	value
injected emittance (x, y, z)	1.29, 1.22, 75.5 μm
natural emittance of the ring (x, y, z)	1.39 nm, 0.28 nm, 1.75 μm
extracted emittance (x, y, z)	1.62 nm, 0.99 nm, 1.47 μm
injected bunch length (σ_z)	3.4 mm
extracted bunch length (σ_z)	2.1 mm

Design of a ring is a progressive work, to be more specific, requires foreseeing the impact of each action and return back to overcome. To illustrate, 4 MV cavity voltage has led to very large momentum spread acceptance, however the equilibrium bunch length become about 2.1 mm. Recalling the impact of the coherent synchrotron radiation (see Section 3.3), we may need to reduce the cavity voltage which will relaxes the bunch to longitudinally spread. However, the bucket height of the seperatrix will get diminished proportionally. Therefore, we may need to decrease the cavity voltage to 2 MV so that the rms bunch length of the beam elongates to approximately 5 mm. Furthermore, CSR may also be suppressed by the beam pipe if it is narrow enough to avoid superposition of emitted radiation. This time, the small beam pipe will tend to free more secondary particles stemmed from the radiated particles from the primary beam. This will create *electron cloud* which will decrease the beam transmission in the ring. To date, the electron cloud study for the FCC-e^+e^- is ongoing for Φ =30 mm round beam pipe [74]. Therefore, the beam pipe radius is 15 mm, which matters for the field calculation of the magnets. Since the DR is totally normal-conducting except the cavities, quadrupole strength which should be less than 0.8 Tesla to stay NC. All quadrupoles in the DR are with less than 0.6 T magnetic field for 15 mm radius beam pipe. Actually, this optimization was to leave safety margin if the beam pipe radius would have been chosen to be 20 mm which corresponds to 0.8 T magnetic field in the quads. Apart from this, the sextupoles, which all are 8 cm long, will have 0.3 T and the main dipoles (i.e. those deployed in the arc) will produce 0.66 T to circulate the beam in the ring.

The beam pipe material selection matters the vacuum as well as instabilities experts. For instance, resistive wall instability may arise if the conductivity of the beam pipe is not sufficient. Also, the beam pipe inner coating needed to reach higher vacuum, for instance coating with non-evaporable getter, would have also change the conductivity. However, the beam pipe radius has more fundamental limiting impact for the optics design, which is the beam loss. The radial aperture of 15 mm is applied in the arcs and straight sections of the DR, meaning that the any particle exceeding this limit will be counted as loss. Consequently, the transmission of the DR for 40 ms tracking is 57% whereas it is 98% if the 15 mm radius beam pipe constraint is only applied in the straight sections. To sum up, the beam pipe size needs to be larger in the arc, since $x = x_\beta + \eta\delta$ (Equation 2.55), thereby the positron beam injected has δ_{total}=±5% the beam size is very large in the arcs. The beam pipe study is still ongoing iteratively together with misalignment and instability studies in the DR.

8. BEAM-BASED STUDIES AT SuperKEKB

SuperKEKB is the flagship experiment carried out at the High Energy Accelerator Research Organization (KEK) in Japan. Being the successor of KEK B-meson factory (KEKB) which held the world luminosity record, SuperKEKB aims to reach 40 times more luminosity, i.e. 80×10^{34} cm^{-2}s^{-1}. The double-ring asymmetric energy collider seeks physics beyond the Standard Model of particles. The SuperKEKB makes use of the old KEKB accelerators with improvements on the injector linac and further suppression of β functions at the interaction point (IP) where the Belle II detector stands. The layout of the SuperKEKB collider is presented in Figure 8.1.

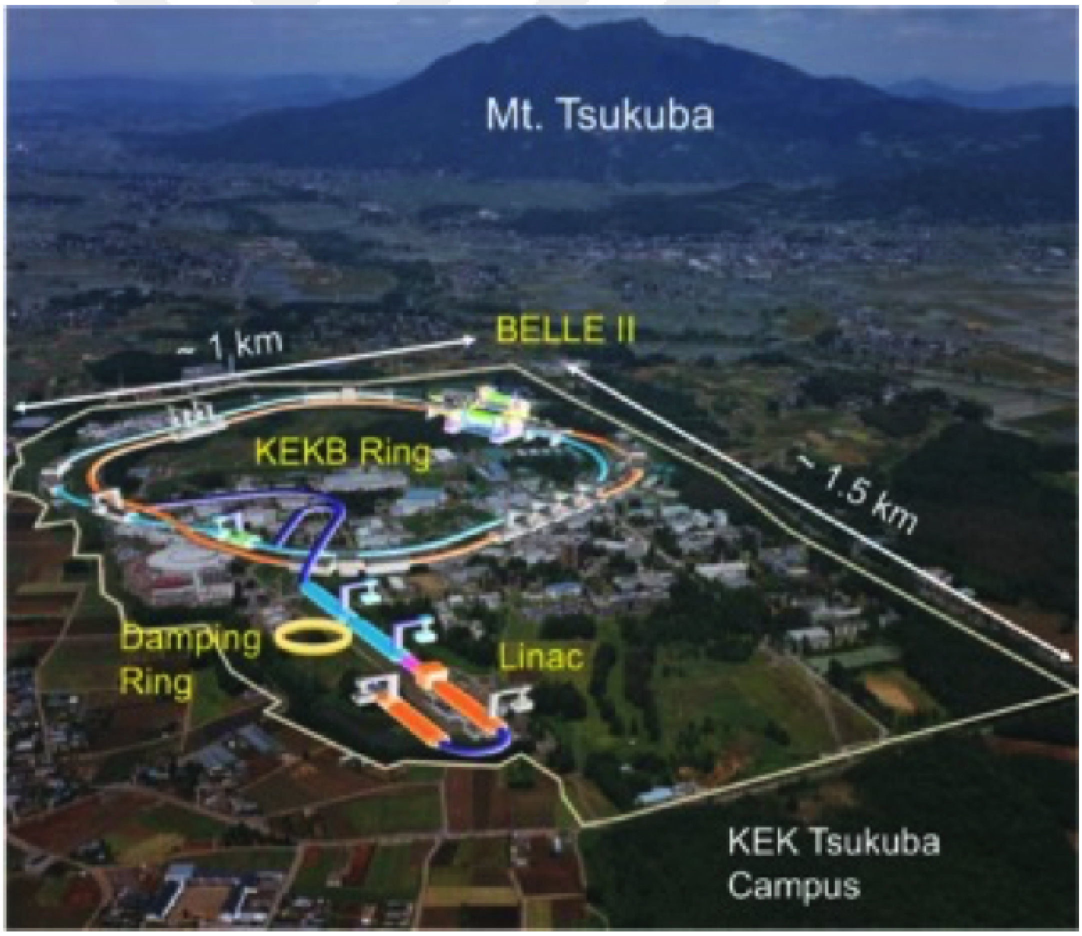

Figure 8.1. SuperKEKB layout. The J-shaped linac has a branching point for the positron damping ring. The injector linac provides e$^-$ and e$^+$ beam with asymmetric bunch charge and energy to the collider with two rings.

The SuperKEKB collider has two rings: one for the electron beam called high energy ring (HER) and another for the positron ring at 4 GeV called low energy ring (LER).

In this chapter, we describe two main studies carried out at SuperKEKB injector linac, the first study was 'Beam-based Misalignment Determination of Quadrupoles', which is described in Section 8.1-8.3, the same as it is published [75].

8.1. Beam-based Misalignment Determination of Quadrupoles

The advance from KEKB to SuperKEKB has also required an upgrade of the injector. The SuperKEKB injector includes two different electron sources, namely an RF-gun producing a low emittance electron beam, for injection into the SuperKEKB electron ring, and a thermionic gun, generating high-intensity electron bunches for positron production. Following these sources, the SuperKEKB S-band injector linac is about 648 m long. It is alternatively used for the acceleration of electrons and positrons. Positrons are created by intercepting 10 nC electron bunches with a production target. The positron target is located 275 meter downstream of the electron sources, corresponding to an electron beam energy of 3.3 GeV. Positrons emerging from this target are captured and accelerated to 1.1 GeV, in the first portion of the same linac, before they are injected into a damping ring. The primary operational challenge is to keep the positron charge at around 4 nC during capture and acceleration. In order to achieve a high positron transmission, focusing magnets are installed around the accelerating cavities, in addition to steering magnets and BPMs. Table 8.1 compiles a few key parameters of the SuperKEKB injector linac [76, 77].

In daily operation, the performance of the SuperKEKB linac has been maintained by brute force scanning of both orbit and focusing strengths for optimum transmission, using all the steerers, quadrupoles and BPMs available. This optimization, however, is complicated by the fact that the changes applied are typically not orthogonal. For example, changing a quadrupole strength will affect the beam orbit if the beam is not centered in the quadrupole. For this reason, we developed an alternative beam-based

Table 8.1. SuperKEKB linac parameters

Parameters	electrons	positrons
beam energy [GeV]	7	4
bunch charge [nC]	5	4 (10*)
normalized vertical emittance [μm]	20	20
normalized horizontal emittance [μm]	50	100
rms bunch length [mm]	1.3	0.7
energy spread [%]	0.08	0.07
number of bunches/pulse	2	
bunch spacing [ns]	96	
max. linac repetition [Hz]	50	
operating Frequency [MHz]	2856	

* Primary electron beam sent to the target to achieve 4 nC of positrons.

determination of the quadrupole centers and an associated steering algorithm.

The term ‘beam-based alignment’ refers to a group of widely-used techniques to determine the magnetic centre of quadrupole and sextupole magnets with respect to nearby BPMs using beam information [78–80]. The misalignments of a set of quadrupoles with respect to the beam is often determined with the help of response matrices. Such response matrices require an accurate optics model, including information on the local beam energy, which is not easily available in a linac, where reference RF phases tend to drift in time.

For our method, instead, we directly determine the magnetic centre (‘zero kick’ position) for each individual quadrupole, and avoid the use of any response matrix element R_{12}. The error in our method is mainly due to ‘beam jitter’, i.e. pulse-to-pulse fluctuations in the beam trajectory, and due to slow drifts in the alignment, electronics or change in RF parameters etc. It is independent of beam energy and optics model. Considering sets of three BPMs, the correlation between the BPMs varies during a measurement. Yet the variation stays below 1 μm, a value which we identify with the

BPM measurement error.

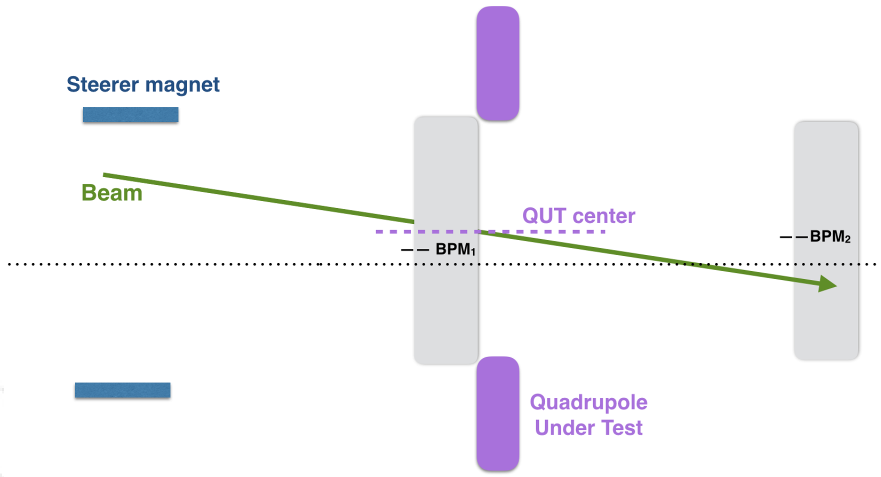

Figure 8.2. QuadBPM is a simple operation performed by varying the strengths of upstream steerer magnets and quadrupoles until the highest current transmission is achieved in the downstream BPM(s). The dotted line represents the accelerator reference orbit.

So far, during regular SuperKEKB linac operations, a so-called 'QuadBPM' method [81] has been performed. Here, the transverse position of a beam inside a quadrupole is optimized so that the transmission recorded by a downstream BPM is maximum, as is illustrated in Figure 8.2. However, steering the beam in this way may make the beam enter the downstream accelerating structures at a nonzero angle, and thereby expose the beam to strong linac wakefields, resulting in a banana shape bunch [43]. In consequence, the beam may suffer from emittance dilution and even experience beam break-up instability.

The aim of the present study is to develop an approach alternative to the QuadBPM method. More precisely, our goal is to first determine the quadrupole alignment errors and to then steer the beam through the quadrupole centres accordingly. Under the plausible assumption that quadrupoles and nearby accelerating structures are closely aligned with each other, this steering should also approximately center the beam inside these structures. As a consequence of wake-field minimization, it should help preserve the normalized emittance.

Hence, the proposed steering method should be useful in long linacs operating with low-emittance beams, such as for X-ray Free Electron Lasers or the FCC-e^+e^- [2, 5], CLIC [82] and ILC [83].

In a proof-of-principle experiment we have applied our method to the first 12 meters of positron capture section, where beam loss is particularly critical. The electron beam was used for the beam-based measurements instead of the positron beam, since it is smaller in size both transversely and longitudinally; it also has a higher energy in this region, and, therefore, is less affected by the wakefields. The optics of the electron beam after the positron target is presented in Figure 8.3. The electron beam parameters at the time of our measurement are listed in Table 8.2. The tabulated values are measured just before the positron target where the last diagnostics station is located. Downstream of this point the beam energy increases, by about 300 MeV over 10 m, since all the cavities are active, while the charge decreases since all quadrupoles, except for the one under test, are turned off in the region of interest corresponding to Figure 8.4.

Figure 8.4 shows the positron optics in the region of interest. Two successive 2 meter long S-band cavities are surrounded by 3 quadrupoles each; one more quadrupole is installed between the cavities. In other words, there are 7 quadrupoles without BPM located between two quadrupoles equipped with a BPM. These 7 quadrupoles can be seen in between the BPM_1 and BPM_2 which are marked by arrows. A third BPM, BPM_3, is also marked, and it is used for Q5 (i.e. the quadrupole located just after BPM_2). These 3 BPMs are also used for self-correlation studies to analyze and quantify measurement errors. This particular region was selected to illustrate the usefulness of the method even in a challenging accelerator zone.

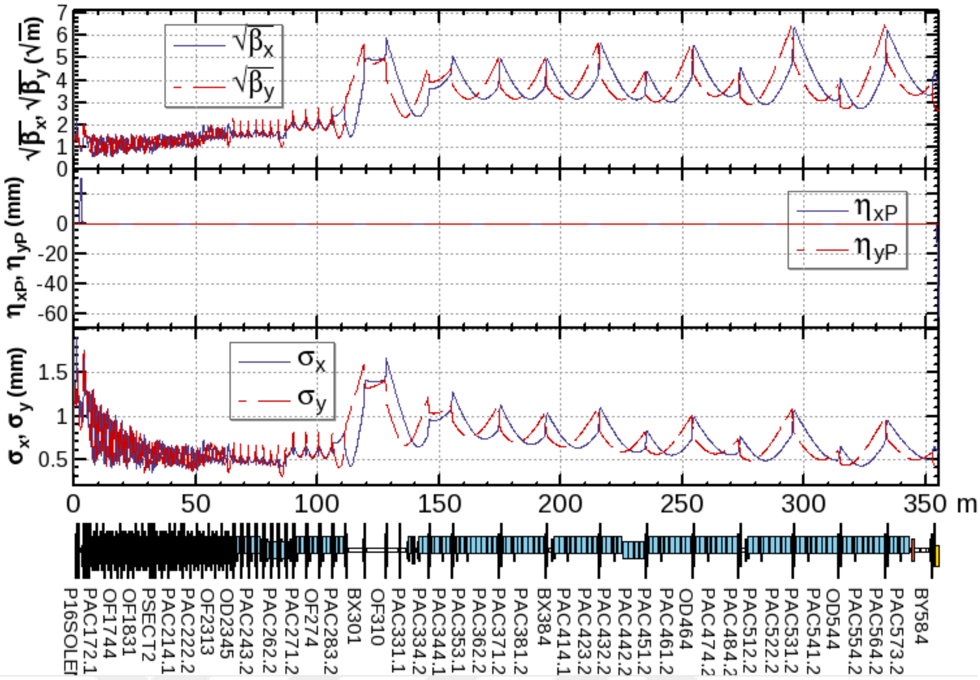

Figure 8.3. SuperKEKB electron optics starting from the positron target with an electron beam energy of ranging from 3.2 to 7.0 GeV. Square-root of β-functions (top), design dispersion function in normalised coordinates (centre) and rms beam sizes (bottom) as a function of longitudinal position along the accelerator.

Table 8.2. SuperKEKB linac parameters used during the measurements presented in this paper.

Parameters	value
beam energy	> 2.98 GeV
normalized horizontal/vertical emittance ($\gamma\epsilon$)	90 μm
horizontal/vertical beam size	0.5 mm
bunch length (σ_z)	1.3 mm
bunch charge	< 1.2 nC
linac repetition	5 Hz
horizontal jitter (rms)	62 μm
vertical jitter (rms)	104 μm

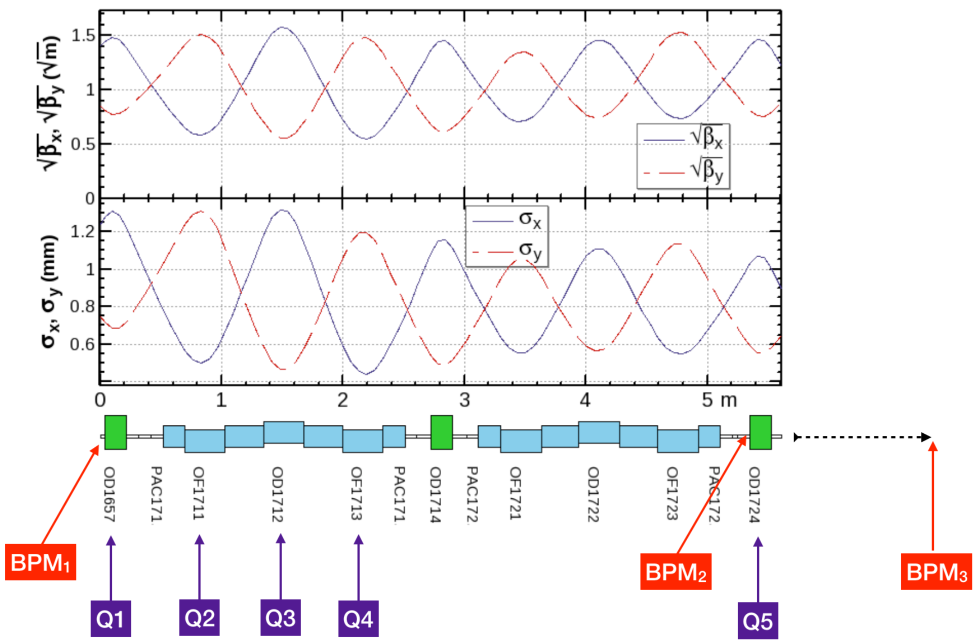

Figure 8.4. SuperKEKB electron beam optics for 3.34 GeV to 3.39 GeV. Upper graph demonstrates the square-root of the β-function, and its beneath, the transverse beam sizes are plotted.

A misaligned quadrupole deflects the beam centroid in the same way as a dipole magnet. Thanks to this deflection, the misalignment of the quadrupole can be determined [84]. The offset dx of a quadrupole relative to the beam with transfer matrix element R_{12} between the quadrupole with an effective length l_Q and a downstream BPM can be determined by changing the quad's integrated gradient $B'l_Q$, and recording the orbit change Δx of the beam,

$$\Delta x = -R_{12}\frac{B'l_Q}{B\rho}dx \; , \tag{8.1}$$

where $B\rho$ denotes the magnetic rigidity. From this equation we can deduce the quadrupole shunt technique [85], which consists in changing the quadrupole strength and recording the varying deflections due to misaligned quadrupole. This simplest method, however, is not applicable at the SuperKEKB linac due to the absence of a local energy measurement (magnetic rigidity). Instead, we utilize the fact that a quadrupole does not deflect the beam at all if the beam passes through its center. For storage rings, this fact is the basis of the quadrupole alignment using tune modulation, developed at LEP [86].

We determine the *zero kick position* for the quadrupoles with BPM, which directly yields their misalignments with respect to their own BPMs, or more precisely the offset of the BPM with respect to the quadrupole magnetic center. Indeed, we are utilizing Equation (8.1), where Δx is recorded by the BPM_2 and changes in dx by BPM_1. BPM_2 is located about 5 m away from BPM_1 and the two cavities between the BPMs are active.

Determining the misalignment of two quadrupoles with respect to their own BPMs is the first and most crucial step to determine the reference orbit. So-called *virtual BPMs* are then assigned to the intermediate quadrupoles, those without any physical BPMs which are located in between the two aforementioned quadrupoles. The position reading for these virtual BPMs is obtained, after switching off all the intermediate quadrupoles, by fitting a straight line between the two real BPMs, ignoring any possible effect of acceleration, which is small for the high-energy electron beam. The intermediate quadrupoles are then turned on, one alone at a time, to measure the deflections generated, and to find the misalignment with respect to the virtual BPM.

Prior to executing the complete misalignment study, we examine the correlation of the BPM readings for an example data set.

8.1.1. Correlation of BPM Readings

While it is independent of BPM offsets, the alignment method requires the BPM readings to be precise and mutually consistent. In order to check this consistency, we have examined the correlation between three successive BPMs. Including a possible offset (c_0), we expect the BPM readings to be linearly related as

$$c_1 \times BPM_1 + c_2 \times BPM_2 = BPM_3 + c_0 \;, \tag{8.2}$$

where c_0, c_1 and c_2 are coefficients, which can be calculated from the data using the least-squares method or, perhaps better, the "eigenfit" technique [87].

We examine the BPM correlation for each data acquisition period. An outstanding correlation between the 3 BPMs has been observed, as shown in Figure 8.5. For three BPMs the discrepancy (offset) is c_0=0.4 μm, which is small compared with the BPM resolution of 1 μm, and the correlation exceeds 99.9%.

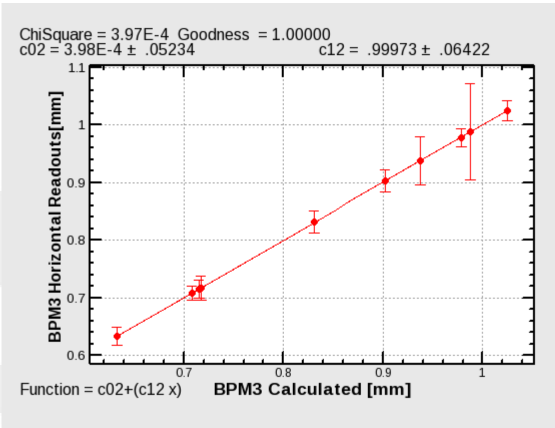

Figure 8.5. Measured BPM_3 reading versus the BPM_3 value predicted from the other two BPMs according to Equation (8.2).

8.1.2. Alignment of Quadrupoles with respect to their own BPMs

The method is easy and straightforward to deploy, as depicted in Figure 8.6. Determining the alignment of the Quadrupole Under Test (QUT) requires at least two BPMs, one located just in front, or attached to, and another one downstream of the QUT, which are called BPM_1 and BPM_2, respectively. In addition, a third downstream BPM, called BPM_3, is also used to cross-check transmission and dipolar kick, as well as to study downstream quadrupoles; this additional BPM is not shown in the figure. All other quadrupoles between BPM_1 and BPM_2 need to be turned off, so that the misalignment determination can be made with highest precision, and the associated error is not affected by other alignment errors.

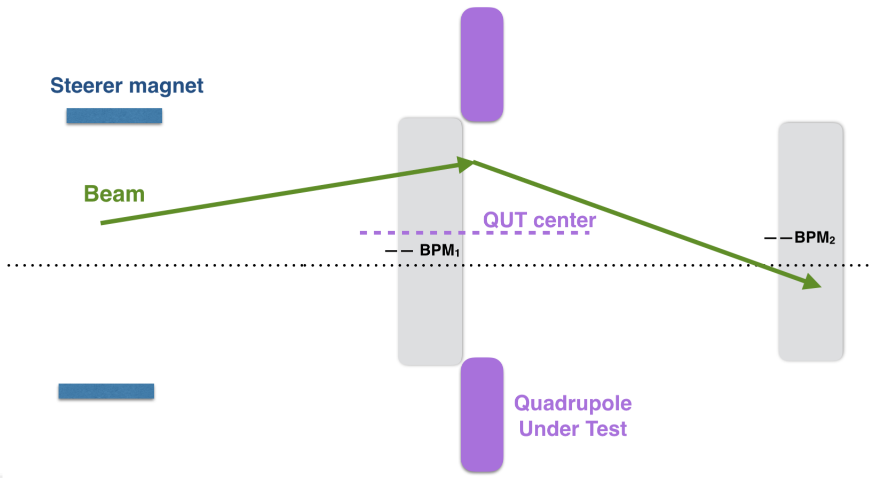

Figure 8.6. A sketch of the orbit change caused by the dipolar kick from a displaced quadrupole.

8.1.3. Horizontal magnetic center of Q1

The interface presented in Figure 8.7 is taken from the GUI of SAD [16]. The procedure applied is as follows:

- The steerer magnet is set to a value at which the beam transmission through all the BPMs is almost constant; otherwise the BPM readout would be shifted due to beam loss and not purely reflect the effect of the QUT's dipolar kick. To ensure good data quality, we also require that changes on the quadrupole gradient are not accompanied by noticeable changes in the readouts of BPM$_1$ located upstream.
- Indeed the incident position at BPM$_1$ needs to be almost constant. Small fluctuations seen in Figure 8.7 are due to the natural pulse-by-pulse beam jitter. The errorbars on both BPMs are calculated by taking the same measurement 20 times at fixed QUT strength. From these measurements standard deviations are computed.
- The QUT gradient should be changed within a strength interval in which no significant beam loss occurs at the reference BPMs. Also, for each gradient change of QUT, we waited 10 seconds before starting the data acquisition to make sure

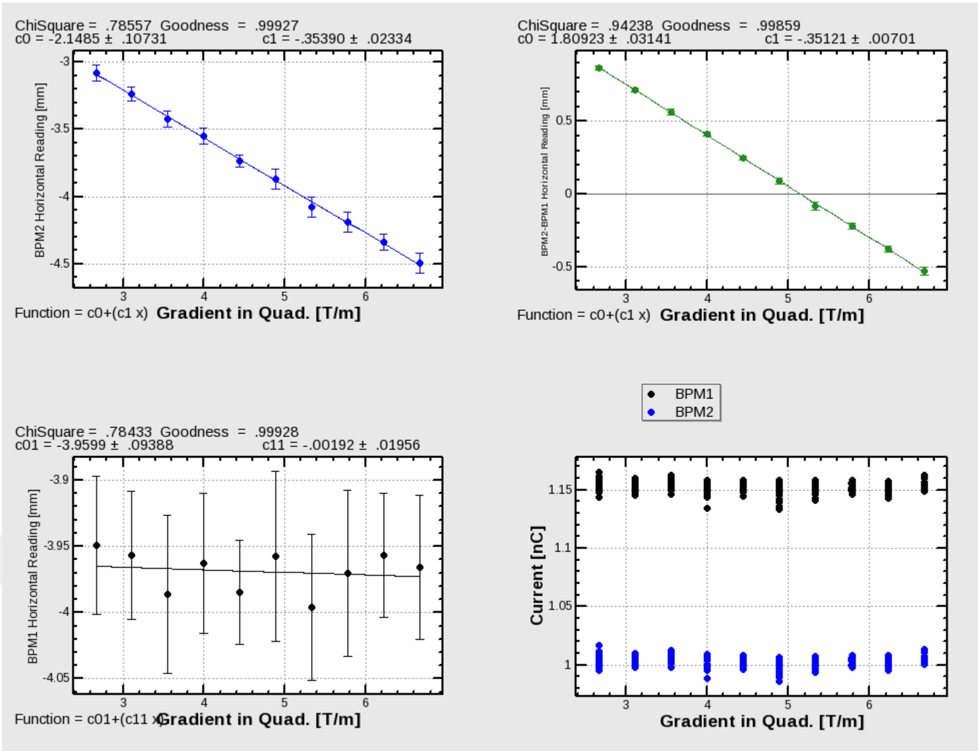

Figure 8.7. The horizontal corrector is set to BX135=−0.45 A, and the beam is almost stable on BPM_1 (left bottom graph), but the quadrupole under study(QUT) kicked the beam with a certain slope on BPM_2 (left top graph). To eliminate the impact of beam jitter, another linear fit looks at the difference of BPM_2 and BPM_1 readouts (right top graph); the beam current is almost constant with varying quadrupole gradient (right bottom graph).

that the magnetic field was stabilized.

- Next the beam is steered to another initial position at BPM_1 using upstream steerer magnets and the above steps are repeated, as is illustrated in Figs. A.1, A.2, A.3, and A.4.
- The data to be collected and analyzed are the positions at BPM_1 and BPM_2. We can plot either the BPM_2 data or the difference of BPM_2 and BPM_1 versus the BPM_1 reading. Utilizing these data, we can determine the position with zero slope and declare this to be the misalignment of QUT with respect to BPM_1. This information can later be used for steering the linac so that the beam passes through the magnetic center of the QUT.

- We can also plot BPM_2 data versus the steerer magnet current, as is presented in Figure 8.8.

Evidently, the steerer magnet should drive the beam in the direction of the intended measurement. For instance, a horizontal steerer can be used only for the horizontal misalignment determination. We assume that the region under study contains no solenoids or skew quadrupoles or any other source of $x - y$ coupling.

From Figure A.1 to A.3, the slopes calculated are decreasing together with the steering-corrector current. Continuing to decrease the corrector current we should cross the quadrupole center, where the beam orbit on all BPMs should stay constant while the QUT gradient varies. Actually, already from the change in the slope we can deduce BPM position corresponding to the quadrupole center.

The possible error due the beam jitter seen in Figure A.3 is largely suppressed by taking weighted averages of the slopes. If we plot all of the slopes calculated in Figs. A.1, A.2, A.3, and A.4 including their errors as a function of the change in the corrector current, or incident position at BPM_1, we can obtain the corrector setting (or position) where this slope is zero. This corresponds to the magnetic center of the QUT with respect to BPM_1, as sketched in Figure 8.8. We notice, in the example, that the QUT's horizontal magnetic center is passed when the corrector current varies between -0.1 A and 0 A, where the slope changes sign (see Figs. A.3 and A.4). Therefore, the horizontal misalignment of QUT (Q1) is found to be -0.502 ± 0.015 mm with respect to (w.r.t.) BPM_1. This point -0.5 mm at BPM_1 is indeed reached for a steerer current between -0.1 A and 0 A, as shown in the right picture of Figure 8.8.

8.1.4. Confirmation of the magnetic center of Q1

Actually, we can test whether the calculated value -0.502 ± 0.015 mm on BPM_1 indeed corresponds to the horizontal magnetic center of the Q1 or not. The procedure is simple: We just need to send the beam to around -0.5 mm at BPM_1, as we did in Fig 8.9.

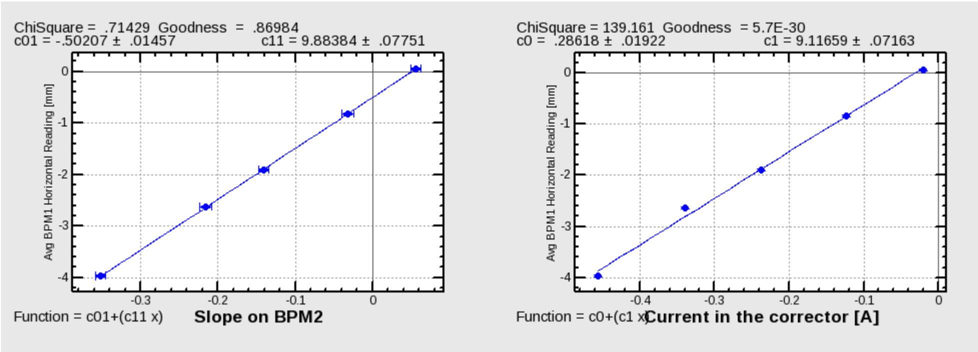

Figure 8.8. The misalignment of the Q1 is -0.502 ± 0.015 mm with respect to (w.r.t.) BPM_1 where the slope is zero on BPM_2 (left graph).

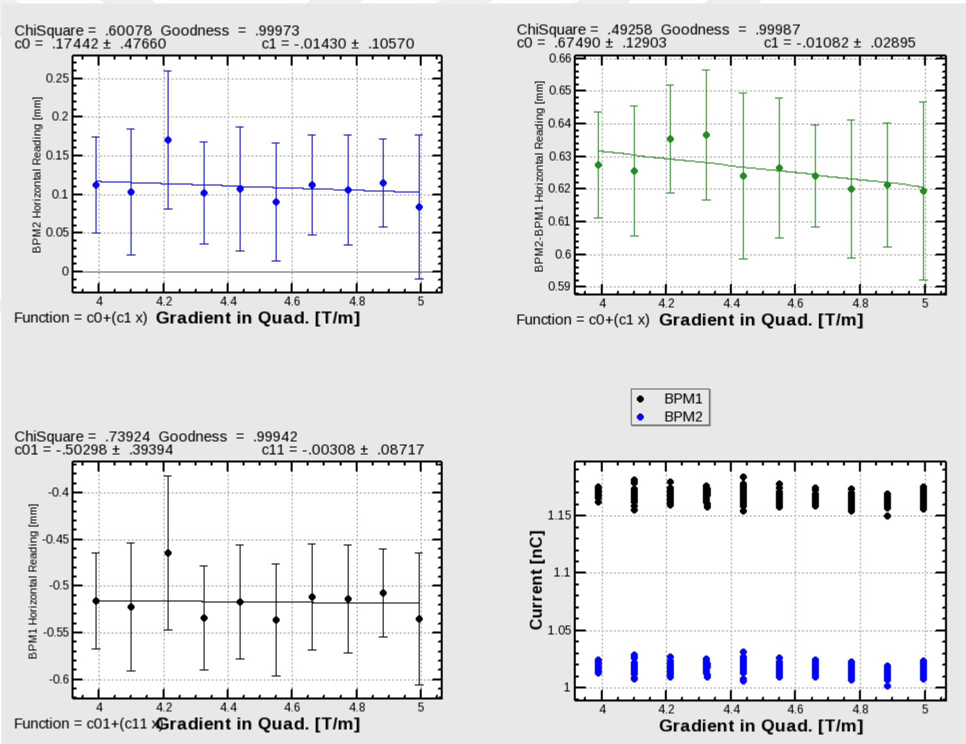

Figure 8.9. The beam is steered to the calculated center of quadrupole Q1 w.r.t. BPM_1. The beam almost does not move with changing strength of Q1 which means the beam is passing through the magnetic center of the quadrupole or close to it.

8.1.5. Vertical magnetic center of Q1

A procedure quite similar to the one in Subsection 8.1.3, can be applied in the vertical plane as well. Fortunately, since the beam line between the horizontal steerer

BX135 and the quadrupole Q1 contains a solenoid, we are able to use the exactly same data for the vertical alignment of Q1 w.r.t. BPM_1. The vertical misalignment calculated is 0.195 ± 0.037 mm, as is shown in Figure 8.10.

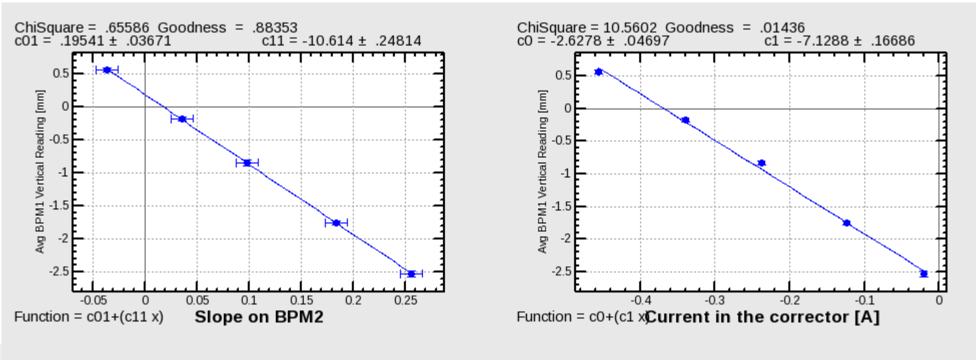

Figure 8.10. Vertical alignment of Q1.

8.1.6. Horizontal magnetic center of Q5

We proceeded to apply the same method to Q5 which contains the BPM_2 in its bore (see Figure 8.4). Instead of BPM_1 and BPM_2, now the BPM_2 and BPM_3 are utilised since now these two are the front and rear BPMs with respect to Q5.

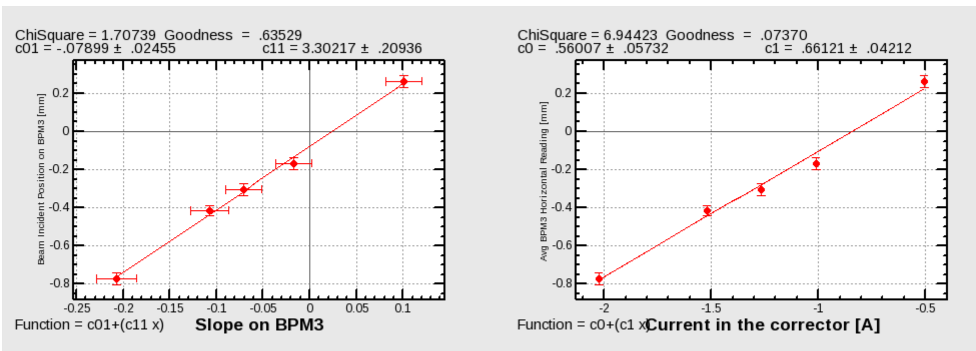

Figure 8.11. Horizontal alignment of Q5 (left), and the current of the steerer leading to the corresponding BPM_2 readouts (right).

The horizontal displacement of Q5 is calculated to be -0.079 ± 0.025 mm, at which point the slope on BPM_3 is zero, as can be deduced from Figure 8.11.

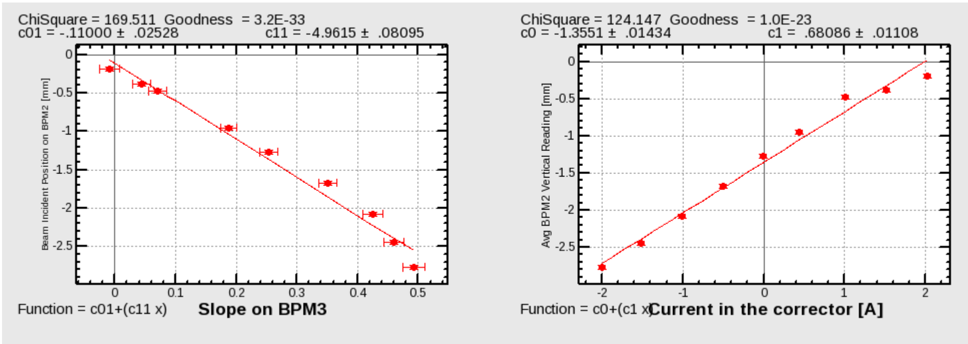

Figure 8.12. Vertical alignment data for Q5 (left), and the current of the steerer leading to the corresponding BPM_2 readouts (right).

8.1.7. Vertical magnetic center of Q5

Our alignment procedure seems to work as intended. This leaves the issue of its eventual optimization. Namely, the question arises that how many (and which) slope points are needed to converge to the minimum standard deviation for the misalignment value. We were able to check this question with Q5, since we had a horizontal and a vertical steerer, respectively, in the vicinity, enabling us to steer the beam over a wide range of incident positions on BPM_2 without significant transmission loss. This allowed us to acquire more data points as presented in Figure 8.12. The calculated alignment turns out to be -0.110 ± 0.025 mm. Hence we can conclude that the additional points do not necessarily decrease the standard deviation in the alignment determination. However, acquiring more than 20 measurements at fixed QUT strength would allow us to construct a reliable errorbar, which is enlisted as a future study.

8.2. Alignment of the quadrupoles without BPMs

The data taking procedure for quadrupoles without near-by BPMs is the same as for quadrupoles with BPM. Nonetheless, the absence of the attached BPM to a quadrupole compels us to revise our analysis a little. As depicted in Figure 8.13, the steerer can be located quite far away; in addition, there can be other accelerator elements between the references BPM_1 and BPM_2. Using the associated transfer matrices might introduce an error since no direct measurements of beam rigidity are available at the location of each quadrupole. Therefore, we focus on the region of interest, namely, the zone spanned by BPM_1 and BPM_2, and we turn off all quadrupoles located in between except for the QUT.

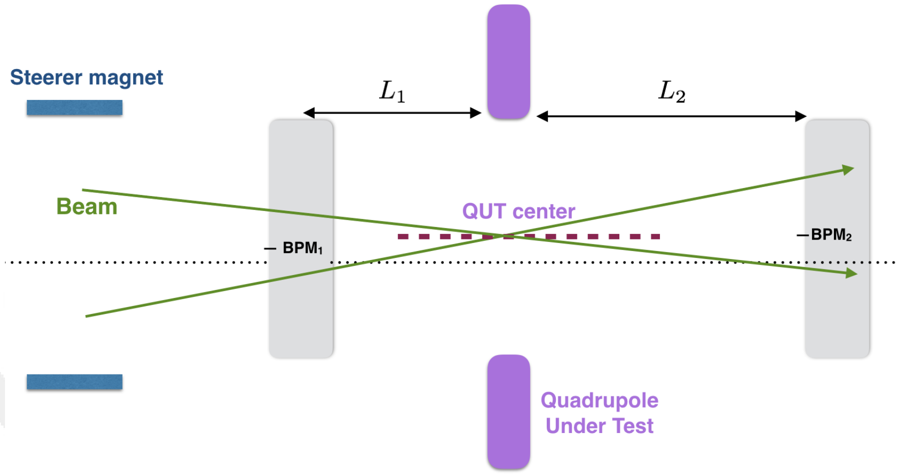

Figure 8.13. Two beam trajectories are shown as green continuous lines. The beam orbit is straight, as for the green lines, only when it passes through the magnetic center of the QUT (purple dashed line) or when the QUT is off. The dotted line shows an ideal reference line of the accelerator.

Next we create hypothetical BPM readouts. The beam moves on a straight line between BPM_1 and BPM_2 in the two cases when it either passes through the QUT centre (Figure 8.13) or when the QUT is off. Therefore, we can calculate a *virtual* BPM readout at the location of the QUT as follows:

$$\frac{BPM_1 \times L_1 + BPM_2^{QUT=0} \times L_2}{L_1 + L_2} = BPM_{virtual} \ , \tag{8.3}$$

where the BPM_1 and BPM_2 readouts are interpolated depending on their distances from the QUT, i.e. L_1 and L_2, respectively. $BPM_2^{QUT=0}$ is the BPM_2 readout for QUT at zero quadrupole current. This BPM reading $BPM_2^{QUT=0}$ can be obtained even without actually switching off the quadrupole: it corresponds to the vertical intercept at zero strength in the measurements of BPM_2 reading versus different QUT strengths; see, for instance, the top-left plot in Figure A.5. Again BPM_1 represents a weighted average of readouts. The error of the virtual BPM readout follows by propagating the errors of BPM_1 and BPM_2:

$$\sigma^2_{virtual} = \left(\frac{L_1}{L_1+L_2}\right)^2 \sigma^2_{BPM_1} + \left(\frac{L_2}{L_1+L_2}\right)^2 \sigma^2_{BPM_2^{QUT=0}} \ . \qquad (8.4)$$

The computed misalignment for the QUT is given with respect to the hypothetical straight line passing from BPM_1 to BPM_2, or in other words, with respect to its own virtual BPM.

However, we may also choose another line of reference for the misalignment of the QUT. For example, magnets in a region of interest, between Q1 and Q5, are actually situated on top of a girder. Therefore, we may want to physically align the intermediate quadrupoles with respect to these two outer quadrupoles centers. For this purpose we create another set of data consisting of (BPM_1 minus the Q1 misalignment) versus ($\mathrm{BPM}_2^{QUT=0}$ minus the Q5 misalignment) for the each direction of misalignment determination. Thus, the associated error with respect to the reference magnets would become:

$$\sigma^{magnets^2}_{virtual} = \left(\frac{L_1}{L_1+L_2}\right)^2 (\sigma^2_{BPM_1} + \sigma^2_{Q1}) + \left(\frac{L_2}{L_1+L_2}\right)^2 (\sigma^2_{BPM_2^{QUT=0}} + \sigma^2_{Q5}) \ , \qquad (8.5)$$

where σ_{Q1} denotes the error of the displacement value we found in Subsections 8.1.4 and 8.1.5, for the horizontal and vertical misalignment, respectively; similarly σ_{Q5} corresponds to the values we found in Subsections 8.1.6 and 8.1.7. Obviously, the horizontal study requires the corresponding horizontal error, the vertical study the vertical error.

8.2.1. Horizontal magnetic center of Q2

The misalignment of Q2 with respect to the straight line passing through BPM_1 and BPM_2, in other words, with respect to its own virtual BPM_{Q2} is -0.209 ± 0.029 mm. However, if this misalignment is determined with respect to the line passing though the magnetic centers of Q1 and Q5, it becomes -0.075 ± 0.032 mm in the horizontal plane.

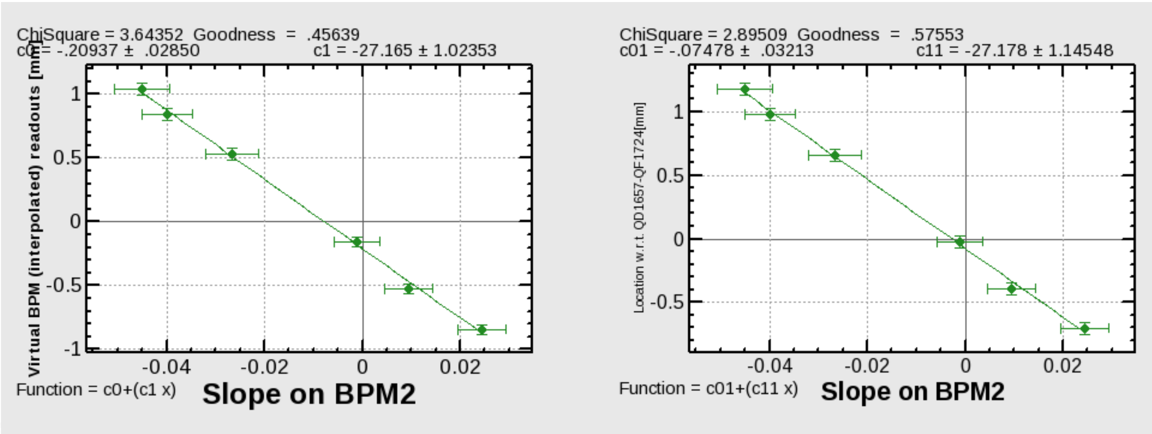

Figure 8.14. Horizontal misalignment of Q2, on the left with respect to its own virtual BPM_{Q2}, on the right with respect to the reference line defined by Q1 and Q5.

8.2.2. Vertical magnetic center of Q2

The vertical misalignment of Q2 with respect to its own virtual BPM_{Q2} is $-0.019{\pm}0.107$ mm. On the other hand, the misalignment determination with respect to the line defined by the magnetic centers of the Q1 and Q5 is $0.056{\pm}0.109$ mm. The larger error of this measurement is due to the stronger jitter in the vertical direction (see Table 8.2).

8.2.3. Horizontal magnetic center of Q3

This measurement has two data points with almost the same steerer current as can be seen in Figure 8.16. This is intentionally used in the fit to check that the similar measurements repeated later would correspond to the similar results. All in all, the calculated misalignment is $-0.419{\pm}0.031$ mm w.r.t. $\mathrm{BPM}_{Q3}^{virtual}$ and it is -0.232±0.034 mm w.r.t. the reference quadrupoles.

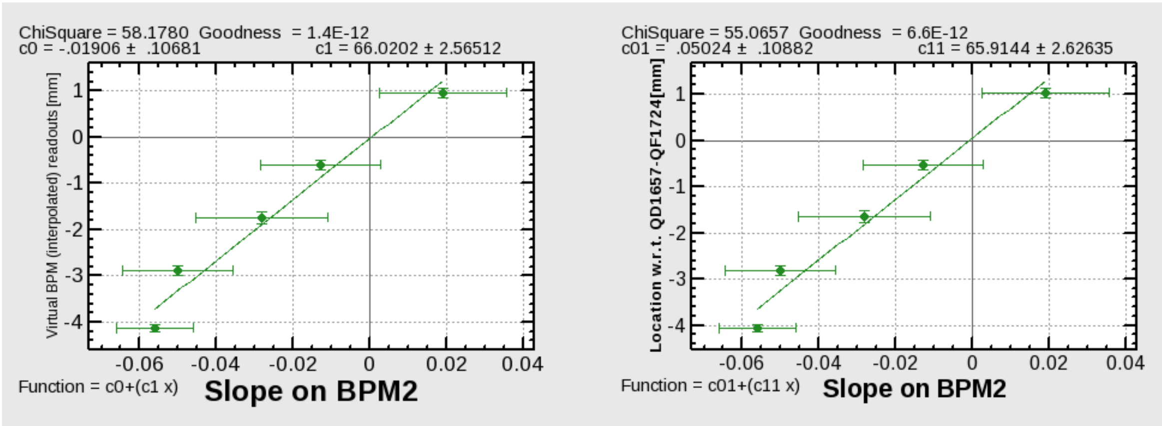

Figure 8.15. Vertical misalignment of Q2, on the left with respect to its own virtual BPM_{Q2}, on the right with respect to the reference line created by Q1 and Q5.

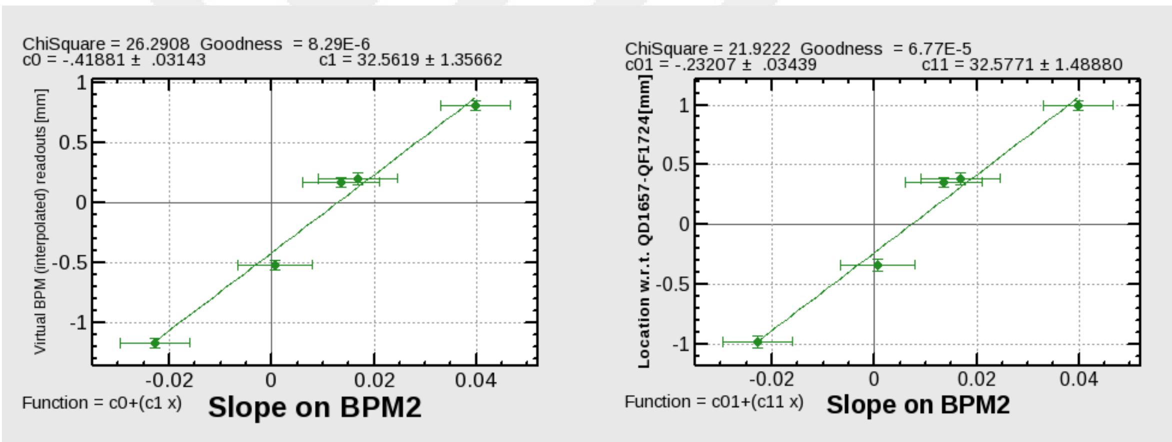

Figure 8.16. Horizontal misalignment of Q3, on left with respect to its own virtual BPM_{Q3}, on right, w.r.t. the reference line defined by Q1 and Q5.

8.2.4. Vertical magnetic center of Q3

The calculated misalignment is -0.173 ± 0.079 mm w.r.t. $\mathrm{BPM}_{Q3}^{virtual}$ and it is $-0.141\pm$ 0.082 mm w.r.t. reference quadrupoles, as presented in Figure 8.17.

8.2.5. Horizontal magnetic center of Q4

This measurement has an almost same steerer current data point, as presented in Figure 8.18. This is intentionally kept to check that the similar measurements repeated

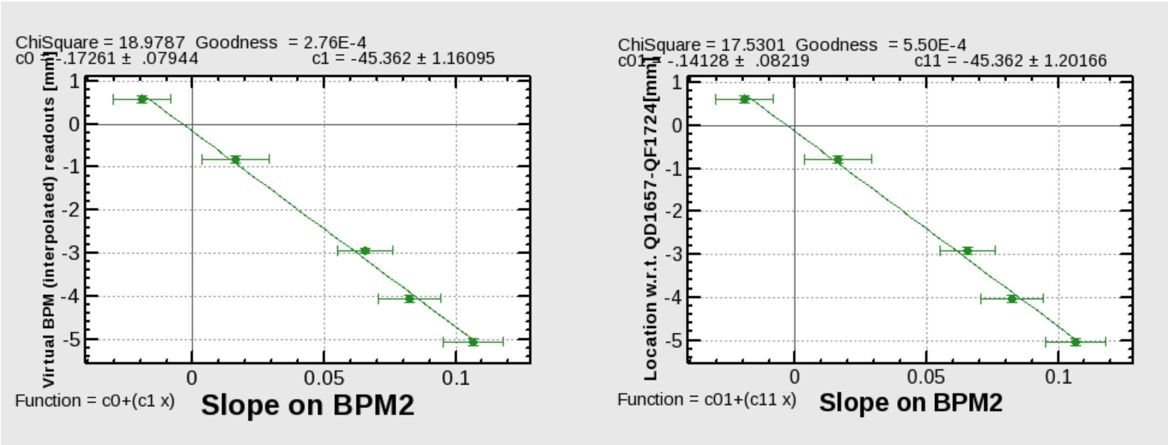

Figure 8.17. Vertical misalignment of Q3, on left w.r.t. BPM$_{Q3}^{virtual}$, on right, with respect to the reference line defined by Q1 and Q5.

later would correspond to the similar results. All in all, the calculated misalignment is -0.555 ± 0.023 mm w.r.t. BPM$_{Q4}^{virtual}$ and it is $-0.316 \pm$ 0.026 mm w.r.t. reference quadrupoles.

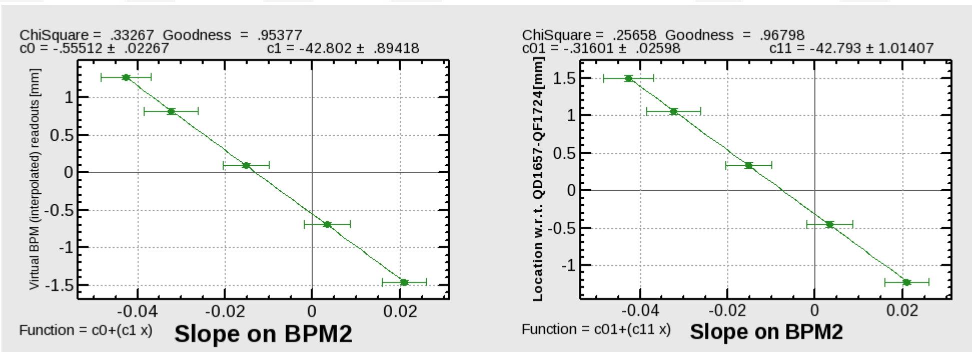

Figure 8.18. Horizontal misalignment of Q4, on left with respect to its own virtual BPM$_{Q3}$, on right, with respect to the reference line defined by Q1 and Q5.

8.2.6. Vertical magnetic center of Q4

The calculated misalignment is w.r.t. 0.277 ± 0.109 mm BPM$_{Q4}^{virtual}$ and it is 0.263 ± 0.112 mm w.r.t. reference quadrupoles, as presented in Figure 8.19

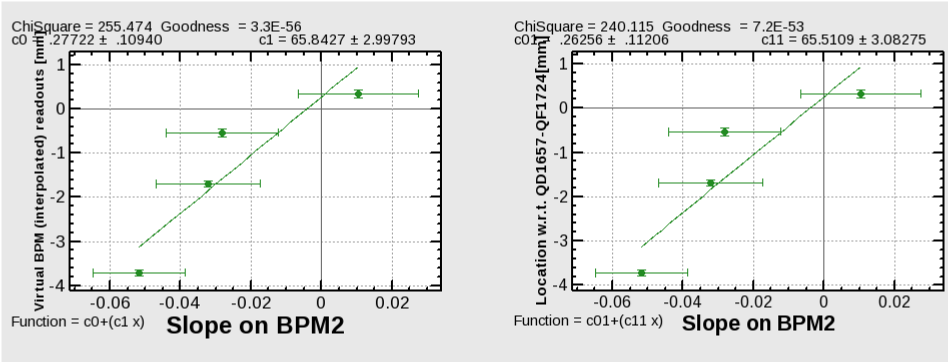

Figure 8.19. Vertical misalignment of Q4, on left w.r.t. $\text{BPM}_{Q4}^{virtual}$, on right, with respect to the reference line defined by Q1 and Q5.

8.3. Results

We have examined a total of 5 quadrupoles, 2 with BPMs in the bore (i.e. Q1 and Q5) and 3 quadrupoles without BPM. The associated errors compiled in Table 8.3 are small, below 35 μm, for all quadrupoles in the horizontal plane. The horizontal position offsets vary between -0.55 to -0.08 mm. The values are negative for all quadrupoles tested. The vertical positions offsets found vary between -0.18 mm and 0.27 mm, but these are determined with a larger error, around 100 μm, for the quadrupoles without attached BPMs, and below 38 μm for Q1 and Q5, which do have their own BPMs.

From the measured offsets, we conclude that the transverse alignment of the quadrupoles and BPMs was achieved with a precision of about 100 μm rms, which is a typical precision also at other accelerator facilities.

Table 8.4 reveals that the offsets of quadrupoles Q2 to Q4 with respect to the line defined by the Q1 and Q5 reference magnets are smaller than those with respect to their virtual BPMs, but the corresponding measurement errors are slightly larger, as expected from Eqs. (8.4) and (8.5).

Using the values of Table 8.4 we can steer the beam to the magnetic center of Q1, after physically moving the other magnets situated on the same girder (Q2 to Q5)

Table 8.3. Misaligments of the Tested Quadrupoles

Quad Name	Horizontal Offset[mm]	Vertical Offset [mm]	w.r.t. BPM
Q1	-0.502 ± 0.015	0.195 ± 0.037	SP165
Q2	-0.209 ± 0.029	-0.019 ± 0.107	$\mathrm{BPM}_{Q2}^{virtual}$
Q3	-0.419 ± 0.031	-0.173 ± 0.079	$\mathrm{BPM}_{Q3}^{virtual}$
Q4	-0.555 ± 0.023	0.272 ± 0.110	$\mathrm{BPM}_{Q4}^{virtual}$
Q5	-0.079 ± 0.025	-0.110 ± 0.025	SP172

so as to align these with respect to Q1, according to the tabulated errors.

Table 8.4. Misalignments of the Tested Quadrupoles w.r.t. Q1-Q5

Quad Name	Horizontal Misalignment[mm]	Vertical Misalignment[mm]
Q2	-0.075 ± 0.032	0.050 ± 0.109
Q3	-0.232 ± 0.034	-0.141 ± 0.082
Q4	-0.316 ± 0.026	0.263 ± 0.112

Concerning the discrepancy between the horizontal and the vertical plane, we recall that the magnitude of the pulse-to–pulse horizontal beam position jitter at BPM_2 was 62 μm, and the vertical one 104 μm, averaged over all measurements (see Table 8.2), where the horizontal and vertical design beta functions are equal to within 10%. This jitter is calculated as the average of the standard deviation on BPM_2 readings for each value of the QUT strength (20 pulses per strength). For instance, the average of the standard deviations of the top-left plot in Figure 8.7 is regarded as the jitter during that data acquisition session. The jitter on BPM_2 (or on BPM_3 for Q5) has been chosen rather than BPM_1, since we determine the quadrupole offset relying upon the slope recorded on BPM_2.

Therefore, we may conclude the following:

- We observe little correlation between the measured offsets and the associated errors, as is illustrated in Figure 8.20 for the horizontal plane.

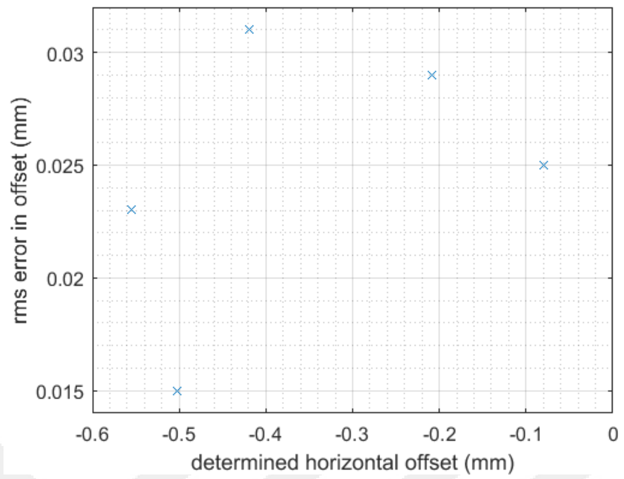

Figure 8.20. The calculated quadrupole offsets w.r.t. BPM (horizontal axis) and their errors (vertical axis).

- The size of the jitter appears to be correlated with the measurement error of the position offsets, as is illustrated in Figure 8.21.

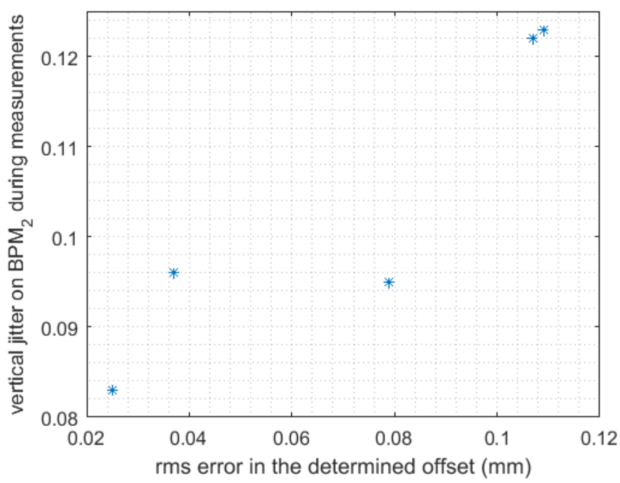

Figure 8.21. The average size of the jitter during each offset measurement versus the associated rms error.

- The beam-position jitter (and drift) limits the slope determination in the rear BPM. A larger span on this BPM allows for a better precision in the offset measurements, since the relative size of the beam jitter is reduced. For instance, the offset in Figure 8.10 is determined with a higher precision than the one of Figure 8.12. Indeed, plotting the difference of the maximum and minimum slopes against the rms errors of the offsets reveals a clear anti-correlation, as is shown in Figure 8.22.

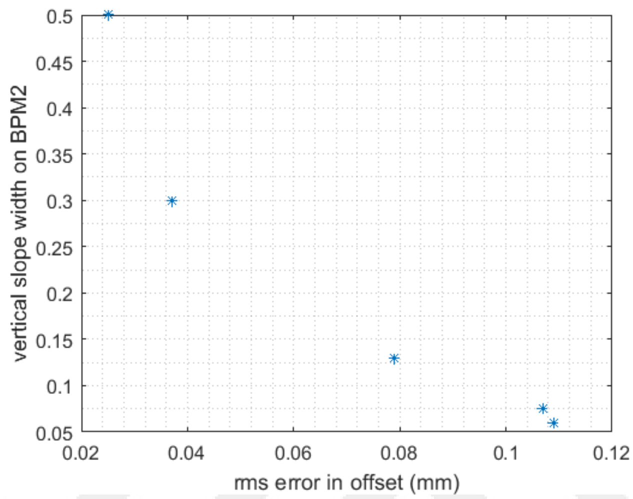

Figure 8.22. Slope width on BPM2 versus the rms measurement error of the quadrupole offsets.

In general, a reliable quadrupole offset determination requires the beam jitter to be less than 50 μm. However, the jitter is not the only parameter, a good measurement also requires the beam to pass through the QUT with varying large transverse offsets, so that the range of deflection slopes is significant, and the relative importance of the jitter reduced.

The alignment of quadrupoles is a crucial step of accelerator commissioning. The method presented in this article allows determining the misalignments of the quadrupoles in the SuperKEKB injector linac with a precision below 37 μm, and potentially even less if the beam were more stable. The existence of steerer magnets and BPMs in the vicinity of the quadrupoles to be aligned will fasten the method. However, our method can also applied to quadrupoles without BPMs located between quadrupoles equipped with a BPM, which are aligned first. In that case, for the intermediate quadrupoles without BPMs we have achieved an alignment precision of approximately 110 μm.

The ultimate aim of the study is to identify and correct the misalignments in order to avoid steering the beam, or to steer the beam exactly to the quadrupole center, to minimize the effect of wake fields. The offsets determined can either be used to steer the beam to the quadrupole center found, or the magnets can be moved mechanically by the negative offset.

The method can be further improved by taking more measurements at fixed quadrupole strength so that the error bar of the beam jitter approaches its asymptotic minimum.

This method will also assist the KEK operators in setting the steerer strength for their standard QuadBPM method, which is performed by scanning the quadrupole strengths to obtain highest transmission in the downstream BPM(s). Thanks to the method developed, they can steer the beam to a position in which a change in the the quadrupole strength does not kick the beam.

8.4. Beam Jitter at SuperKEKB linac

The beam optics and dynamics simulations are perfect tools embedding the accelerator physics and give a thorough understanding of possible main source of errors. However, stray fields, vacuum or RF failures, earthquakes, etc are not included in the simulations since they are mostly rare and can be corrected once they are realized. Therefore, there are some operational refinements needed to deliver the designated beam determined by the simulations. The operational commissioning aims to realize and resolve continuous issues such as emittance blow, beam size jitter, or any shot-by-shot variation of the beam. At the end of 640 meter long SuperKEKB linac there is a dipole bending the beam into the diagnostic station in which the transverse beam profile can be recorded. That profile was observed to not coincide with the expected design target, as can be seen in Figure 8.23. Moreover, the non-elliptical shape of the beam also proves that the beam is affected from the wakefields and the beam profile has loosen the symmetry. Besides, the beam profile recorded was seen to be moving left and right of the target (it is useful to mention that the dipole was bending horizontally), this means that the shot-by-shot beam has different energies. All together, we can conclude that the beam has jitter. For this reason, we initiated a campaign to find out what caused the jitter, then we attempted to solve the problem.

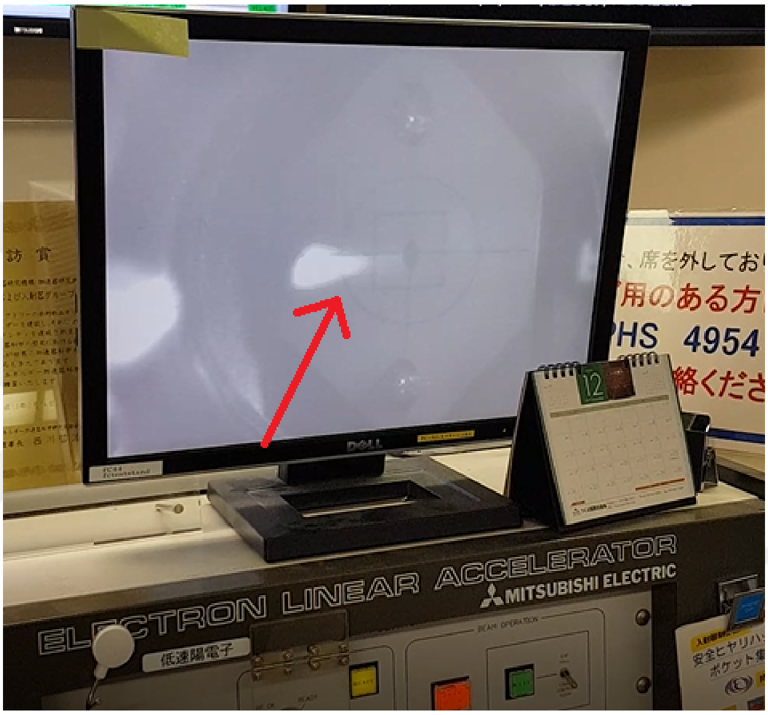

Figure 8.23. The transverse beam profile recorded at the end SuperKEKB injector linac. The beam asymmetric shape and the shot-by-shot variation of the beam incident position compelled us to investigate the jitter.

The method is to investigate by recording the time variation of the beam orbit (i.e. centroid). The SuperKEKB injector linac has 77 beam position monitors along the accelerator. Therefore, a script has been written to record the BPM readouts in *SAD*. The script printouts the horizontal, vertical, charge, and design beta functions of the beam, as presented in Figure 8.24.

Figure 8.24 is useful to claim that the BPMs and accelerators are not perfectly aligned, however beam centroid motion recorded at one session (i.e. shot) would not reflect the jitter. Instead, we have chosen to record 1000 times consecutive measurements

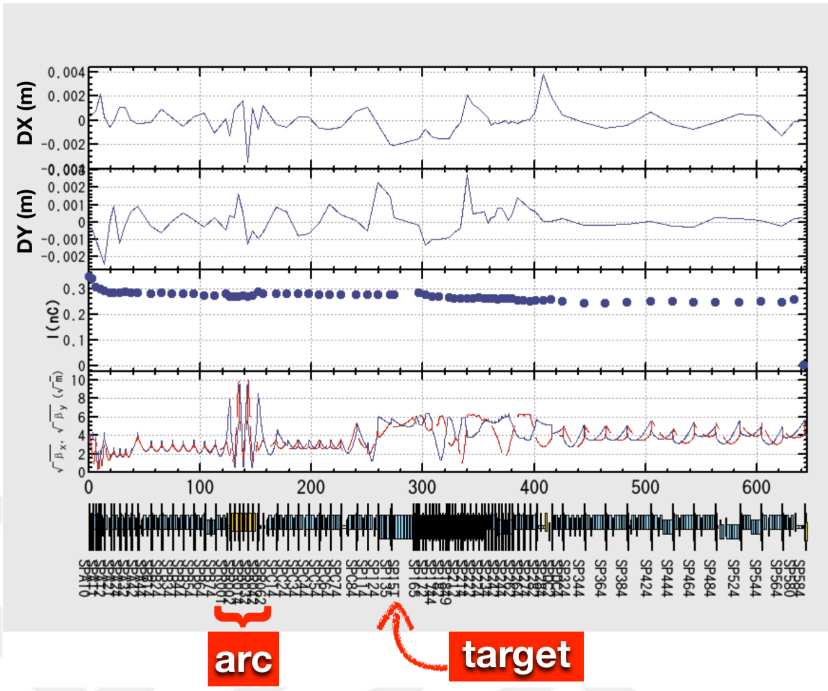

Figure 8.24. The GUI demonstrating BPM horizontal,vertical, and bunch charge measurements along the linac. The fourth plot is the design optics.

of the beam centroid and calculate rms variation of the average position on a BPM, then we plot only the rms variation recorded at each BPM, as shown in Figure 8.25.

Figure 8.25 demonstrates that there is a jitter in horizontal axis starting at the arc, and this jitter is suppressed (not apparent) until the first BPM after the target, through which the jitter couples and can be seen in both planes. Therefore, we need to focus on the arc and then the region after the target. The arc is an 180° isochronous achromat [88], meaning that the $R_{56} = 0$ element of the transfer matrix is set to zero such that the dispersive term in Equation 2.55 is zero. In other words, this bent of the beam is supposed to be dispersion free, such that the motion keeps its linearity.

However, it seems the beam size oscillations in the horizontal axis in Figure 8.24 somehow get suppressed or even annihilated after the arc, yet they reappear after the target in both transverse planes. Therefore, before jumping into conclusion, we will investigate the existence of the jitter through different linac beam optics settings. There are some different linac operational modes since KEK is also a synchrotron radiation

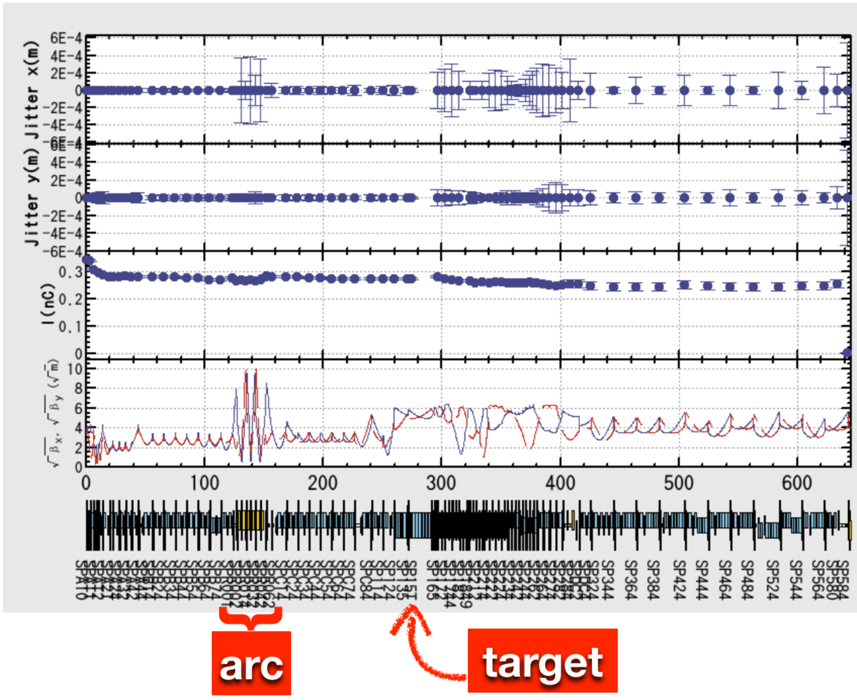

Figure 8.25. The rms variation of the beam orbit during 1000 consecutive BPM readouts.

facility used for biological sciences and so on. The modes used during data acquisition presented in this section is presented in Table 8.5. Of course, the charge and linac repetition for each mode can be changed as we will do. However, our aim was to see the impact on different optics meanwhile we make sure that our acquisition can record the continuous flow of data for long enough time.

Table 8.5. KEK linac modes used during jitter study.

Modes	Aim	Bunch Charge	Repetition
QFE	injection to photon factories	0.3 nC	5 Hz
KBE	KEKB electron injection	1.0 nC	5 Hz
SFE	RG-gun low emittance electrons	2 nC	5 Hz
KBP	KEKB positron injection	10 nC $e^- \rightarrow$ 2 nC e^+	5 Hz

we will delay the discussion of the oscillations at the arc and focus on the early part of the positron linac. The positron target, capture and pre-injector linac are densely packed avoiding the beam instrumentation (i.e. diagnostics) elements to be

Figure 8.26. KEK 180° bend isochronous achromat which was built to bridge the extension to the old linac in parallel. Thus, the linac has become J-shaped.

deployed for about 20 m downstream of the target, as depicted in Figure 8.27 and the absence of BPM at that region can be realized in Figure 8.25. Moreover, there are pulsed steerers to create orbit bump to hit the positron target, and then the following structures are centered with respect to the positron beam. Therefore, one may argue that the beam is off-centered for electron beams at that section.

The QFE mode mentioned in Table 8.5 is already presented in Figure 8.25. It might be even more useful to zoom in after the target region for QFE mode which is shown in Figure 8.28. The jitter has nodes, therefore it suggests that it follows the phase advance set by the quadrupoles. we will also switch the beam mode to KBE and send around 1 nC bunch charge, as shown in Figure 8.29.

The horizontal rms jitter size after the target seems to become 400 μm in Fig-

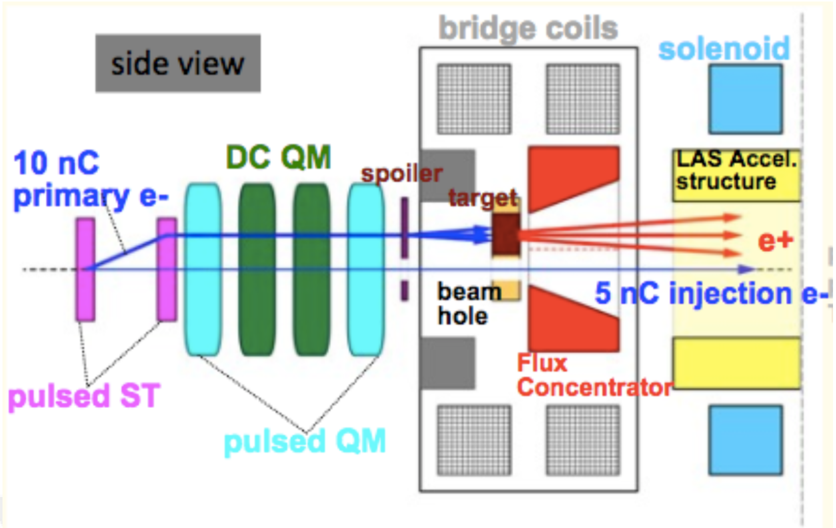

Figure 8.27. KEK positron production region.

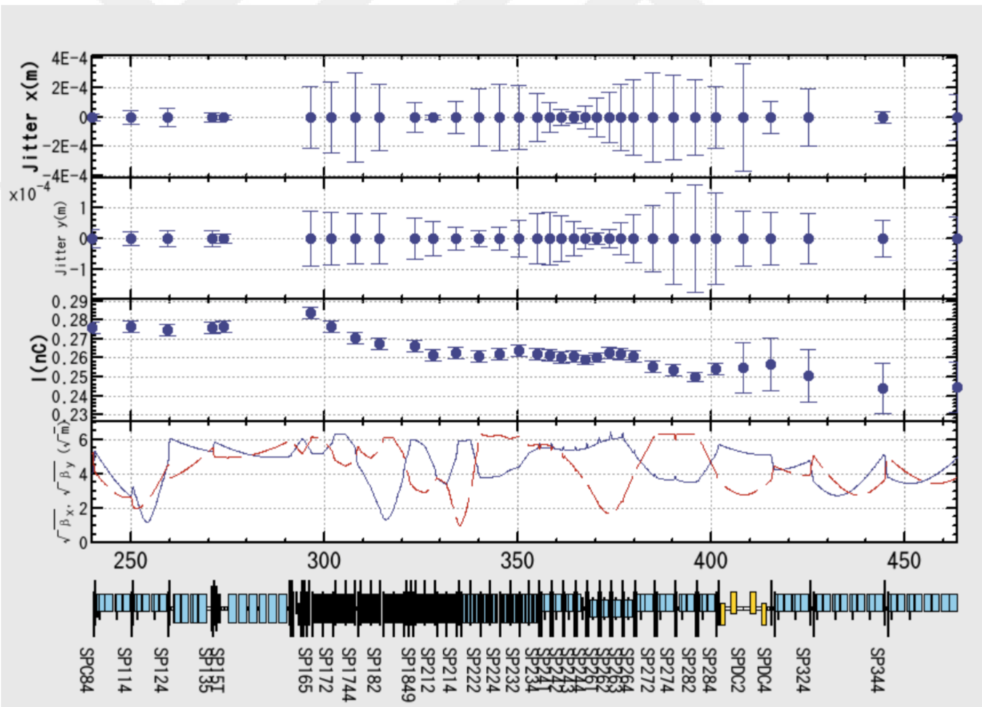

Figure 8.28. The jitter after the positron converter.

ure 8.29 compared with Figure 8.25 which whas around 300 μm. Therefore, we need to immediately check with the charge jitter correlation by accelerating different charges in the linac, as we did in Figure 8.30. In this figure, the subtle point is to compare the charge which is passing through the positron target (recall that the target has a

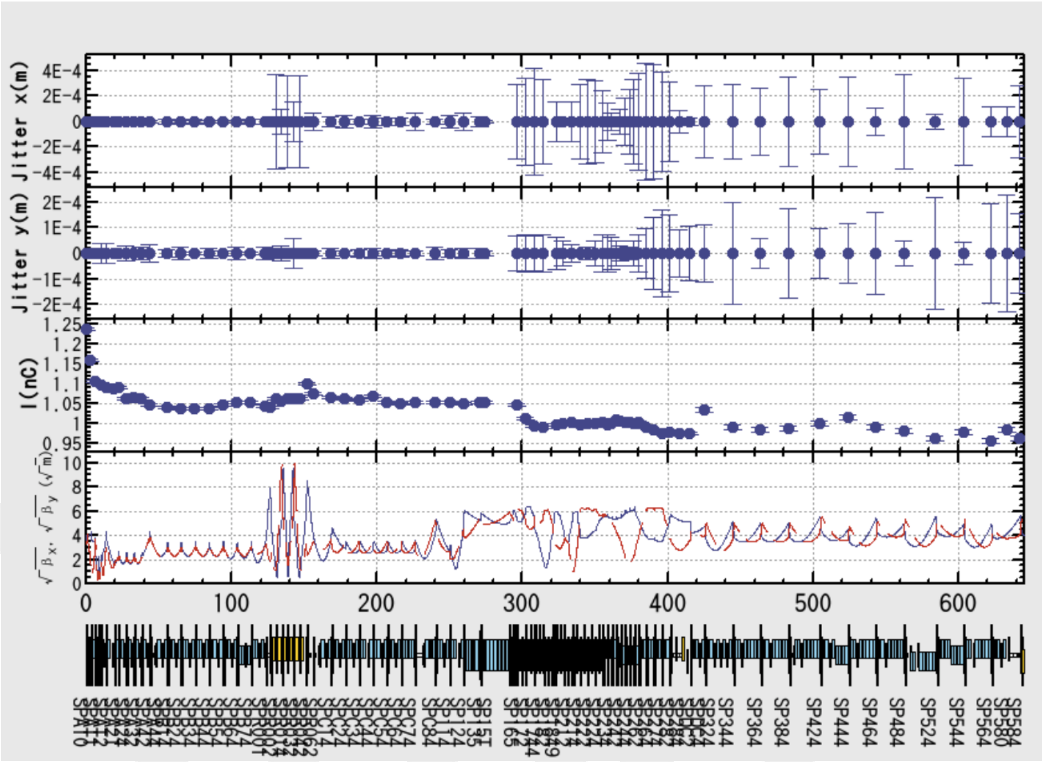

Figure 8.29. The jitter of 1 nC bunch charge in KBE mode.

pinhole for electron beam and hits the target only when the pulsed steerers are on, thus electron beam passes through the pinhole) versus the largest horizontal rms jitter recorded after the target. To sum up, we will compare the charge at *SP15T* versus the horizontal rms jitter at *SP1744* from optics desk, which their names can be more easily seen in Figure 8.28, as shown in Figure 8.30.

Figure 8.30 may suggest that the jitter is correlated to the charge and therefore, wakefield deflection due to the target pinhole on the electron beam resulting in the jitter. However, the linear fit does not pass through (0,0), in other words, the jitter is correlated to the charge, however, it may not be the initial, or we will say, only cause of the jitter. we will switch to the positron creation mode (KBP), what BPMs will measure is the electron charge up to the target which will be followed by the positron charge generated, as can be seen in Figure 8.31.

In Figure 8.31, there are subtle changes. First, the jitter at the arc is bigger

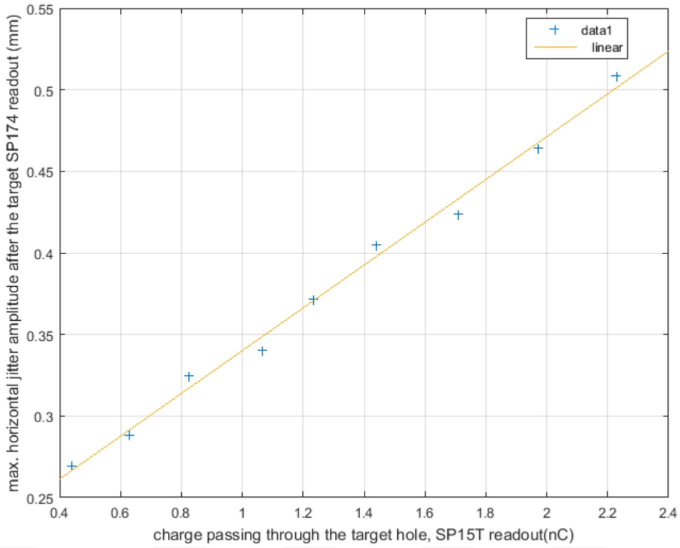

Figure 8.30. There is a linear correlation between the charge and the jitter recorded around the positron target.

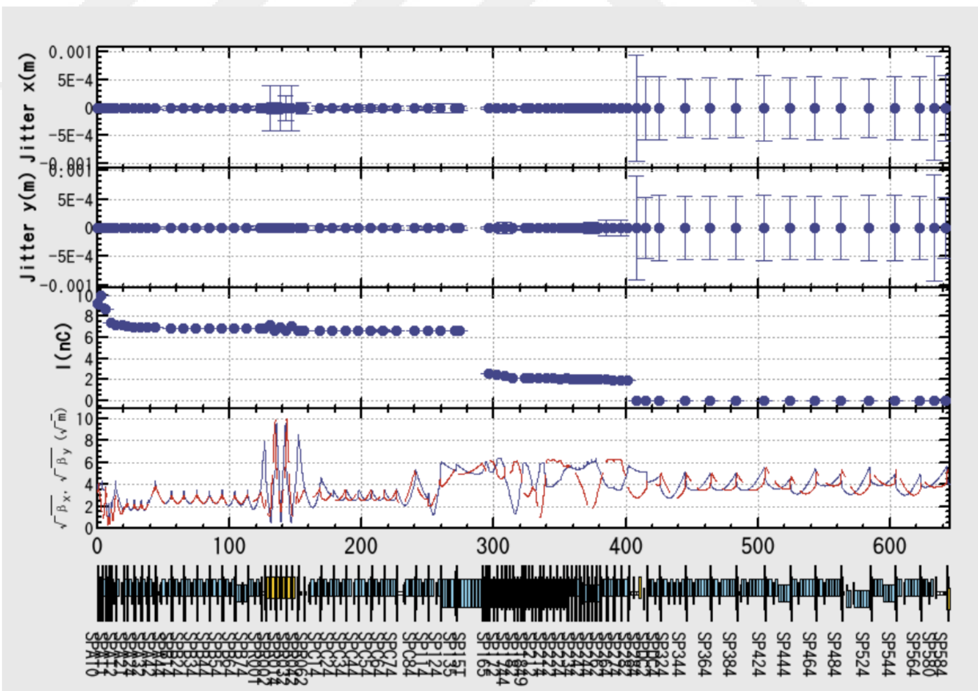

Figure 8.31. There is a linear correlation between the charge and the jitter recorded around the positron target.

compared to the QFE, KBE mdoes. Second, there is no jitter (i.e. below 50 μm quantitatively) after the target even though the positron charge is above 2 nC. Also, the positrons are damped around 400 meter of the linac via a chi-cane, because normally beam is supposed to enter the DR, and not continue directly in the linac. Therefore, after the 400 meters of the accelerator the recorded jitter is meaningless values. All in all, we arrive at the following hypotheses:

- the wakefield deflection of the pinhole in the target is the source,
- the jitter may have started due to flux concentrator,
- the jitter is caused due to the off-axis entrance to the 15 m long solenoid.

We have checked all these options, first we have analytically calculated the deflection [89], turned off the solenoid (see Figure B.1), then turned off the flux concentrator (see Figure B.2), however none of the hypothesis could be identified as being responsible for the jitter. Therefore, one may wonder whether all the beams used up to now were sent from the thermionic gun, and had better to switch to the RF gun since it can deliver smaller emittance beam. Therefore, we can use the SFE mode, in which the beam sent is generated from the RF gun. The jitter in SFE mode is presented in Figure 8.32.

To sum up, even though it is quite compelling to hold the region after the target responsible for the jitter, it turned out that we need to look somewhere else. If the jitter after the target actually stems from the arc, we should see a correlation between the two jitters. To commence with, we will zoom in to the horizontal jitter presented in Figure 8.32, and the zoomed version is shown in Figure 8.33.

Figure 8.33 shows the nodes and maxima of the jitter. Therefore, we can immediately compare it with the design optics, since the jitter seems to demonstrate a sinusoidal change. First, the phase advance between the *first largest* jitter and the target in the design optics has 1.21 radian phase advance, we would expect exactly $\pi/2$ if the target was the node (i.e. the origin of the jitter). Second, the phase advance between the *first smallest* and target is 3.88 radian, which we would expect π. Third, the phase advance between the *second smallest* and the target is 6.56 radian, we would expect 2π. Lastly, the *second largest* and the target is 7.17 radian which we would ex-

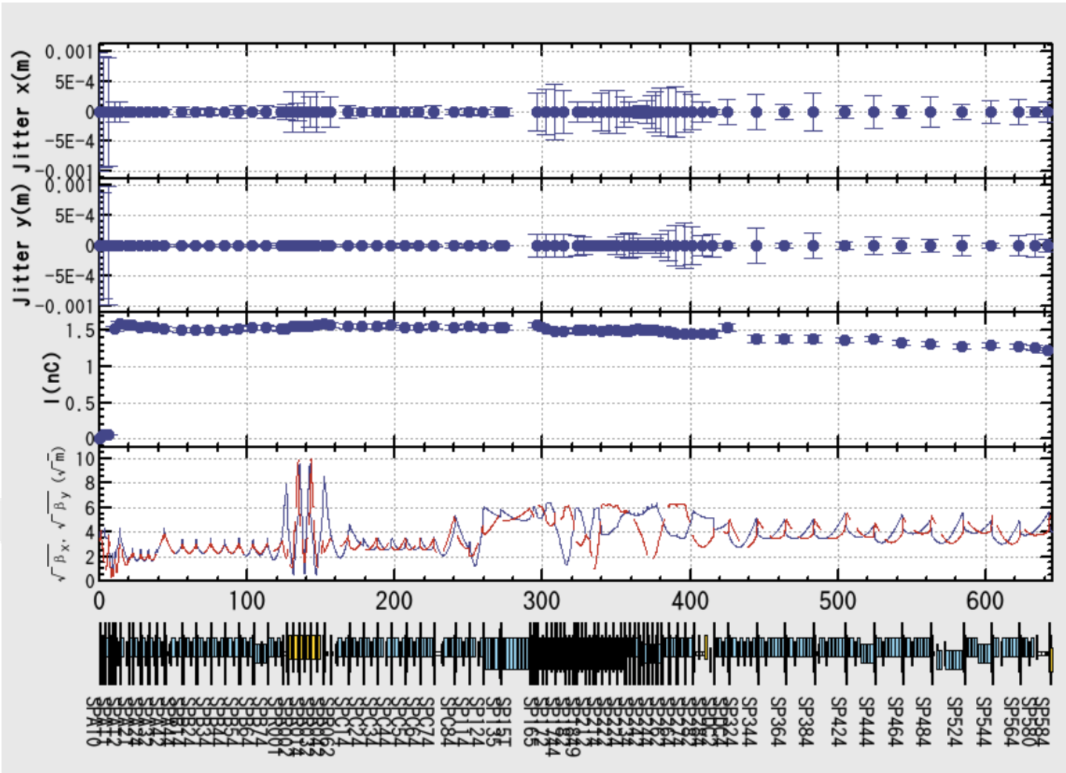

Figure 8.32. The jitter still exists in SFE mode in which the beam is generated from the RF gun. The start of the data is the recording from the BPMs located at the thermionic gun side, which are taken for compatibility and should be ignored.

pect $5/2\pi$. However, one should also take into account that the operational optics may be different than the designed nominal optics, due to sporadic operational tuning (i.e. QuadBPM [81]). Therefore, it seems the jitter more or less obeys the phase advance. Apart from this, we can also zoom in to the jitter in the arc of the same data presented in Figure 8.32, and the zoomed version is shown in Figure 8.34.

The correlation between the largest in the arc versus both vertical and horizontal largest jitter after the target demonstrates a correlation. Moreover, the largest in the arc seems to be correlated to the smallest after the target. The smallest and largest in the arc are also correlated. All the relevant plots are shown in Figure B.3. Moreover, another set of plots can be seen in Figure B.4 which certify that the measurements recorded by the BPMs seem to obey Gaussian distribution through which we were always modeling the rms jitter size.

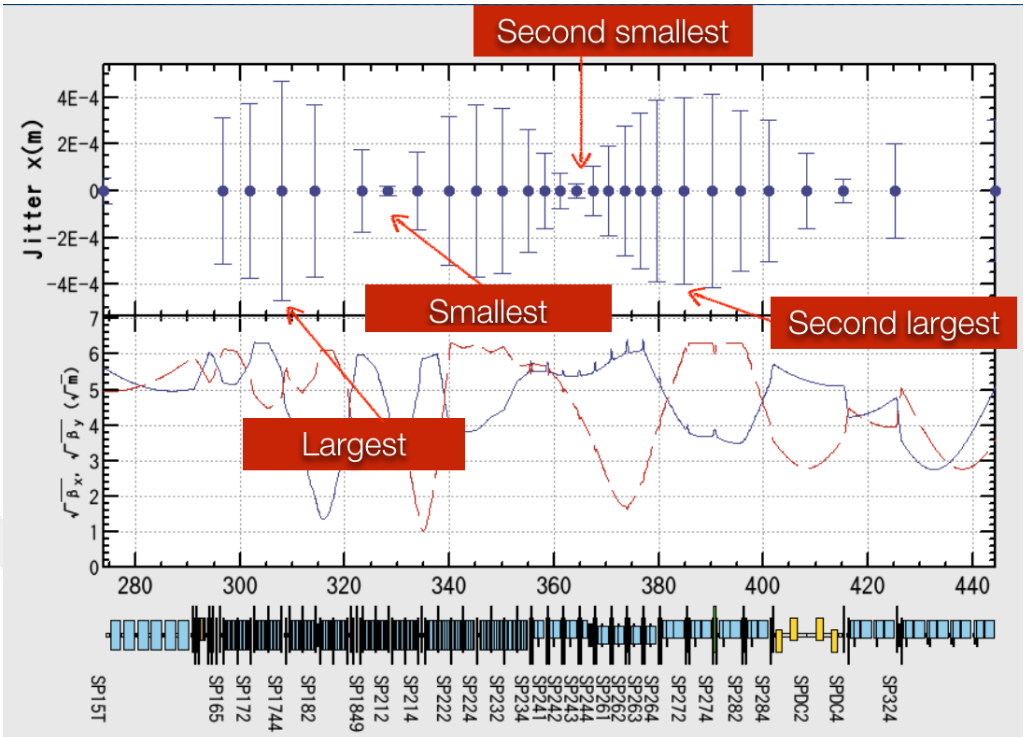

Figure 8.33. Closer look to the horizontal jitter after the target in SFE mode, and labelling of the maxima and minima are meant to compare with those in the arc.

To date, there seems the jitter is due to leaked dispersion from the arc which is transferred up to the target. This jitter is partially enhanced by the target hole. The nonvisual jitter between the arc and all the way downstream to the target is because of the strong focusing of the quadrupoles. In other words, if we normalize the rms jitter to the square-root of the designed β-function [7] , we will see the jitter exists largely in the arc and some enhancement after the target, as shown in Figure 8.37. The vertical jitter scale in Figure 8.37 is order of magnitude smaller than the horizontal, which is actually aroused due to coupling of planes led by the 15 m long solenoid.

[7]Recall Equation2.46 which is $x = \sqrt{\epsilon\beta}$, therefore it is reasonable to normalize the beam size by the square-root of β.

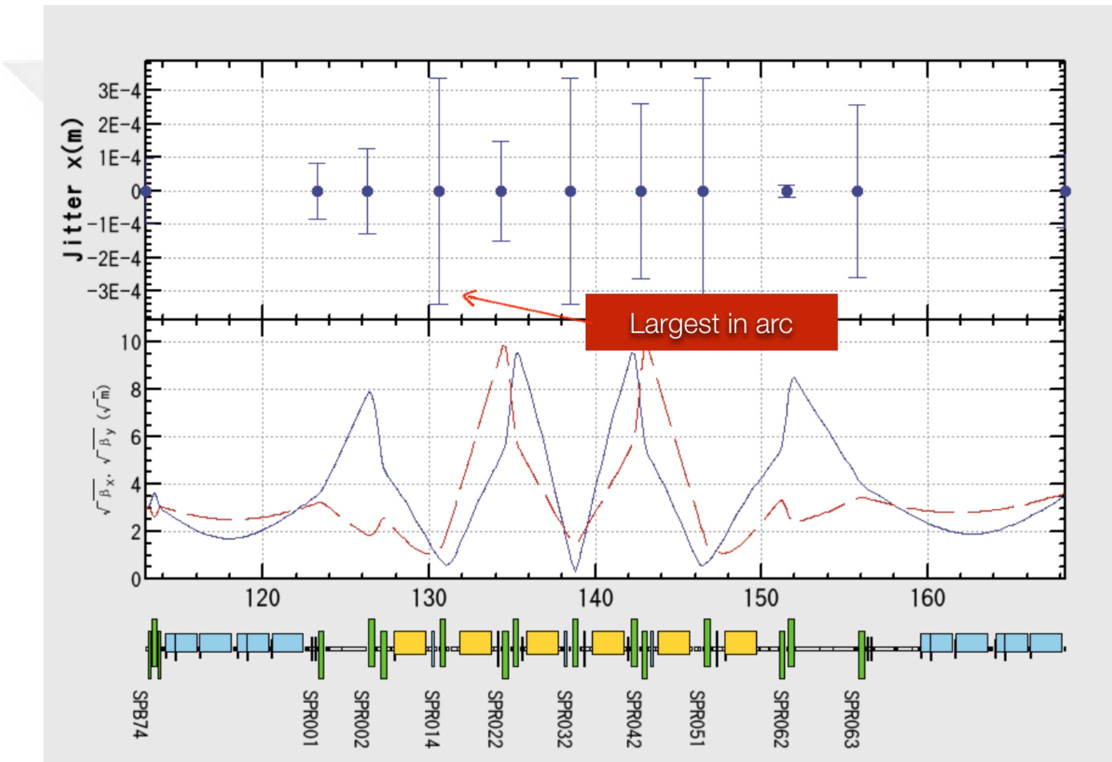

Figure 8.34. Closer look to the horizontal jitter in the arc in SFE mode, and labelling of the maximum is to compare with those occurred after the target.

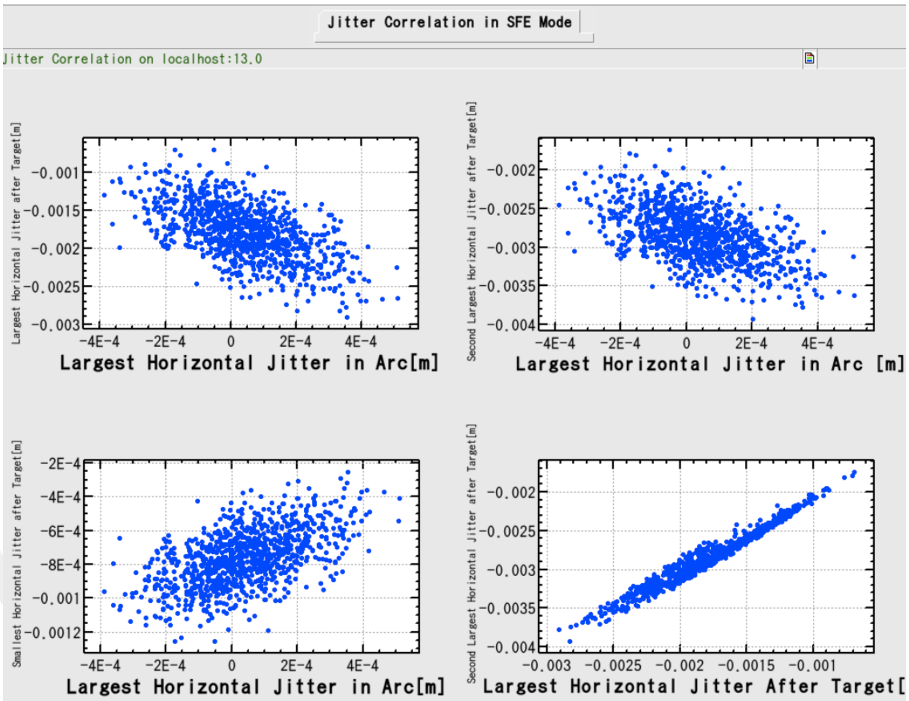

Figure 8.35. Correlation plots in SFE mode. It seems that the jitter in the arc and after the target are linked.

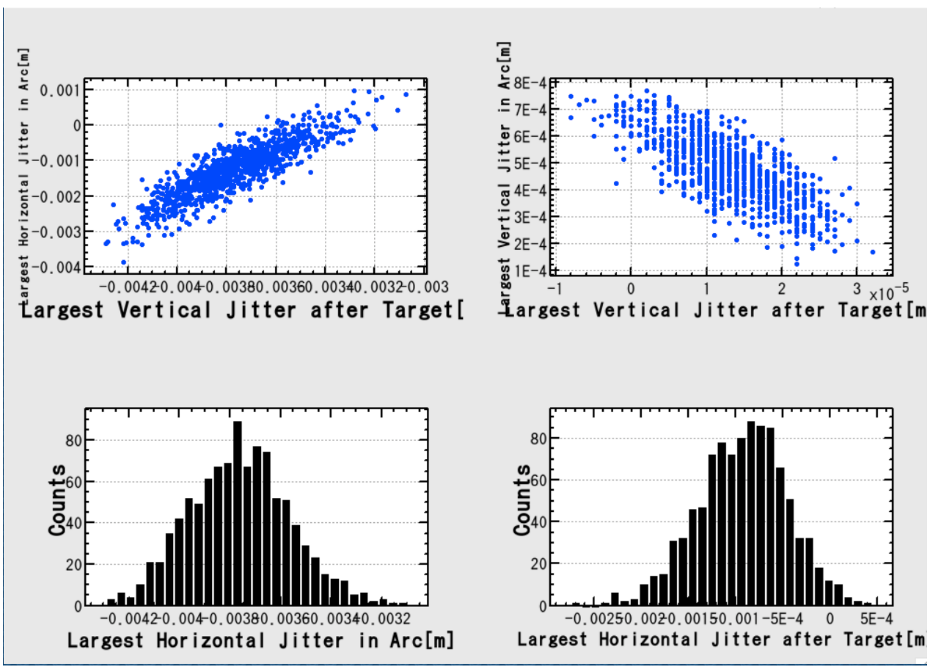

Figure 8.36. Correlation plots in SFE mode. The histograms are shown in order to verify that the BPM measurements mostly obey normal distribution.

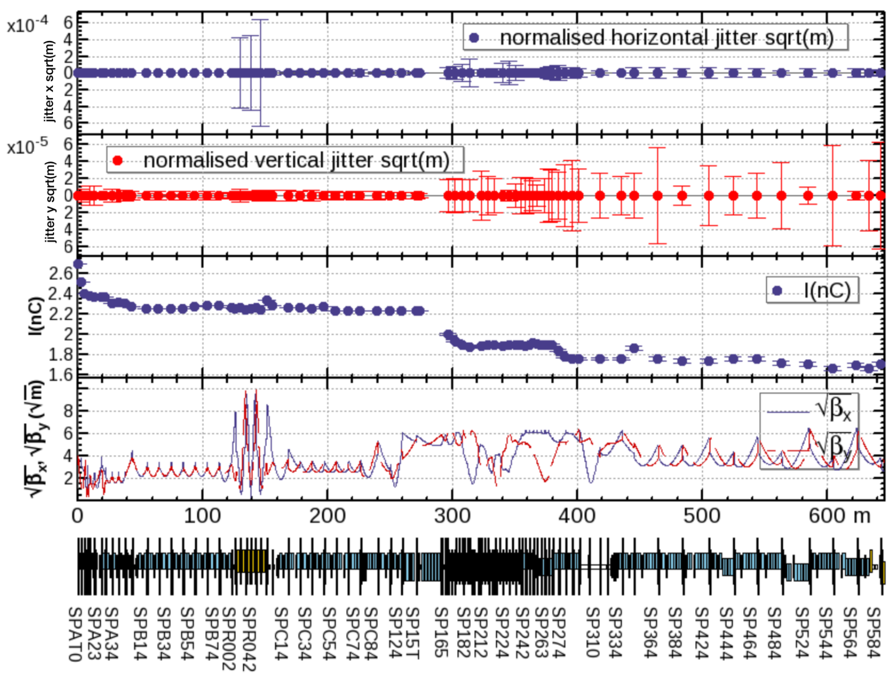

Figure 8.37. Rms jitter size is normalized to the square-root of the corresponding β-function at that BPM. It shows implicitly the jitter starts in the arc, and slightly enhanced after the target.

9. CONCLUSION

The Future Circular Collider study has been initiated in 2014 and FCC collaboration submitted its conceptual design report (CDR) in December 2018 [1]. The linac and damping ring designs as well as bunch schedules presented in this thesis have taken place in the Volume II of the CDR.

The optimisation of bunch schedules and injector baseline table are crucial in order to assure that the FCC-e^+e^- can reach extremely high target luminosities. Even more importantly, the FCC-e^+e^- can maintain delivering peak luminosity during operation thanks to quasi-continuous top-up injection from the 98-km main booster and the injector chain. We have shown that the injectors can fill the collider in 17 minutes at the Z pole and fill the collider in shorter time for other operations, such as 4 mins in $t\bar{t}$.

The S-band 6 GeV linear accelerator has perfect transmission and keep the low emittance beam within only 15% blow-up which can be very safely accepted by the pre-booster synchrotron (PRB). The SPS of CERN is the primary candidate to be the PRB of the FCC-e^+e^-. However, a new synchrotron of 2.9 km or an extension of the linac up to 20 GeV are also studied as alternatives. A 437.4 meter extension of the 6 GeV linac with C-band cavities has also demonstrated satisfying results. Together with such C-band extension, the 20 GeV linac will be 765 meters, excluding the possible (20-30 meter long) positron capture/pre-injector section.

The positron study for the FFC-e^+e^- is an ongoing work with a damping ring that is primarily designed for the positron emittance cooling. The optics design of the DR together with tracking including intra-beam scattering is currently satisfying. However, the iterative work is needed to properly address instabilities and errors.

Apart from the FCC-e^+e^- injector study, this thesis also describes two hands-on linac control campaigns carried out at KEK in Japan. The beam-based misalignment study allows a determination of misalignment of a quadrupole with a BPM in the bore with an rms precision below 37 μm which is limited only by the jitter size of the beam. This new method or the enhancement we introduced to the already existing QuadBPM method is still applied in daily operations of the SuperKEKB injector linac. Finally, the beam jitter study campaign in the SuperKEKB linac has important clues about the possible source of jitter that is reducing the quality of the beam. The dispersion leak from the arc and wakefield deflection from the pinhole in the positron converter have been identified. These issues are being addressed by the SuperKEKB crew.

REFERENCES

1. Future Circular Collider Study. Volume 2: The Lepton Collider (FCC-e^+e^-) Conceptual Design Report, preprint edited by M. Benedikt et al. CERN accelerator reports, CERN-ACC-2018-0057, Geneva, December 2018, accepted for publication to Eur. Phys. J. ST.

2. K. Oide *et al.*, "Design of Beam Optics for the Future Circular Collider e^+e^- collider rings", Phys. Rev. Accel. Beams 19, 111005 (2016).

3. D. Shatilov, K. Oide, *Luminosity at ttbar with 400 and 800 MHz RF*, `https://indico.cern.ch/event/686197/contributions/2814861/attachments/1571535/2479473/rf800_ttbar.pdf`, accessed in May 2019.

4. D. Shatilov, *Luminosity Optimization for FCC-ee: recent results*, `https://indico.cern.ch/event/661041/contributions/2697585/attachments/1512904/2359918/lumi_param.pdf`, accessed in May 2019.

5. S. Ogur *et al.*, "Layout and performance of the FCC-e^+e^- pre-injector chain", IOP Conf. Series: Journal of Physics: Conf. Series, 1067, 022011, 2018.

6. O. Etisken *et al.*, "Pre-Booster Ring Considerations for the FCC e^+e^- Injector", Proceedings of Int. Particle Accelerator Conf. (IPAC'18), MOPMF002, Vancouver, Canada, 2018.

7. B. Harer *et al.*, "Status of the FCC-e^+e^- Top-up Booster Synchrotron", Proceedings of Int. Particle Accelerator Conf. (IPAC'18), Vancouver, Canada, Apr.-May 2018, MOPMF059.

8. T. Charles *et al.*,"Bunch Compression and Turnaround Loops Design in the FCC-e^+e^- Injector Complex", Proceedings of Int. Particle Accelerator Conf. (IPAC'18), Vancouver, Canada, Apr.-May 2018, THPAF037, this conference.

9. S. Ogur *et al.*, "Bunch Schedules for the FCC-e^+e^- Pre-injector", Proceedings of Int. Particle Accelerator Conf. (IPAC'18), Vancouver, Canada, Apr.-May 2018, MOPMF001.

10. Xabier Cid and Ramon Cid, *Taking a Closer Look at LHC* https://www.lhc-closer.es/taking_a_closer_look_at_lhc/0.lhc_running, accessed in May 2019.

11. S. Ogur *et al.*, "Overall Injection Strategy for FCC-e^+e^-", Proceedings of the High Luminosity Circular e+e- Colliders (eeFACT2018), Hong Kong, China, TUPAB03.

12. A. V. Andrianov *et al.*, "Development and low power test of the parallel coupled accelerating structure", JINST 11 P06007, 2016.

13. D. Zhou and K. Oide, *Maps used in SAD*, http://research.kek.jp/people/dmzhou/SAD/Manual/Maps_in_SAD.pdf, accessed in October 2018.

14. A. Wolski, "Beam Dynamics in High Energy Particle Accelerators", Imperial College Press, ISBN: 978-1-78326-277-9, 2014.

15. V. Yildiz, "CERN Linac4 Beam Dynamics Studies and Commissioning up to 12 MeV", PhD Thesis, Bogazici University, 2015.

16. KEK Accelerator Laboratory, *SAD (Strategical Accelerator Design)*, http://acc-physics.kek.jp/SAD/index.html, accessed in January 2019.

17. R. Steerenberg, *AXEL-2018: Introduction to Particle Accelerators*, https://indico.cern.ch/event/704869/ accessed in January 2019.

18. H. Wiedemann, "Particle Accelerator Physics", Stanford, CA, USA, Springer, ISBN: 978-3-319-18316-9 (2015).

19. E.D. Courant, H.S. Snyder, "Theory of the Alternating-gradient Synchrotron", Annals of Physics, Volume 3, Issue 1, January 1958, Pages 1-48.

20. Bernhard J. Holzer, "Beam optics and lattice design for particle accelerators", DOI: 10.5170/CERN-2013-001.171, arXiv:1303.6514 (2013).

21. D. A. Edwards and M. J. Syphers, "An Introduction to the Physics of High Energy Accelerators", John Wiley& Sons, Inc. ISBN-13: 978-0-471-55163-8 (2004).

22. S. Di Mitri, *Transverse Dynamics, Single Particle*, http://uspas.fnal.gov/materials/15Rutgers/lecture_Tu6.pdf, accessed in May 2019.

23. E. Métral and D. Möhl,“Transition Crossing”, Report No. CERN-2011-004, 2011, p. 59.

24. W. Barletta, *Synchrotron Radiation - I*, http://uspas.fnal.gov/materials/09UNM/Unit_11_Lecture_18_Synchrotron_radiation.pdf, accessed in May 2019.

25. Deutsches Elektronen-Synchrotron DESY, *How does a synchrotron radiation source work?* http://photon-science.desy.de/research/students__teaching/primers/synchrotron_radiation/index_eng.html, accessed in May 2019.

26. Matthew Sands, “The Physics of the Electron Storage Rings an Introduction”, SLAC-121, UC-22 (ACC), 1970.

27. C. Bracco, *Injection: Hadron Beams*, https://indico.cern.ch/event/451905/contributions/2159032/attachments/1425216/2188137/CAS_ERICE_Hadrons_Injection.pdf, accessed in January 2019.

28. F. Zimmermann, “Introduction to Collective Effects in Particle Accelerators”, ICFA Beam Dyn. Newslett. 69, 8-17 (2016).

29. E. Belli *et al.*, “Single Bunch Instabilities in FCC-e^+e^-”, in Proceedings of IPAC2018, Vancouver, BC, Canada, pp. 3336-3339.

30. M. Ferrario *et al.*, “Space Charge Effects”, CAS - CERN Accelerator School: Advanced Accelerator Physics Course, Trondheim, Norway, 18 - 29 Aug 2013, pp.331-356 (CERN-2014-009).

31. A. Wolski, “Damping Ring Design and Physics Issues: Space Charge, Intrabeam Scattering, Touscheck Effects”, Lecture of the Fourth Int. Acc. School for Linear Colliders, Beijing, China (2009).

32. M. Bassetti and G.A. Erskine, “Closed expression for the electrical field of a two-dimensional Gaussian charge”, CERN-ISR-TH/80-06 (1980).

33. A. Chao, "Beam Dynamics of Collective Instabilities in High energy Accelerators", Proceedings of the CAS-CERN Accelerator School: Intensity Limitations in Particle Beams, Geneva, Switzerland, CERN Yellow Reports: School Proceedings, Vol. 3/2017, CERN-2017-006-SP.

34. W. Barletta, *Beam Loading and Wakefields*, USPAS 2010, `http://uspas.fnal.gov/materials/09UNM/Unit_4_Lecture_13_Beam_loading_&_wakefileds.pdf`, accessed in March 2019.

35. K. Yokoya, "Short-Range Wake Formulas for Infinite Periodic Pill-Box", 1998, unpublished.

36. F.J. Decker *et al.*, "Long-Range Wakefields and Split-Tune Lattice at the SLC", SLAC–PUB–7259, 1996.

37. D.H. Dowell, P.G. O'Shea, "Coherent synchrotron radiation induced emittance growth in a chicane buncher", DOI: 10.1109/PAC.1997.751051, Particle Accelerator Conference, Vancouver, BC, Canada (1997)

38. H.H. Braun *et al.*, "Emittance growth and energy loss due to coherent synchrotron radiation in a bunch compressor", Physical Review Special Topics- Accelerator and Beams, VOLUME 3, 124402 (2000).

39. S. Di Mitri, M. Cornacchia, and S. Spampinati, "Cancellation of coherent synchrotron radiation kicks with optics balance," *Phys. Rev. Lett.*, 110, 014801, 2013.

40. R. Hajima, "A first-order matrix approach to the analysis of electron beam emittance growth caused by coherent synchrotron radiation," *Japanese Journal of Applied Physics, Part 2: Letters*, 42, pp. 974–976, 2003.

41. K. Kubo *et al.*, "Intrabeam scattering formulas for high energy beams", Phys. Rev. ST Accel. Beams 8, 081001 (2005).

42. V.Balakin, A.Novokhatsky and V.Smirnov, "VLEPP: Transverse Beam Dynamics", Proc. of the 12th International Conference on High-Energy Accelerators, Batavia, Illinois, p. 119 (1983).

43. A. Chao, Physics of Collective Beam Instabilities in High Energy Accelerators, Wiley (1993).

44. A. Piwinski, “Synchrotron Sidebands of Betatron Coupling Resonances”, DESY 93-189, ISSN 0418-9833, 1993.

45. D. Shatilov, K. Oide, *Luminosity Optimization for FCC-ee: recent results*, `https://indico.cern.ch/event/661041/`, accessed in May 2019.

46. T. Naito *et al.*, “Direct Generation of Multi-Bunch with Thermionic Gun”, KEK Preprint 92-64 (1992).

47. Y. D. Chernousov *et al.*, “Accelerating structure with parallel connection”. Patent for invention (Russia), No. RU2472244C1, BI. 01/10/2013, No: 1.

48. G. I. Kuznetsov, “IrCe Cathodes For EBIS *Journal of Physics: Conference Series 2*, p. 35-41 (2004).

49. Satoh D *et al.*,“Research and development of iridium cerium photocathode for SuperKEKB injector linac”, *Energy Procedia Volume 131* Pages 326-333, 2017.

50. A.M. Barnyakov *et al.*, *RF gun based on parallel coupled accelerating structure for high charge and low emittance*, `https://indico.cern.ch/event/655723/contributions/2670903/attachments/1498777/2333386/RF_gun_based_on_parallel_coupling_accelerating_structure_FCC.pdf`, accessed in May 2019.

51. J. T. Seeman *et al.*, “Measured Optimum BNS Damping Configuration of the SLC Linac”, SLAC-PUB-6204 (1993).

52. Y. Sun and C. Adolphsen, “Linac alignment algorithm: analysis on 1-to-1 steering”, SLAC-PUB-14323 (2011).

53. P. Emma et al.,“Beam-Based Alignment of Sector 1 of the SLC Linac ”, Proceedings of the 1992 European Particle Accelerator Conference, 1625 (1992).

54. R. Ostojic, “The LHC Insertion Magnets”, 7th International Conference on Magnet Technology (MT17), 24-28 September 2001, LHC Project Report 532, Geneva, Switzerland.

55. R. H. Helm, Technical Report SLAC-2, SLAC, Stanford, CA, USA (1962).

56. John T. Seeman and John C. Sheppard, "Special SLC Linac Developments", Proceedings of the 1986 International Linac Conference, Stanford, California, USA.

57. Z. D. Farkas *et al.*, "SLED: A Method of Doubling SLAC's Energy", SLAC-PUB-1453, June 1974.

58. SLC Design Report, SLAC-R-714, Stanford, California 94305 (1984).

59. M. Yoshida *et al.*, "Study on High-current Multi-bunch Beam Acceleration for KEKB Injector Linac", Proceedings of LINAC 2006, WEI-2, Knoxville, Tennessee USA, MOP025.

60. A. Vivoli *et al.*, "The CLIC Positron Capture and Acceleration in the Injector Linac", CLIC – Note - 819, CERN-OPEN-2010-020, 2010.

61. I. Chaikovska *et al.*, "Experimental Activities on High Intensity Positron Sources Using Channeling", Proceedings of IPAC'17, Copenhagen, Denmark, WEPIK002, 2017.

62. P. Martyshkin, *Preliminary result of FCC positron source simulation*, CERN, Geneva, Switzerland, accessed in September 2018, `https://indico.cern.ch/event/623025/contributions/2576145/attachments/1452960/2241145/Presentation2.pdf`, accessed in May 2019.

63. I. Chaikovska *et al.*, *Positron source*, talk presented at the FCC-week 2017, Berlin, Germany, accessed in March 2018, `https://indico.cern.ch/event/556692/contributions/2590440/attachments/1468997/2272259/e_FCCweek2017_IC.pdf`, accessed in May 2019.

64. P. Martyshkin, *FCC-e^+e^- Flux Concentrator Computer Models*, CERN, Geneva, Switzerland, accessed in September 2018, `https://indico.cern.ch/event/749013/contributions/3098680/attachments/1699198/2735883/FCC-FC.pdf`, accessed in May 2019.

65. N. Iida *et al.*, "Beam Dynamics in Positron Injector Systems for the Next Generation b-Factories", Proceedings of IPAC 2011, THYA01, San Sebastian, Spain, 2011.

66. L. Zang *et al.*, "Design and Optimisation of Flux Concentrator for SuperKEKB", Proceedings of IPAC 2012, TUPPD032, New Orleans, Louisiana, USA.

67. Naoko Iida, Takuya Kamitani (KEK), *private communication.*

68. N. Iida *et al.*, "Design of the Positron Transport System for SuperKEKB", Proceedings of IPAC'10,THPD004, Kyoto, Japan (2010).

69. M. Kikuchi *et al.*, "Design of Positron Damping Ring for Super-KEKB", Conf.Proc. C100523, TUPEB054 (2010).

70. J. E. Clendenin *et al.*, "ILC at SLAC R&D Program for a Polarized RF Gun", SLAC-PUB-11657, January 2006.

71. Alexander W. Chao, "Evaluation of Radiative Spin Polarization in an Electron Storage Ring", Nuclear Instruments and Methods 180 (1981) p.29-36.

72. D. Quatraro *et al.*, "Coherent tune shift and instabilities measurements at the CERN Proton Synchrotron Booster", Proceedings of PAC09, TH5PFP013, Vancouver, BC, Canada (2009).

73. Katsunobu Oide (CERN & KEK), *private communication.*

74. F. Yaman, "Electron Cloud Build-up Comparisons for FCC-ee Damping Ring at Injection and Extraction", `https://indico.cern.ch/event/797022/`, accessed in April 2019.

75. S. Ogur, N. Iida, T. Kamitani, K. Oide and F.Zimmermann, "Beam-based alignment of the SuperKEKB linac quadrupoles", Nuclear Inst. and Methods in Physics Research, A 925 (2019) 199–211.

76. M. Satoh *et al.*, "Commissioning Status and Plan of SuperKEKB Injector Linac", Proceedings of IPAC2015, Richmond, VA, USA, TUPTY008 (2015).

77. K. Furukawa *et al.*, "High Intensity and Low-Emittance Upgrade of 7 GeV Injector Linac Towards SuperKEKB", Proceedings of IPAC2013, Shanghai, China, TUPME010 (2013).

78. C. Adolphsen and T. O. Raubenheimer, "Method to Evaluate Steering and Alignment Algorithms for Controlling Emittance Growth," Presented at the 1998 IEEE Part. Acc. Conf, Washington D.C. (1993).

79. T. O. Raubenheimer and R. D. Ruth, "A dispersion-free trajectory correction technique for linear colliders" Nuclear Instruments and Methods in Physics Research A302 p. 191-208 (1991).

80. R. Assmann *et al.*, "Quadrupole alignment and Trajectory Correction for Future Linear colliders: SLC Tests of a Dispersion-Free Steering Algorithm", eConf C951114, 046 IWAA-1995-046, SLAC-PUB-10485 (1995).

81. M. Masuzawa *et al.*, "Beam-based Calibration of Beam Position Monitors and measurements of the Sextupole Magnet Offsets at KEKB", Proc. of EPAC 2000, Vienna, Austria, WEP5A16, p. 1780 (2000).

82. M. Aicheler *et al.*, "A Multi-TeV Linear Collider Based on CLIC Technology: CLIC Conceptual Design Report", CERN-2012-007, -841 p. (2012).

83. C. Adolphsen *et al.*, The International Linear Collider technical design report - Volume 3.II: accelerator baseline design, arXiv:1306.6328 (2013).

84. P. Tenenbaum *et al.*, "Beam-Based Alignment of the Final Focus Test Beam", SLAC-PUB-7058 (1995).

85. T. Raubenheimer and P. Tenenbaum, "Brief Review of Linear Collider Beam-Based Alignment for Linacs", SLAC-TN-03-071 (2004).

86. B. Dehning *et al.*, "Beam based alignment at LEP," Nucl. Instrum. Methods Phys. Res. A 516, 9–20 (2004).

87. T. Lohse, P. Emma, "Linear Fitting of BPM Orbits and Lattice Parameters," SLAC-CN-371 (1989).

88. T. Kamitani *et al.*, “Beam Optics Matching in the SuperKEKB Injector”, Proc. of the First Asian Particle Accelerator Conference (APAC 98), pp.429-431.

89. Alexander Novokhatski (SLAC), Katsunobu Oide (KEK & CERN), Kaoru Yokoya (KEK), *private communication.*

APPENDIX A: EXTRA PLOTS FOR SECTION 8.1

A.1. Full Data Used for the Horizontal Offset determination of Q1 and one similar plot for the quadrupole without BPM, i.e. Q2

Figures A.1-A.4 present the full data set used to determine the misalignment of the Q1 quadrupole for the horizontal axis in Figure 8.8. These figures show the change in the slope as a function of corrector current. In particular, the average BPM_1 reading (left-bottom plot) and the slope on BPM_2 (left-top plot) were obtained from these figures and substituted into Figure 8.8.

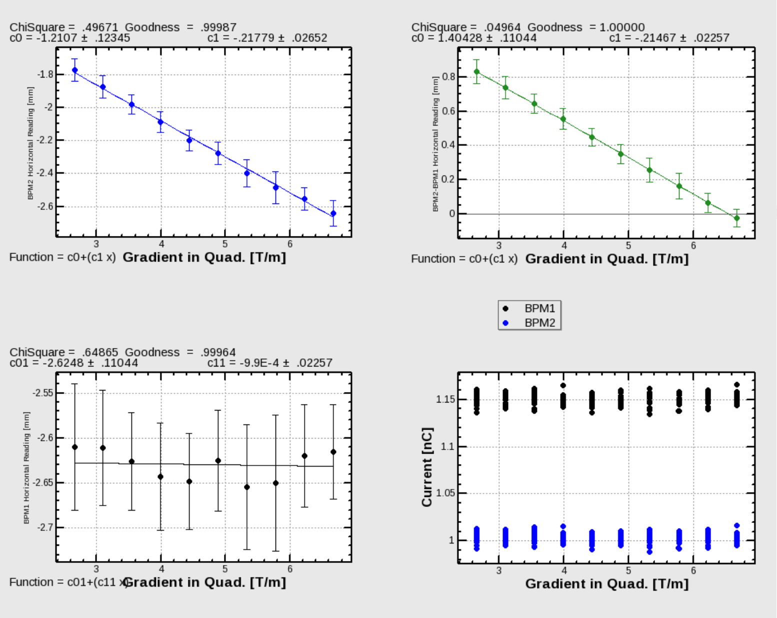

Figure A.1. This data is taken during Q1 horizontal axis studied. The steerer is set to BX135=-0.34 Amp.

The data acquisition is the same for quadrupoles with or without BPM. The example of a quadrupole without BPM in this appendix is chosen to illustrate that the same data acquisition procedure can be applied as for quadrupoles with BPMs. The only change is in the subsequent analysis, as discussed in the body of this paper. $BPM_2^{QUT=0}$ denotes the weighted average of BPM_2 readings for zero current of the QUT, or the extrapolation from QUT data recorded at different non-zero currents which would correspond to this case.

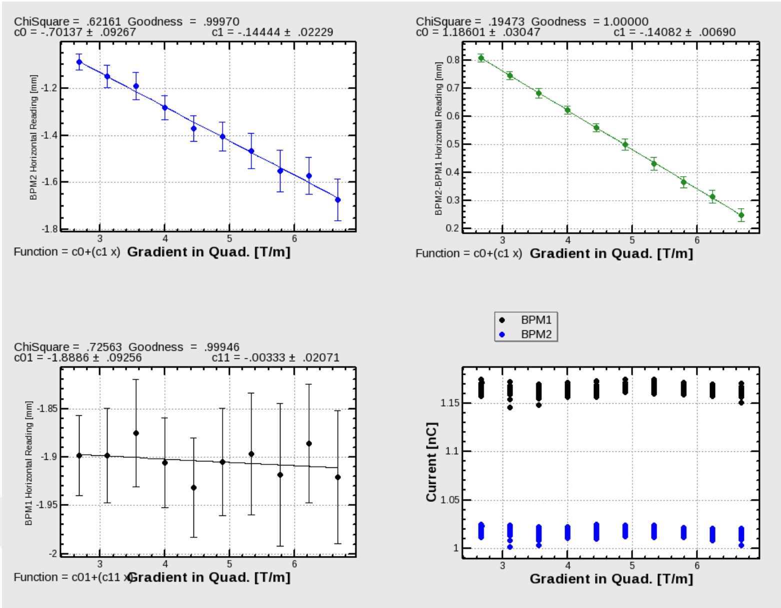

Figure A.2. Data taken during Q1 horizontal-plane studies. The corrector is set to BX135=-0.24 Amp.

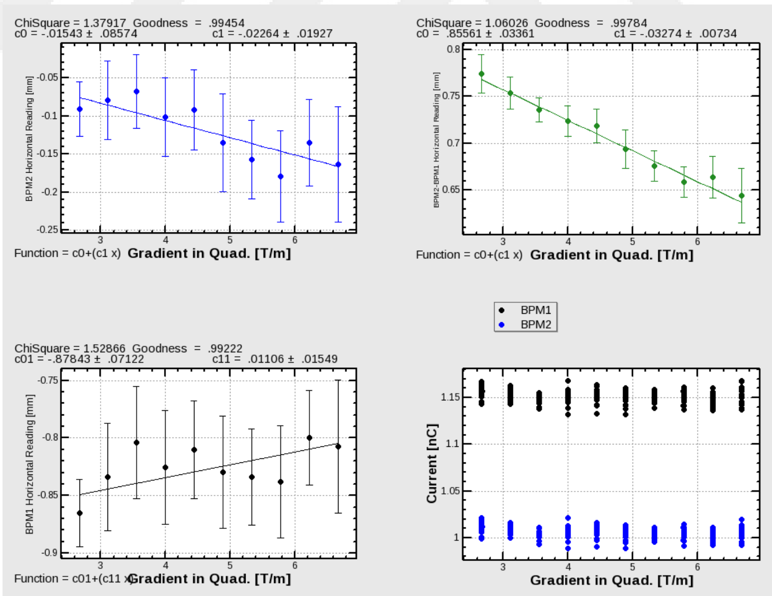

Figure A.3. Data taken during Q1 horizontal-plane studies. The corrector is set to BX135=-0.12 A.

In Figure A.5, neither BPM_1 nor BPM_2 are attached to QUT Q2, but Q2 sits 0.69 m upstream of BPM_1 and 4.55 m downstream of BPM_2, To assign a *virtual BPM*, we need to find a straight line between these two BPMs. Instead of turning off the quadrupole, we can read $\mathrm{BPM}_2^{QUT=0}$ from our regular data taking GUI. $\mathrm{BPM}_2^{QUT=0}$ corresponds to the BPM_2 readout that would be obtained for a quadrupole Q2 of zero

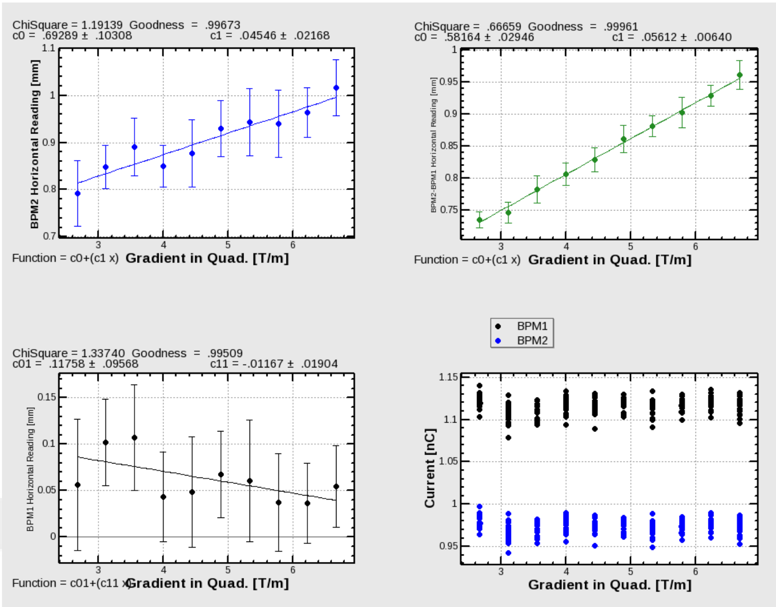

Figure A.4. Data taken during Q1 horizontal-plane studies. The corrector is set to BX135=0 A.

strength. $\mathrm{BPM}_2^{QUT=0}$ is the vertical intercept in the top-left plot. The associated error is also displayed.

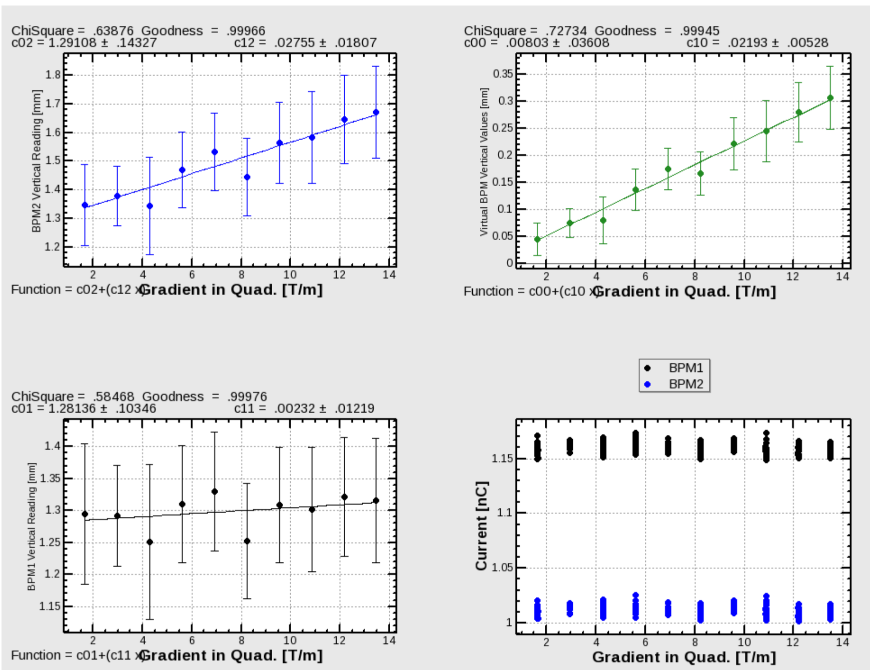

Figure A.5. Data taken during the Q2 horizontal offset study. The steerer magnet BX165 in the vicinity is used; its current is −0.22 Ampere.

APPENDIX B: EXTRA PLOTS FOR SECTION 8.4

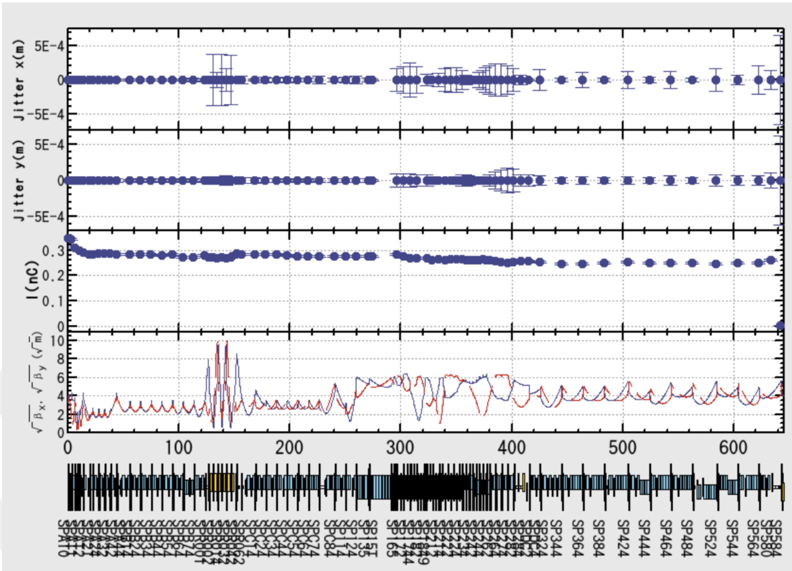

Figure B.1. The jitter still exists even though 15 m long solenoid after the target is turned off in QFE mode.

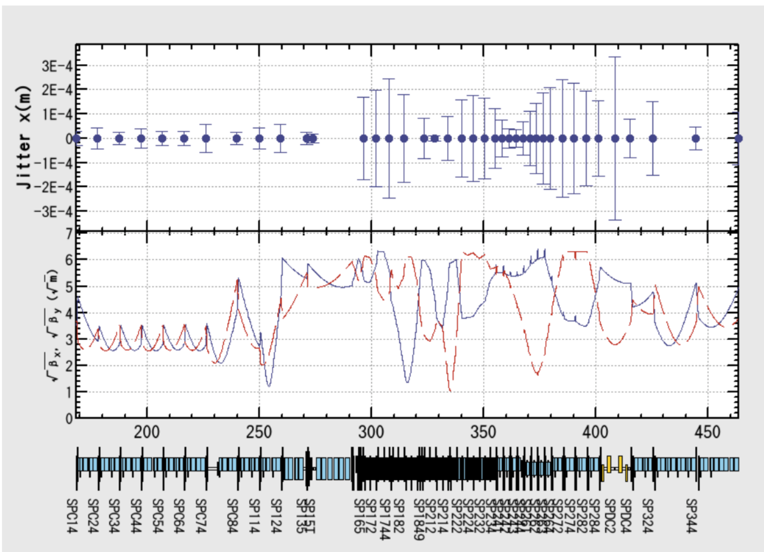

Figure B.2. The jitter still exists even though 15 m long solenoid and the flux concentrator after the target are both turned off in QFE mode.

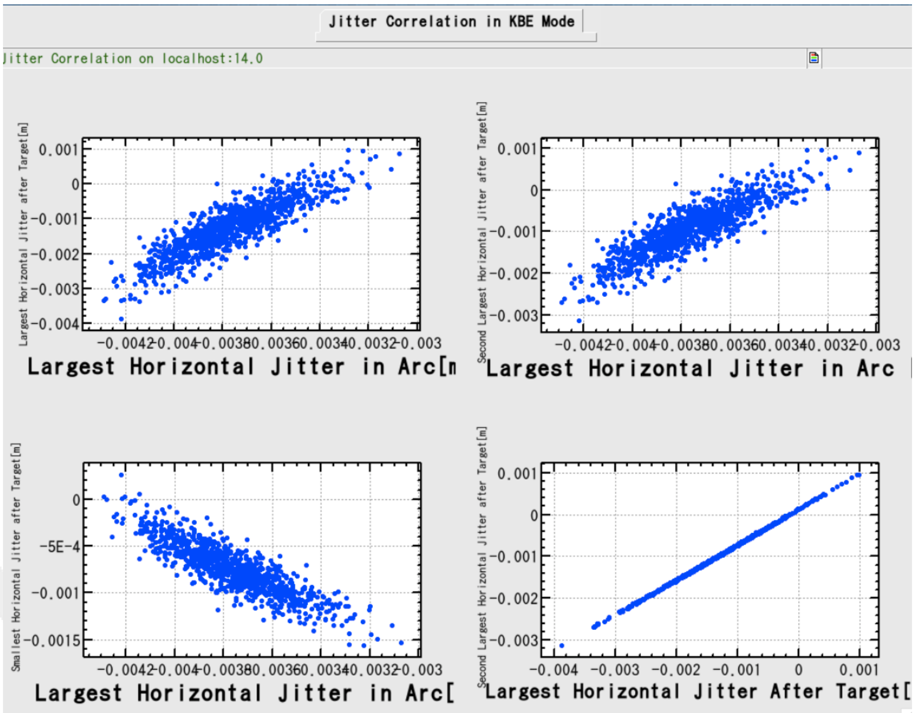

Figure B.3. Correlation plots in SFE mode. It seems that the jitter in the arc and after the target are linked.

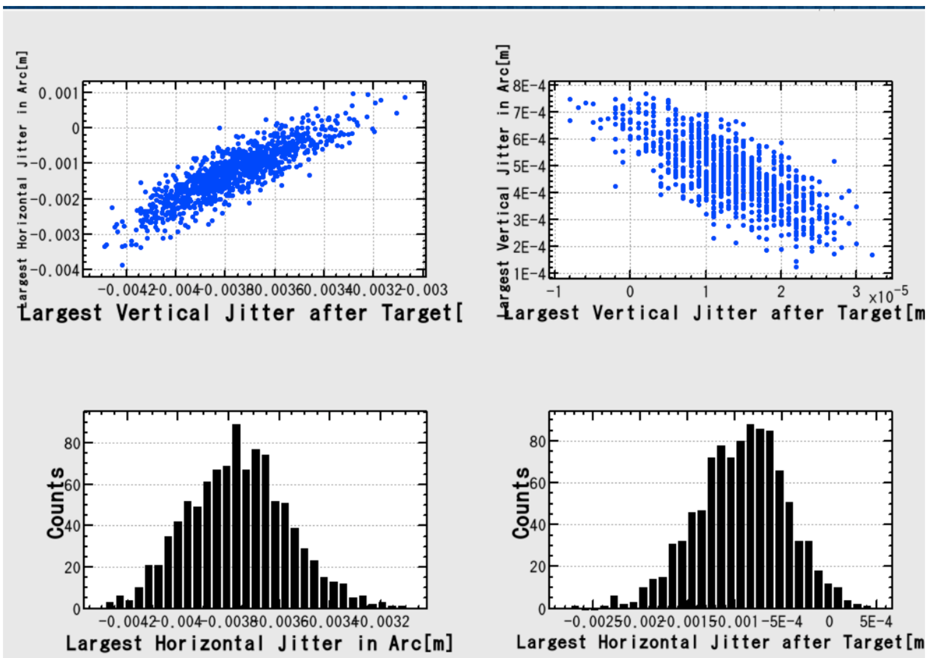

Figure B.4. Correlation plots in SFE mode. The histograms are shown in order to verify that the BPM measurements obey normal distribution. Also left top figure demonstrates the resolution of the BPM which is 1 μm.